

---

# Title page

---

**Project title:**

Damage Identification in Wind Turbine Blades - A Modal and Wavelet Analysis-based Approach

**Project theme:**

Structural health monitoring

**Project period:**

01.10.12 - 19.06.13

**Project authors:**

Jonas F. Skov & Martin D. Ulriksen

**Project supervisors:**

Professor Lars Damkilde & Professor Poul Henning Kirkegaard

**Number of pages:**

97

**Number of printed editions:**

5

**Attachments:**

DVD containing the report in PDF format, two papers and eleven appendices

---

# Abstract

---

In the present report, modal and wavelet analysis-based damage identification for wind turbine blades is addressed. Damage identification is typically classified by use of four levels, namely 1) detection, 2) localization, 3) assessment and 4) consequence. Since this report is the first of its kind at Aalborg University Esbjerg, it is chosen only to treat level 1, 2 and 3 identification, because these levels compose an appropriate basis for conducting fundamental research within the area of damage identification and subsequent expansion to more specific and complex issues.

A literature review of some of the general methods available for damage identification is presented along with a description of typical structural damages in wind turbine blades. On the basis of the review and damage descriptions, a modal analysis-based approach is preferred since this method facilitates up to level 3 identification and shows promise when it comes to in-service employment.

With modal analysis as the general approach, the damage identification must be conducted by use of a specific method which utilizes modal parameters, i.e. eigenfrequencies, mode shapes and modal damping ratios, as damage indicators. Both the eigenfrequencies and the damping ratios have proven to be inconvenient, because they, respectively, are too insensitive towards structural damages and show ambiguous changes when damage is introduced. Consequently, three methods utilizing mode shapes or their derivatives have been tested on the basis of numerically derived pre- and post-damage mode shapes of a cantilevered rectangular shell tube. Hereby, it is found that a wavelet analysis-approach yields the best results for damage detection, localization and assessment, and therefore this method is chosen.

To examine the general applicability of the modal and wavelet analysis-based damage identification method, blades from a residential-sized wind turbine, namely the Whisper 500, and a full-scale wind turbine, namely the GE 1.5 XLE, are treated. First, level 1, 2 and 3 damage identification is conducted for the Whisper 500 blade introduced to longitudinal cracks of realistic sizes. The mode shapes are derived both experimentally and numerically, and since the different results show strong correlation, the experimental and numerical findings show the same tendencies; introduction of longitudinal cracks mostly influences the mode shapes of the higher modes, especially the twisting modes, but through wavelet analysis even the first bending mode shape yields valid and useful damage detection, localization and assessment.

Damage identification analyses of the GE 1.5 XLE wind turbine blade are conducted for derived mode shapes of a numerical blade model, to which different damage types, in the form of longitudinal and transverse cracks plus edge debondings, are introduced both alternately and simultaneously. To further challenge the robustness and general applicability of the identification method, Gaussian noise is added in order to simulate typical experimental findings. It is found that valid damage identification is obtained for both single- and multi-damage scenarios with noise-contamination corresponding to a signal-to-noise ratio (SNR) of 40 dB when the second flapwise bending mode and the first twisting mode are employed along with the first flapwise bending mode.

---

---

# Preface

---

The report in hand is the M.Sc. thesis of group BM4-1. The thesis is written during third and fourth semester of the master programme in Mechanical Engineering at Aalborg University.

The theme of the project is structural health monitoring, and in this report modal and wavelet analysis-based damage identification in wind turbine blades is addressed. The project, which covers experimental tests and numerical simulations, is the first of its kind at Aalborg University, Esbjerg department, and therefore a lot of work has been invested in literature reviewing, theoretical studies and testing of the equipment utilized in the experiments. It has been found that a theoretical understanding of basic physical and mathematical subjects such as structural dynamics, the finite element method, calculus and linear algebra is necessary, thus it is assumed that the reader has a certain degree of literacy concerning these subjects.

Throughout the entire report, references will appear. These references are specified in a bibliography at the back of the report. The references are indicated with the number method, by which a reference is given by [X], with X referring to the Xth position in the bibliography. Here, the books are indicated with author, title, publisher, edition and publication year, whereas Internet pages are indicated with link, title and the accessed date. With regard to figures it is noted that any reference will appear from the figure text, hence figures without references are produced by the authors of this report. Lastly, references to appendices are indexed with letters.

The appendices of the project can be found on the enclosed DVD, on which a copy of the report in PDF format and two papers also are included. The papers, which are produced during the third semester by the authors and supervisors of this report plus Kristoffer A. Dickow, Ph.D. student at Aalborg University, document studies performed in state-of-the-art SHM techniques and a modal analysis-based SHM technique for damage detection in a small wind turbine blade, respectively. Both papers are submitted to the 10th International Conference on Damage Assessment of Structures (DAMAS) 2013. The appendices include MATLAB pseudocodes whose files, unless stated otherwise, are produced by the authors of this report. The appendices also include ANSYS Workbench tutorials which are produced by the authors of this report. The tutorials cover modeling aspects new to the authors and serve, i.a., as helping tools for coming students and others who are interested in ANSYS Workbench analyses.

## Acknowledgments

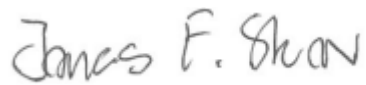
The report is written under supervision of professors at Aalborg University, Lars Damkilde and Poul Henning Kirkegaard. The supervisors have contributed highly to the completion of this report and the two papers submitted to DAMAS 2013. For that, the authors of this report express gratitude.

Thanks are also given to Kristoffer A. Dickow, Ph.D. student at Aalborg University, for general guidance throughout the project, and in particular regarding the experiments conducted in the project. Without his help, the experimental tests would not have been possible.

Furthermore, thanks are given to Find M. Jensen, Ph.D., Chief Technology Officer at Bladena, and Michael S. Jepsen, Ph.D. student at Aalborg University, for, respectively, guidance regarding damage types in wind turbine blades and guidance regarding the experiments conducted in the project. The contributions from both are highly appreciated.


Finally, the financial support by the SYSWIND project, funded by the Marie Curie Actions under the Seventh Framework Programme for Research and Technology Development of the EU, is gratefully acknowledged.

Aalborg University Esbjerg  
June 19, 2013



---

Jonas F. Skov



---

Martin D. Ulriksen



---

---

# Contents

---

<b>Title page</b>	<b>III</b>
<b>Abstract</b>	<b>IV</b>
<b>Preface</b>	<b>V</b>
<b>1 Introduction</b>	<b>1</b>
1.1 Structural damages in wind turbine blades . . . . .	2
1.2 SHM techniques for wind turbine blades . . . . .	5
1.3 Project specification . . . . .	9
<b>2 Methodology</b>	<b>12</b>
2.1 Modal analysis . . . . .	13
2.2 Damage detection . . . . .	20
2.3 Damage localization . . . . .	21
2.4 Damage assessment . . . . .	28
2.5 Summary . . . . .	31
<b>3 Experimental setup for Whisper 500 blade</b>	<b>33</b>
3.1 Fixation system . . . . .	33
3.2 Impact hammer . . . . .	34
3.3 Accelerometers . . . . .	35
3.4 Data analyzer . . . . .	35
3.5 Summary . . . . .	40
<b>4 Finite element model of Whisper 500 blade</b>	<b>41</b>
4.1 Geometry . . . . .	41
4.2 Materials . . . . .	43
4.3 Boundary conditions . . . . .	45
4.4 Damping properties . . . . .	46
4.5 Discretization . . . . .	47
4.6 Model calibration . . . . .	51
4.7 Summary . . . . .	53
<b>5 Damage identification for Whisper 500 blade</b>	<b>55</b>
5.1 Modal analysis . . . . .	55
5.2 Damage detection . . . . .	61
5.3 Damage localization . . . . .	62
5.4 Damage assessment . . . . .	64
5.5 Summary . . . . .	66

<b>6</b>	<b>Finite element model of GE 1.5 XLE blade</b>	<b>68</b>
6.1	Geometry . . . . .	68
6.2	Material . . . . .	69
6.3	Boundary conditions . . . . .	70
6.4	Discretization . . . . .	70
6.5	Summary . . . . .	70
<b>7</b>	<b>Damage identification for GE 1.5 XLE blade</b>	<b>71</b>
7.1	Description of individual damages . . . . .	72
7.2	Measurement points . . . . .	72
7.3	Criteria for valid identification . . . . .	73
7.4	Single-damage identification analyses . . . . .	73
7.5	Multi-damage identification analyses . . . . .	86
7.6	Summary . . . . .	89
<b>8</b>	<b>Conclusion</b>	<b>91</b>
	<b>Bibliography</b>	<b>93</b>
<b>A</b>	<b>ANSYS Workbench tutorial - Orthotropic model</b>	
<b>B</b>	<b>MATLAB pseudocode - Signal analysis</b>	
<b>C</b>	<b>ANSYS Workbench tutorial - Simulating hammer hit-based vibrations</b>	
<b>D</b>	<b>Damage identification - MSC and WA with noise-contaminated signals</b>	
<b>E</b>	<b>Damage identification - Example of two-dimensional WA method</b>	
<b>F</b>	<b>MATLAB pseudocode - Wavelet analysis</b>	
<b>G</b>	<b>Mathematical proof - Orthogonality in damped eigenvalue problem</b>	
<b>H</b>	<b>ANSYS Workbench tutorial - Employment of superelements</b>	
<b>I</b>	<b>ANSYS Workbench tutorial - Model calibration</b>	
<b>J</b>	<b>Experimental findings - Pre-damage mode shapes of Whisper 500 blade</b>	
<b>K</b>	<b>ANSYS Workbench tutorial - Varying shell thickness</b>	

# INTRODUCTION

One of the significant issues in the wind industry is how to increase the reliability of wind turbines and decrease maintenance costs at the same time. Current maintenance costs of new offshore turbines, such as those depicted in Fig. 1.1a, are very high and can easily make up to 20-25 % of the total cost of produced energy and sometimes even more [1]. Therefore, the development of condition monitoring and structural health monitoring (SHM) techniques has been of great interest in the last decade. The aim of such SHM techniques can be to identify and categorize the damages which make the operators able to optimize maintenance or in the case of an emergency, shut down the wind turbine to avoid further failure. An often used classification for damage identification within SHM defines four levels, namely 1) detection, 2) localization, 3) assessment and 4) consequence [2]. Since the levels are considered accumulative, level 1 SHM techniques can only be used for general detection of damage, while level 2 techniques can provide additional information in the form of the damage location. Moreover, level 3 techniques can give information about the damage size, and lastly level 4 techniques yield additional information about the safety of the damaged structure based on the specific damage. In general, the presented classification system is useful when describing an SHM technique and when comparing the applicability of different SHM techniques.

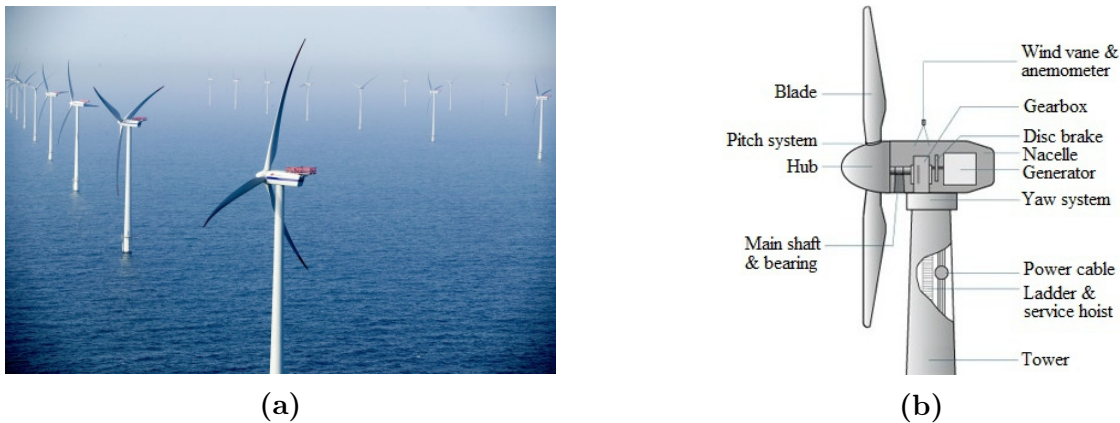


**Fig. 1.1:** Wind turbine system. (a) A picture of the offshore wind turbine park in Horns Rev, Denmark [3]. (b) An overview of the main components in a typical wind turbine [4].

Several studies have presented SHM techniques which measure a range of quantities like temperature, noise and vibration parameters to be used for monitoring of structural wind turbine components, e.g. gearboxes, generator bearings or blades [5,6,7]. In Fig. 1.1b, the main structural components of a typical wind turbine are specified.

While failure can occur in any structural component of the wind turbine, one of the most common and critical components to fail is the blades [8]. Here, several different damage types can be introduced [9] and in an extreme, failure like shown in Fig. 1.2 can occur. In Section 1.1, some of the damage types most commonly occurring in wind turbine blades are described. It is noticed that the text presented in Sections 1.1 and 1.2 is mainly from DAMAS paper 1<sup>1</sup>.

<sup>1</sup>DAMAS paper 1 can be found on the enclosed DVD.



**Fig. 1.2:** Wind turbine with a failed blade [10]. The wind turbine is located near Wilton, North Dakota, USA.

## 1.1 Structural damages in wind turbine blades

In the study documented in [9], 15 blades of 300 kW wind turbines and 81 blades of 100 kW wind turbines, all with a life time ranging between 16 and 19 years, were inspected. As a result of these inspections, several different damage types were found and subsequently categorized into the following three overall groups:

1. Cracks; in the form of transverse cracks, longitudinal cracks and surface cracks.
2. Edge damages; in the form of edge crushing plus side separation.
3. Surface and coating damages; in the form of coating pores, surface damages, holes or penetrations and reworked areas.

In Subsections 1.1.1 - 1.1.3, the damage types in each group will be described on the basis of the study presented in [9], and subsequently the severity of the different damage types will

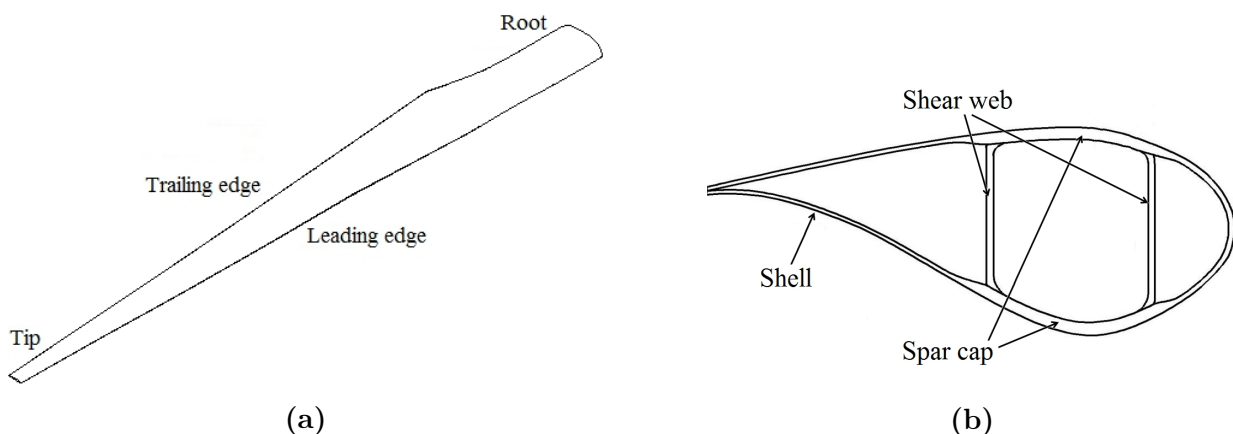


**Fig. 1.3:** Sketches of a wind turbine blade with geometric specifications. (a) Overall illustration. (b) Cross-sectional view (edited version of a figure found in [11]).

be evaluated in Subsection 1.1.4. In the damage type descriptions, certain blade geometric specifications will be used. These are specified in Fig. 1.3.

### 1.1.1 Cracks

As stated in the listing introductory in the present section, the damage group cracks include transverse, longitudinal and surface cracks, see Fig. 1.4. The latter is a crack type which spreads over areas with different sizes, having a random orientation or sometimes with a radial orientation from a certain point, while the transverse and longitudinal cracks are the ones growing perpendicular and parallel to the blade edges.

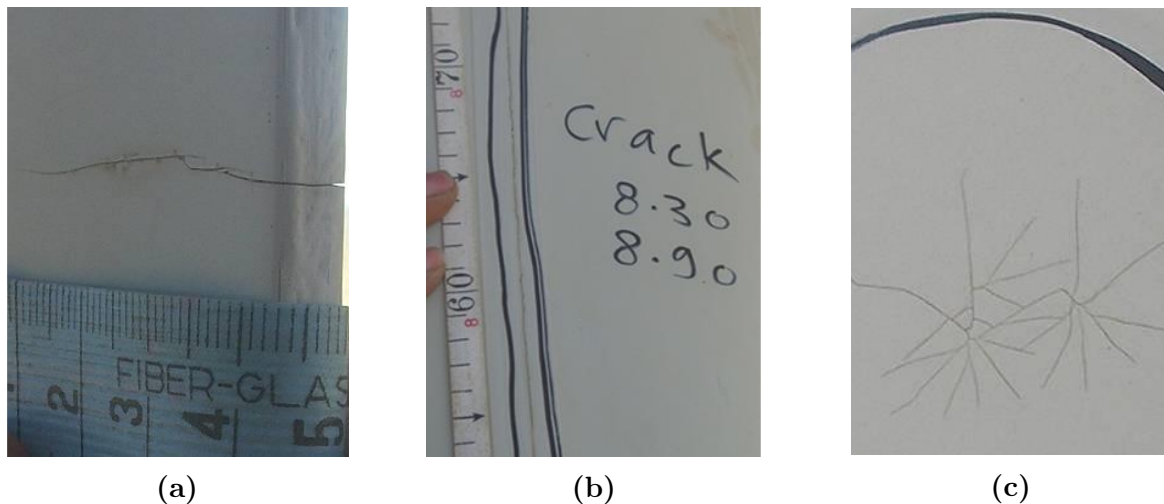


**Fig. 1.4:** Cracks in wind turbine blades [9]. (a) A transverse crack. (b) A longitudinal crack. (c) Surface cracks.

In the study documented in [9], the found surface cracks were fine shallow cracks on the coating layer of the blade which could not be detected fully by visual inspection, hence another detection method, in the form of liquid penetrant test, was used. On the contrary, the transverse and longitudinal cracks could be detected visually, and hereby a maximum transverse crack of 4 cm (near the tip in a 300 kW turbine blade) and a maximum longitudinal crack of 59 cm (near the root in a 100 kW turbine blade) were found. It was observed that most of the transverse and longitudinal cracks occur near the root and tip, respectively.

### 1.1.2 Edge damages

The edge damage group includes edge crushing plus side separation, see Fig. 1.5. The latter is a cracking or debonding in the joining region of one of the blade edges. It was found in [9] that most of these side separations occur near the root, more specifically at the radical geometric change, and near the tip. The maximum side separation, measuring 135 cm, was found in a 300 kW turbine blade, half-way along the trailing edge, see e.g. Fig. 1.3a.

For the edge crushing, it was found in [9] that these primarily occur in the lower third of the blade length. Here, the edge is very thin and sharp, thus making it easy to be crushed by an impact with an external body, e.g. a crane lifting basket. The maximum edge crushing found was 13 cm long, located near the root of a 300 kW turbine blade.



**Fig. 1.5:** Edge damages in wind turbine blades [9]. (a) Edge crushing. (b) Debonding.

### 1.1.3 Surface and coating damages

In [9], most of the detected surface and coating damages were shallow surface damages, while only a few were deep damages, i.e. holes and penetrations. In Fig. 1.6, pictures of blades with coating pores and penetrations, respectively, are presented.

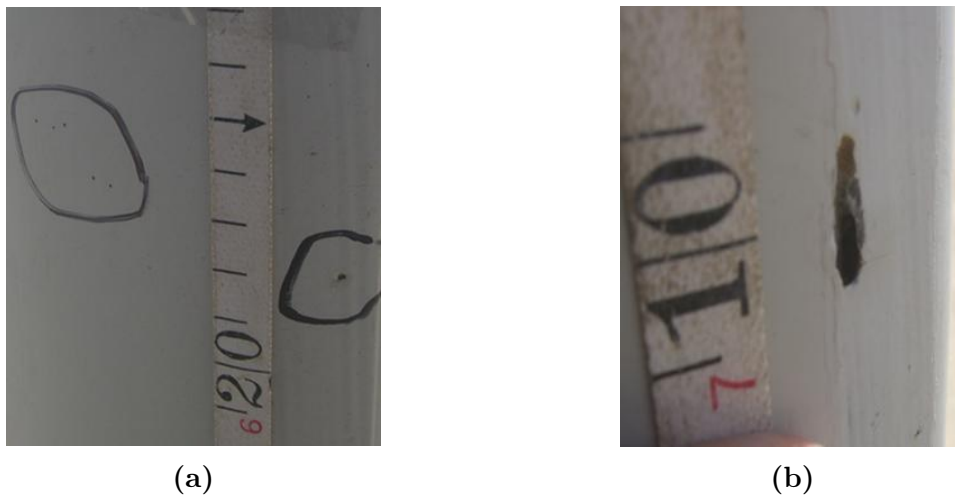


**Fig. 1.6:** Surface and coating damages in wind turbine blades [9]. (a) Coating pores. (b) Penetration in the leading blade edge.

The holes and penetrations were pits of a clear penetration through the blade material and had a diameter of 3-10 mm [9]. Most likely, these originated from the manufacture and mechanical interactions with external bodies. Similarly, the shallow surface damages are expected to arise due to the manufacture process [9].

Despite the fact that the surface and coating damages were primarily small and shallow, these damages are serious because they result in a rougher blade surface, which increases the aerodynamic drag and consequently decreases the efficiency of the wind turbine [9].

### 1.1.4 Summary of blade damage descriptions

Through inspection of 15 300 kW wind turbine blades and 81 100 kW wind turbine blades, three general damage types were found in the study documented in [9]. Of these damage types, some of the most frequently occurring and severe were the longitudinal cracks and debondings, respectively. A 59 cm edgewise crack was found in one of the 100 kW turbine blades, and a 130 cm debonding was observed in one of the 300 kW turbine blades. In the study, it was concluded that structural repairs of these damage types are a necessity for the blades to operate properly. Additionally, cosmetic repairs of especially the surface damages were recommended, because such repairs will decrease the surface roughness and, thus, minimize the aerodynamic drag.

In [11], it is described how longitudinal cracks on and near the leading edge are very often found on blades in operation after few years. Finite element analyses documented in [11] show that the stresses are increased in the leading edge area when the blade is distorted in transverse shear, see Fig. 1.7a, thus providing a plausible cause for the onset of debondings and longitudinal cracks in and near the leading edge. Additionally, [11] predicts that the problem with debonding of the trailing edge will be even more dominant in the future because of the upscale in wind turbines which leads to increased loads and consequently larger deformations of the trailing edge, see Fig. 1.7b.

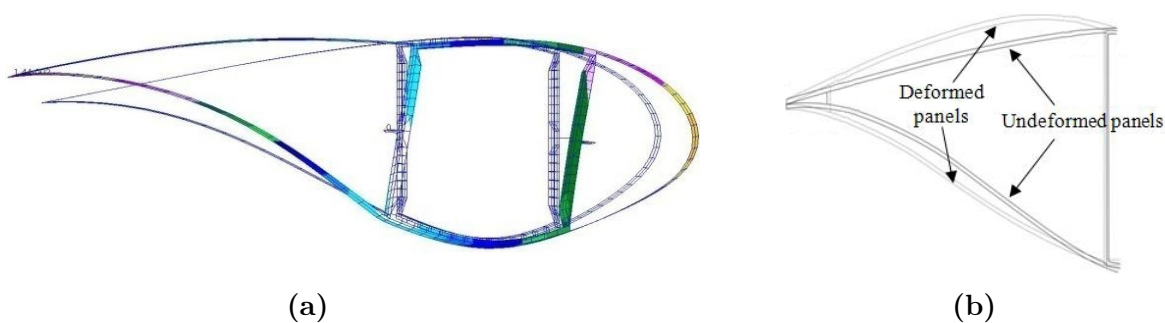


**Fig. 1.7:** Cross-sectional deformations of a wind turbine blade [11]. (a) FEA post-processing of transverse shear distortion. (b) Deformations of trailing edge panels.

Since the blades account for 15-20 % of the total wind turbine costs [12], great focus has been dedicated to monitoring of this particular structural component to reduce the amount of costly repairs and fatal failures. Some of the most frequently studied SHM techniques for damage identification of wind turbine blades are presented and described in Section 1.2.

## 1.2 SHM techniques for wind turbine blades

A wide-ranging variety of SHM techniques is available for monitoring of wind turbine blades. In the present section, an outline of some of the most frequently studied techniques is given. The specific techniques are based on physical quantities, namely temperature, noise and vibration, respectively.

### 1.2.1 Temperature-based technique

The basic idea of a temperature-based SHM technique is to use infrared thermography to detect subsurface features, such as subsurface defects and anomalies, on the basis of temperature differences on the investigated surface [13]. These temperature differences occur in all elastic materials when stressed under adiabatic conditions, see e.g. [14].

Infrared thermography can be deployed by two approaches, namely a passive and an active approach [13]. With the passive approach, thermography is used to investigate materials that are at different temperature than ambient, while the active approach utilizes an external stimulus source, e.g. heat lamps or optical flash lamps, to induce relevant thermal contrasts [13]. The passive approach is not commonly applied in SHM techniques for wind turbines [15].

The infrared thermography is conducted with an infrared camera measuring radiation in the infrared spectrum [13]. This radiation energy is rendered to a temperature value, and hereby temperature differences can be obtained via multiple distinct measurements. Wind turbine blades generally exhibit a temperature rise when stressed because of the viscoelastic constitutive relationships of the blade material, i.e. glass fibre reinforced epoxy or polyester [16]. The damage zones are associated with additional heating, thus enabling distinction between general temperature rise in the non-critical zones and the additional heating in the critical zones [13]. This distinction has been possible in the studies and tests performed in [5,16]. Furthermore, since thermoelastic stresses can be derived on the basis of temperature differences [13], thermography also has the advantage of facilitating characterization of stress distributions and identification of stress concentration areas of a surface [17]. Moreover, it is advantageous that the thermography technique is an area investigating technique, whereas most of the other SHM techniques are based on either point or line testing methods [13]. This means that the thermography technique can detect details impossible to detect with few-point measurement methods, e.g. strain gauge measurements, hence the technique performs well for all the different damage types. However, the thermography technique also has some clear disadvantages due to the use of infrared technology. These disadvantages include a limitation in penetration depth [13] and the sensitivity towards spatial and temporal temperature variations [5]. The latter makes it necessary to keep the load amplitude to a minimum during the measurements [5], hence the technique is not suitable for monitoring of in-service wind turbine blades.

### 1.2.2 Noise-based technique

Processes such as deformations, impacts, cracking and crushing all yield local transient changes in stored elastic energy with a broad spectral content [15]. In typical certification tests of wind turbine blades, static and fatigue tests are conducted to examine whether the blade can withstand extreme load cases as defined in the wind turbine design and testing standards [18,19]. Normally, an audible acoustic emission is detected [5], but without any kind of monitoring equipment it is impossible to locate the source.

By use of acoustic emission monitoring, surface-mounted piezoelectric transducers detect elastic stress waves within a structure and facilitate the location of the origin of these waves within the structure [6]. Also, signals in the non-audible frequency domain, i.e. 20-1200 kHz [5], can be detected as well [6]. In general, the intensity of the recorded wave signals increases as damage becomes more critical [20], thus in theory enabling distinction between normal operational conditions and development of damages and failures. As described in [5,6], the conventional way of acoustic emission testing is to load a structure to slightly above the highest



service load and then hold this load constantly for approximately 10 minutes (referred to as load-hold) to establish stability. For an undamaged structure, acoustic emission will be introduced the first time the load has reached maximum, but subsequently no significant acoustic emission will occur when applying the same load [6]. Hence, the aim of the test is to examine if acoustic emission activity continues during the load-hold period, indicating progressive damage. However, since wind turbine blades can be subjected to high, momentary loads, e.g. the 50 year gust wind [18], the conventional method with 10 minutes load-hold is not suitable. Consequently, an alternative loading method has been introduced in [21]. Here, the highest service load is applied momentary, and subsequently so-called examination loadings are applied to determine the minimum load level at which acoustic emission can be detected [21].

With application of the modified load method, it has been found in [5,6,20,21] that acoustic emission monitoring can identify damage areas plus hot spots and weak points in small wind turbine blades. However, some studies, e.g. [22], report that the diversity of materials in wind turbine blades results in challenging acoustic properties for acoustic emission monitoring. Consequently, the acoustic energy attenuation has been found to be relatively high, thus many sensors must be used [22].

Generally, the studies in [5,6,20,21,22] show that acoustic emission monitoring is a useful SHM technique which, under controlled laboratory tests, can be used for both detection and localization of structural damages in wind turbine blades. Additionally, studies in [23,24] report that the acoustic emission monitoring technique can be applied to the blades of an in-service wind turbine.

### 1.2.3 Vibration-based technique

The basic idea of vibration-based SHM techniques is to monitor the dynamic response of a structure, e.g. accelerations or strains, and hereby detect potential damage-induced changes in the physical properties, i.e. stiffness, damping and mass. An evident way to detect these changes is to examine the modal parameters, i.e. eigenfrequencies, mode shapes and modal damping, which are functions of the physical properties and, thus, altered as a consequence of the change in physical properties.

Typically, vibration-based SHM techniques are based on comparisons between a pre-damage response and a post-damage response, both generated by an excitation source. Several excitation sources are available, with some of the most commonly used being ambient energy plus external shakers and hammers. The former excitation source is utilized in SHM of in-service wind turbines [25], while the external excitation sources are widely used in laboratory tests, see e.g. [7]. Each excitation source has advantages and disadvantages, thus the choice of source must be made on the basis of the specific test, as described in [26]. In [7], a hammer-excited blade from a residential-sized wind turbine is monitored by use of modal analysis. The dynamic response is measured as accelerations, and it is found that an edgewise crack placed in a critical area yields significant frequency and mode shape changes in the twisting modes and in the high-frequency bending modes. Hence, the SHM technique can be used to detect damages under the right circumstances. However, to obtain these circumstances, several aspects, e.g. transducer placement and excitation method, have to be considered. For instance, the amount and placement of transducers must be chosen such that the dynamic response is captured correctly, i.e. the wanted modes can be observed, and specifically such that the obtained mode shapes can be represented validly and subsequently used to locate and assess the damage [27].

Regarding the excitation method, it is found in [7] that the edgewise crack only results in significant modal parameter changes in the high-frequency modes, thus the excitation source must facilitate excitation of these. Since only the first bending modes are excited in in-service wind turbine blades [15], the study in [7] implies that an extra excitation method must be implemented if the modal parameters are to be used directly in an efficient way for in-service wind turbine blades. Another disadvantage is the sensitivity difference in modal parameters for the different damage types. For instance, the study in [7] shows that the modal parameters are changed significantly less when introducing a surface crack compared to an edgewise crack.

#### 1.2.4 Summary of SHM technique outline

When looking at the presented outline of different SHM techniques, it is evident that each technique has desirable advantages but also clear disadvantages. Thus, when considering SHM of a wind turbine blade, the technique should be chosen on behalf of a variety of factors, such as available equipment, environmental influence, damage type and desired type of damage identification. The latter can be evaluated by use of the four-level classification system, mentioned introductory in the present chapter, which is used to indicate to which extent an SHM technique can identify a damage. On the basis of this classification, a typology of the outlined SHM techniques can be schematized, see Table 1.1. The typology is based on the techniques for wind turbine blades in general, i.e. it is not only for those in service, and distinguish between the three overall damage types presented in the present section, see the listing introductory in the section for numbering.

**Table 1.1:** Damage identification typology for SHM techniques, with ”+” indicating that the technique is usable and ”÷” indicating that it is unusable. Brackets are used when the technique is partially usable. The usability is based solely on the specific technique, i.e. no extra methods can be employed. Note that the abbreviations ID (Identification), SDT (Structural damage type), Temp. (Temperature), AE (Acoustic emission) and MA (Modal analysis) are used.

ID level	SDT	Temp.-based SHM	AE-based SHM	MA-based SHM
1	1	+	+	(+)
	2	+	+	+
	3	+	(+)	(+)
2	1	+	+	(+)
	2	+	+	+
	3	+	(+)	(+)
3	1	÷	÷	(+)
	2	÷	÷	+
	3	÷	÷	(+)
4	1	÷	÷	÷
	2	÷	÷	÷
	3	÷	÷	÷

Table 1.1 reveals that the temperature-based technique and the acoustic emission-based technique independently can provide level 1 and level 2 information. However, while the

temperature-based technique can cover all damage types, the acoustic emission-based technique has some shortcomings in damage type 3, specifically shallow surface damages, because of the insignificant acoustic emission. The modal analysis-based technique, which can provide up to level 3 information, also experiences shortcomings in identifying shallow surface damages, and furthermore the technique allegedly lacks sensitivity towards transverse cracks (part of damage type 1).

All the techniques can reach level 4 when extra methods are employed. In [20], it is described how an addition in the form of pattern recognition software was necessary to assess a structural damage by use of the acoustic emission-based technique, and in [28] it is documented how a novel approach correlating the temperature signal with the second harmonic of the loading frequency was necessary to assess the structural damages in a wind turbine blade. Hence, the only SHM technique, described in the present report, capable of providing level 3 information without implementation of additional methods is the modal analysis-based. But, this technique has some general shortcomings regarding damage identification because of the sensitivity differences for damage types, i.e. the modal parameters can be found to change significantly less when introducing, e.g., a surface hole compared to a longitudinal crack or a debonding, see [7]. Furthermore, since studies, e.g. [7], imply that significant changes in modal parameters only occur in the high-frequency modes, an extra method exciting these modes must allegedly be implemented if the modal analysis-based SHM technique is to be used efficiently for in-service wind turbine blades. This extra excitation can, however, easily be obtained by implementing some sort of control of the wind turbine which can decelerate the blade rotations, hence obtaining a high-frequency load wave traveling through the blades. Therefore, both the acoustic emission-based and modal analysis-based SHM techniques show promising usability for in-service wind turbine blades, whereas the temperature-based SHM technique, cf. Subsection 1.2.1, is not suitable for in-service conditions because of the sensitivity towards spatial and temporal temperature variations.

### 1.3 Project specification

The aim of the present report is to conduct damage identification of a full-scale wind turbine blade by use of SHM. Due to project limitations, it is chosen to conduct the damage identification up to and including level 3, i.e. damage detection, localization and assessment. Based on the descriptions and comparisons of different SHM techniques in the previous section, it is chosen to use a modal analysis-based technique. Although the experiments in the project are conducted in laboratories, the temperature-based technique was immediately discarded in the selection process because of the lack of robustness. In the final choice between the acoustic emission-based technique and the modal analysis-based technique, the latter was preferred because of its methodical independence; unlike the acoustic emission-based technique, the modal analysis-based technique can, cf. Table 1.1, provide level 3 damage identification information without implementation of other separate methods. Furthermore, the modal analysis-based technique is appealing because, as mentioned in the previous section, studies imply that only the high-frequency modes are applicable when conducting damage identification based on modal parameters. In the present report, this assumption will be examined.

Before conducting damage identification analysis of the full-scale blade, two simpler geometries are examined in order to gradually apply the theories and methods for increasingly complex, blade-resembling geometries. First, in Chapter 2, a numerical model of a cantilevered

rectangular shell tube is introduced to a longitudinal crack to establish the methodological process of damage identification, and subsequently a blade from a residential-sized wind turbine, namely the Whisper 500 model shown in Fig. 1.8a, will be examined by use of the established procedure both numerically and experimentally. The Whisper 500 blade depicted in Fig. 1.8b has a length of 2.2 m and a mass of 3.2 kg, and it consists of two structural components; an outer glass- and carbon-fibre reinforced composite shell and an inner PVC foam core, i.e. the blade has no shear webs, see e.g. Fig. 1.3b. Regarding the damage type, it is chosen to introduce longitudinal cracks in the leading edge of the Whisper 500 blade. This choice is based on the findings and descriptions presented in the previous section, which state that the longitudinal cracks and the debondings are the most severe and commonly occurring damage types. The crack is chosen rather than debonding due to practical circumstances; a utility knife is used to produce the damage, and since this method removes a small amount of material, an actual crack is introduced in the blade.

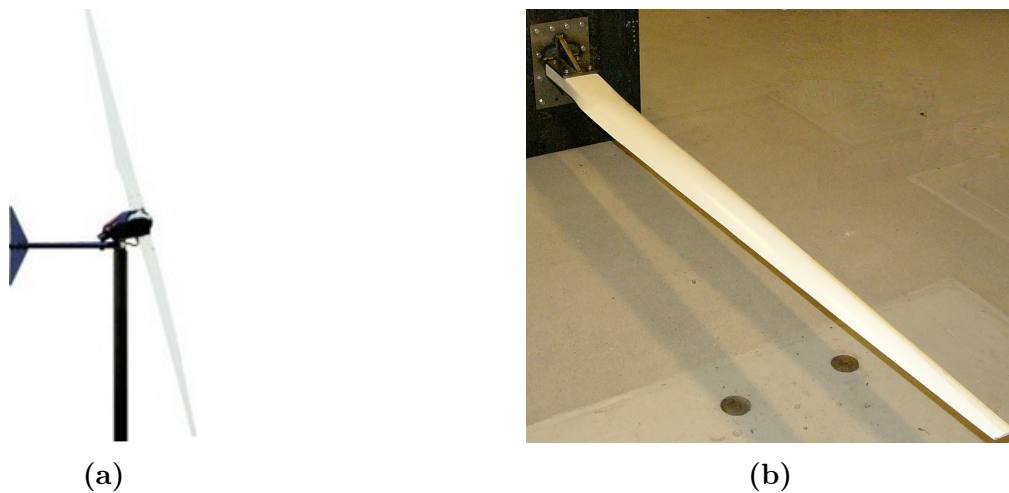


**Fig. 1.8:** Whisper 500 wind turbine system. (a) Whisper 500 turbine system [29]. (b) A picture of the blade.

After the damage identification analysis of the Whisper 500 blade, a full-scale blade is examined numerically. The blade is from a 1500 kW onshore wind turbine, namely a GE 1.5 XLE, see Fig. 1.9, whose blades are 41.2 m long and constructed in glass fibre reinforced plastic [30]. The GE 1.5 XLE blade consists of the shell surface and a shear web, which can be seen in Section 6.1 where the numerical model of the GE 1.5 XLE blade is documented. The initial geometry of the blade is obtained from [31].

When summarizing the project specification, the analysis structure of the present project can be formulated as the following:

- Level 1, 2 and 3 damage identification analyses of cantilevered rectangular shell tube with a longitudinal crack. The analyses, which only cover numerical work, are utilized to present the formulation and validation of the employed methods.
- Level 1, 2 and 3 damage identification analyses of residential-sized Whisper 500 blade with longitudinal cracks. The analyses cover both experimental and numerical work.
- Level 1, 2 and 3 damage identification analyses of GE 1.5 XLE blade with different damage types, namely cracks and debondings. The analyses only cover numerical work.



**Fig. 1.9:** GE 1.5 XLE wind turbine [32].

On the basis of literature regarding vibration-based SHM, see e.g. the references in Subsection 1.2.3, it is found that level 1, 2 and 3 damage identification has only been successfully conducted for simple systems such as two-dimensional beams with transverse cracks, two-dimensional truss systems with an entire truss simulating damage, and plates with both transverse and longitudinal cracks. Thus, since all the three systems treated in the present report are three-dimensional, the possibility of applying modal analysis-based damage identification to more complicated and realistic systems will be examined.

As seen in the listing on the previous page, the modal analyses generally cover both experimental tests and numerical simulations. The experimental tests of the Whisper 500 blade are conducted in a laboratory at Aalborg University, Esbjerg department. The numerical simulations are conducted in the commercial finite element program ANSYS Workbench 14.0.

---

# METHODOLOGY

---

The main aim of this project is to examine whether a modal analysis-based SHM technique can be used for damage identification in wind turbine blades. In general, modal analysis consists of extraction of modal parameters, i.e. eigenfrequencies, mode shapes and modal damping, thus the mathematical basis is the equations of motion

$$M\ddot{\mathbf{x}} + C\dot{\mathbf{x}} + K\mathbf{x} = \mathbf{r}, \quad (2.1)$$

where  $M$ ,  $C$  and  $K$  are the mass, damping and stiffness matrix, respectively,  $\ddot{\mathbf{x}}$ ,  $\dot{\mathbf{x}}$  and  $\mathbf{x}$  are the acceleration, velocity and displacement vector, respectively, and  $\mathbf{r}$  is the external force vector. In all tests and analyses documented in the present report, linearity is assumed, i.e. the system displacements are small and the damping matrix is expressed as a linear combination of the mass matrix and the stiffness matrix. The damping condition implies that since  $M$  and  $K$  are both symmetric,  $C$  is also symmetric. Furthermore, it is assumed that the analyzed systems are time-invariant, i.e. the system output does not depend explicitly on time.

The damage identification consists of detection, localization and assessment. The idea is that introduction of a structural damage will decrease the stiffness and, thus, alter the modal parameters. In the finite element method, the local stiffness matrix of each element,  $K$ , is derived by

$$K = \int_V B^T D B dV, \quad (2.2)$$

in which  $V$  is the volume of interest,  $B$  is the strain-displacement matrix, and  $D$  is the constitutive matrix. For instance, for a 2-dimensional isotropic Euler-Bernoulli beam element,  $D$  is given as

$$D = \begin{bmatrix} EA & 0 \\ 0 & EI \end{bmatrix}, \quad (2.3)$$

where  $E$ ,  $A$  and  $I$  are Young's modulus, cross-sectional area and the moment of inertia, respectively. As an introduction of a crack will remove material, both  $A$  and  $I$  will be reduced, hence the stiffness matrix will be changed compared to the corresponding of an intact element. This suggests that an intuitive way of identifying cracks is to monitor the stiffness matrix. However, different problematics arise when using this method; firstly, the approach does not cover all damage types, secondly the stiffness matrix is typically not known in experimental tests, and thirdly the method quickly becomes trivial in finite element analyses when more advanced elements, e.g. shells and solids, are used. Consequently, employment of a more general and robust methodological procedure is necessary, hence in the present chapter such a procedure will be presented and its applicability will be verified on the basis of the cantilevered finite element model illustrated in Fig. 2.1a and the damage-introduced version of the model shown in Fig. 2.1b. The introduced damage is a longitudinal crack with a length corresponding to a

tenth of the entire tube length,  $L$ , placed with the center at  $x/L = 2/3$  from the clamped end and with a thickness such that it goes through the shell, unless stated otherwise. It is noticed that in the analyses of the model, no experimental tests will be conducted but throughout the methodology, focus will be on usability in both experimental tests and finite element analyses.

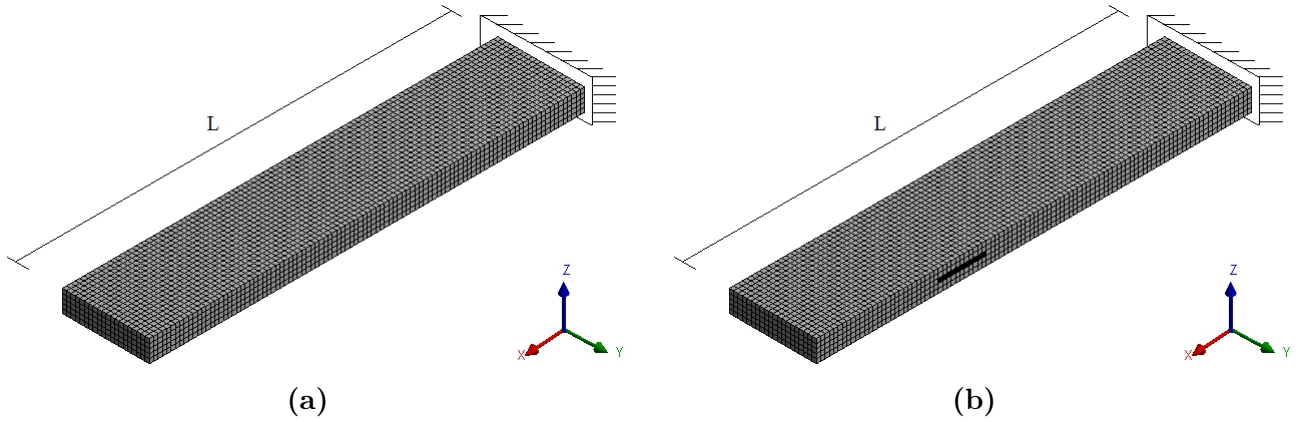


**Fig. 2.1:** Cantilevered finite element model used for validation of damage identification method. (a) Intact model. (b) Crack-introduced model with the crack placed at  $x/L \in [0.62; 0.72]$ . The crack goes through the shell.

The model shown in Fig. 2.1 is a hollow cantilevered rectangular tube with an orthotropic material (see e.g. Section 4.2 and Appendix A), discretized by use of second order shell elements (described in Subsection 4.5.1). On the basis of this finite element model, level 1, level 2 and level 3 damage identification will be conducted in Sections 2.2 - 2.4. Before this, the general theory of modal analysis is described in Section 2.1.

## 2.1 Modal analysis

Introductory in the present chapter, it is described how the damage identification will be based on modal analysis, from which eigenfrequencies and mode shapes are extracted. The equations of motion (2.1) compose the governing discrete, time-invariant mathematical basis for modal analysis. However, the specific application of (2.1) differs in the type of analysis. In the present project, two general modal analysis types, in the form of free vibration and forced-response vibration, are conducted. In Subsections 2.1.1 and 2.1.2, the specific application of (2.1) for the two types are derived mathematically.

### 2.1.1 Parameter extraction of free-response system

The numerical modal parameters will be extracted from finite element free-response analyses. In Section 4.4, it is shown that for the Whisper 500 blade, the modes in the frequency intervals of interest are very lightly damped. Furthermore, studies in e.g. [33] suggest that the impact of structural damping to the vibration modes of wind turbine blades is small, and therefore it is chosen to omit damping in all finite element analyses throughout the report, such the free-response analyses are described by the homogeneous equation system

$$M\ddot{\mathbf{x}} + K\mathbf{x} = \mathbf{0}. \quad (2.4)$$

The expression in (2.4) can be manipulated into an eigenvalue problem with information about the eigenfrequencies in the eigenvalues and information about the mode shapes in the eigenvectors. Several eigenvalue problem formulations exist, and here it is chosen to use the symmetric eigenvalue problem derived with a Cholesky-based congruence transformation, such

$$\exists L, \mathbf{z} : M = LL^T \wedge \mathbf{x} = (L^T)^{-1} \mathbf{z} \Rightarrow M(L^T)^{-1} \ddot{\mathbf{z}} + K(L^T)^{-1} \mathbf{z} = \mathbf{0} \quad (2.5)$$

where  $L^T$  is the transposed of  $L$ . Multiplying (2.5) with  $L^{-1}$  yields

$$I\ddot{\mathbf{z}} + \tilde{K}\mathbf{z} = \mathbf{0} \quad \because \quad \tilde{K} = L^{-1}K(L^T)^{-1}, \quad (2.6)$$

which can be solved in traditional manner, hence

$$\exists \mathbf{v} \neq \mathbf{0} : \mathbf{z}(t) = \mathbf{v}e^{j\omega_n t} \Rightarrow \tilde{K}\mathbf{v} = \omega_n^2 \mathbf{v} \quad (2.7)$$

where  $\mathbf{v}$  is an eigenvector, the eigenvalue  $\omega_n^2$  is the undamped eigenfrequency squared,  $j$  is the imaginary number,  $I$  is the identity matrix, and  $\tilde{K}$  is the mass-normalized stiffness matrix. When applying (2.7), both the eigenvalues and eigenvectors will become real-valued. Furthermore, the eigenvectors will form a fully-ranked orthonormal set which can be used to decouple the undamped equations of motion (2.1).

In all the coming finite element free-response analyses, the eigenvalue problem in (2.7) is employed. By doing so for the model illustrated in Fig. 2.1a, the first seven eigenfrequencies become the ones presented in Table 2.1.

**Table 2.1:** Eigenfrequencies of the cantilevered rectangular shell tube. The results are obtained through finite element free-response analysis.

Mode number	Mode type	Eigenfrequency [Hz]
1	Bending around $y$ -axis	6.55
2	Bending around $z$ -axis	22.84
3	Twisting	31.24
4	Bending around $y$ -axis	32.76
5	Bending around $y$ -axis	70.99
6	Twisting	80.51
7	Bending around $y$ -axis	105.90

### 2.1.2 Parameter extraction of forced-response system

In the experimental tests, the modal analyses are conducted as forced-response analyses, hence the modal parameters cannot be extracted simply by solving an eigenvalue problem. Instead, a spatio-temporal kinematic response is measured and subsequently transformed into a frequency-domain response, namely frequency response functions, from which the modal parameters can be extracted.



Mathematically, a frequency response function,  $h(j\omega)$ , can be derived by Laplace transformation of (2.1), assuming that the initial conditions are zero such

$$(Ms^2 + Cs + K)\mathbf{X}(s) = \mathbf{R}(s) \Leftrightarrow \mathbf{X}(s) = (Ms^2 + Cs + K)^{-1}\mathbf{R}(s), \quad (2.8)$$

where  $H(s) = (Ms^2 + Cs + K)^{-1}$  is the so-called transfer function matrix with the complex-valued variable  $s$ . Evaluating  $H$  along the imaginary axis, i.e.  $s = j\omega$ , yields the frequency response function matrix

$$H(j\omega) = (-\omega^2 M + j\omega C + K)^{-1}, \quad (2.9)$$

by which the mathematical and physical meaning of a frequency response function is indicated. Furthermore, since Laplace transformation is a linear operation, (2.9) implies that the general linearity assumption is not violated. In the experimental tests, accelerations are measured, thus each frequency response function,  $h(j\omega)$ , must be expressed on the basis of these kinematic quantities. This is easily done as

$$h_{\text{acc}}(j\omega) = -\omega^2 h(j\omega), \quad (2.10)$$

because multiplication in Laplace domain corresponds to differentiation in time domain. The coming descriptions will all be based on the displacement frequency response function, i.e.  $h(j\omega)$ .

Since the system matrices,  $M$ ,  $C$  and  $K$ , are not known in the experimental tests, the frequency response functions are derived by use of another approach. This approach is based on spectral analysis, and in the following the approach will be described to the necessary extent. Furthermore, the methodological approach is documented in the MATLAB files `input_data.m` and `spectral_analysis.m` which both are parts of the signal analysis MATLAB pseudocode presented in Appendix B. For a more detailed theoretical description of signal analysis, see e.g. [34].

### Spectral analysis for derivation of frequency response function

When performing an experimental test, the measurements will contain an amount of inherent random noise. Likewise, the time-dependent response of a high-frequency finite element analysis can also be contaminated by noise due to ill discretization in the high-frequency modes. These noise contributions can, however, be reduced significantly in the signal processing that comes ahead of the spectral analysis. This will be described in Section 3.4.

In the following description, no distinctions will be made between the signals obtained by experiments and finite element analyses, respectively, thus each displacement response is consistently denoted  $x(t)$ , while the impulse loads for both the experimental tests and the finite elements are denoted  $r(t)$ . Each frequency response function is derived on the basis of spectral densities. The first step is to determine the correlation functions of  $x(t)$  and  $r(t)$ ,

$$R_{ik}(\tau) = \lim_{T \rightarrow \infty} \frac{1}{T} \int_0^T i(t)k(t + \tau)dt, \quad i, k = x, r \quad (2.11)$$

where  $T$  is the period of the signal and  $\tau$  is the time increment. Evidently, when  $i = k$  the expression in (2.11) is the auto-correlation function, and when  $i \neq k$  it is the cross-correlation function. The correlation functions indicate the similarity of the two signals with a time-lag applied to one of the signals. On the basis of the correlation functions, the spectral densities can be derived by Fourier transformation, thus

$$S_{ik}(\omega) = \frac{1}{2\pi} \int_{-\infty}^{\infty} R_{ik}(\tau) e^{-j\omega\tau} d\tau, \quad i, k = x, r, \quad (2.12)$$

in which  $i = k$  yields the real-valued power spectral densities and  $i \neq k$  the complex-valued cross-spectral densities. The cross-spectral densities are Hermitian symmetric about the origin of the frequency axis, i.e. the real part is an even function while the complex part is an odd function, thus implying that the power spectral densities constitute even functions. These symmetry conditions are utilized in the signal analysis MATLAB pseudocode, see `spectral_analysis.m`, where one-sided spectra are generated instead of full two-sided spectra. Hereby, each frequency response function obtained by

$$S_{xx}(\omega) = |h(j\omega)|^2 S_{rr}(\omega) \quad (2.13a)$$

$$S_{rx}(\omega) = h(j\omega) S_{rr}(\omega) \quad (2.13b)$$

$$S_{xx}(\omega) = h(j\omega) S_{xr}(\omega) \quad (2.13c)$$

spans the frequency interval  $f \in [0; f_{\max}]$  and is based on one input and one output. The expression in (2.13a) yields a real-valued frequency response function, thus only containing information about the magnitude of the transfer function. On the contrary, the expressions in (2.13b) and (2.13c) both result in a complex-valued frequency response function, which means that both magnitude and phase information are obtained. Therefore, it is chosen to employ one of these two expressions in the spectral analyses, namely (2.13b). In theory, this should provide the same frequency response function as (2.13c), but since total consistency in measurements is seldom, due to especially noise, the two expressions will generally yield slightly different frequency response functions. In general, (2.13b) should be used in situations where the system output is expected to be more noisy than the input, while (2.13c) should be used when the input is expected to be most noise-contaminated. A way to check the consistency of  $h(j\omega)$  is by calculating the so-called coherence function,  $\gamma^2$ , given by

$$\gamma^2 = \frac{|S_{xr}(\omega)|^2}{S_{xx}(\omega) S_{rr}(\omega)}, \quad (2.14)$$

i.e. the coherence function represents the fractional portion of the mean square value at the output signal that is contributed by the input at each frequency measurement.  $\gamma^2 = 1$  indicates total consistency while  $\gamma^2 = 0$  indicates that the input signal and output signal are completely unrelated. If  $\gamma \in ]0; 1[$ , the following three possible physical situations exist:[34]

- Extraneous noise is present in the measurements.
- The system relating the input signal and output signal is non-linear.
- The output signal is an output due to multiple inputs.

The coherence function can easily be obtained in the modal analysis software, see e.g. Chapter 3, and also via the signal analysis MATLAB pseudocode in which it is included in `spectral_analysis.m`. Especially throughout the experimental tests, the coherence function will be used to examine the amount of noise contamination.

### Extraction of modal parameters from frequency response functions

Since a frequency response function is based on one input load and one output response, several excitation points and response measurement points will lead to several frequency response functions which can be gathered in a frequency response function matrix. If the number of excitation points equals the number of response measurement points, a symmetric quadratic matrix is constituted. The symmetry exists because of the symmetry of the system matrices,  $M$ ,  $C$  and  $K$ , and it implies that only a row or a column of the frequency response matrix is necessary to extract the modal parameters.

Finite element forced-response analyses are conducted of the model in Fig. 2.1a with three excitation and response measurement points placed along on of the topmost longitudinal edges, evenly spaced from the clamped end. The excitation type used in the analyses is an impulse load in  $z$ -direction, thus simulating a typical hammer hit. The finite element analyses are transient analyses with an implicit solution scheme, namely the Newmark integration method. In Appendix C, a tutorial on how to conduct hammer hit-based modal analysis in ANSYS Workbench is provided.

In Fig. 2.2, the resulting frequency response matrix,  $H(j\omega)$ , is illustrated by use of the signal analysis MATLAB pseudocode in Appendix B. By close inspection of the matrix, it is seen that the reciprocity condition  $H_{lm}(j\omega) = H_{ml}(j\omega)$  applies, i.e. the matrix is symmetric. Furthermore, it is seen that the eigenfrequencies, located at the peaks of the frequency response functions, are in agreement with the results for the bending modes around the  $y$ -axis and the two twisting modes obtained via an eigenvalue problem formulation, see Table 2.1.

The frequency response functions presented in Fig. 2.2 are derived directly on the basis of the displacement responses obtained through finite element analyses, and the modal parameters can simply be extracted by peak picking. However, this parameter extraction method is highly sensitive to measurement noise and effects from adjacent modes, hence the method is best suited for structures with light damping and well separated modes. As mentioned, the structures treated in the present report are lightly damped but as it is seen in Fig. 5.1, some modes are coupled for the Whisper 500 blade and also for the GE 1.5 XLE blade, thus the peak picking method is unsuitable. Instead, it is chosen to use a curve fitting method in which an analytical rational expression of the frequency response function is fitted to the measurement-based frequency response function. In particular, the rational fraction polynomial- $z$  method is employed because of its robustness and because it facilitates multiple inputs and multiple outputs in one curve fitting process. By use of the rational fraction polynomial- $z$  method, the analytical matrix-fraction  $p$ -order model

$$H_{\text{syn}}(j\omega) = \sum_{k=0}^p z^k \alpha_k \left( \sum_{k=0}^p z^k \beta_k \right)^{-1} \quad (2.15)$$

is fitted to the measurement-based frequency response function matrix which is assumed to be of the size  $c \times d$ , i.e.  $c$  outputs and  $d$  inputs. In (2.15),  $H_{\text{syn}}$  is the synthesized, analytical frequency

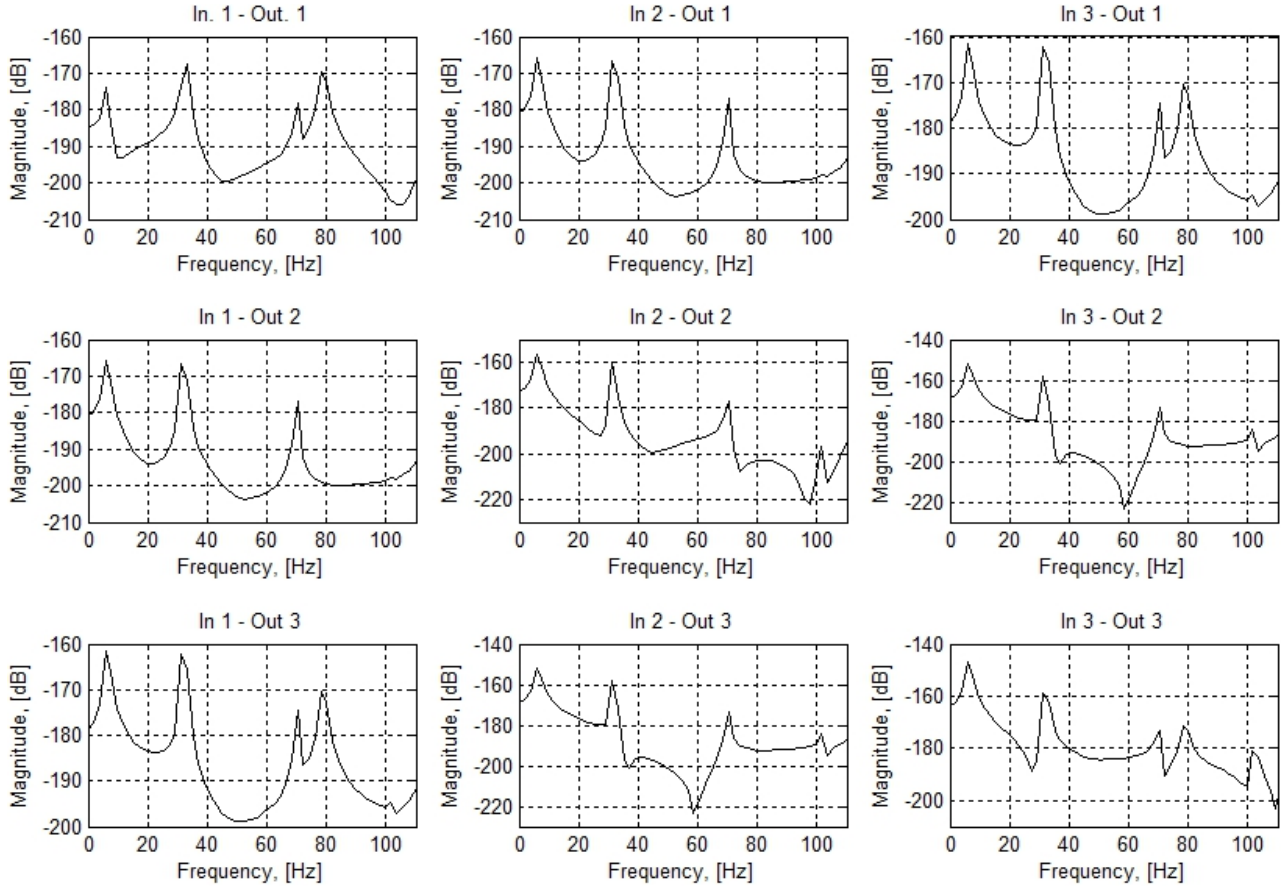


**Fig. 2.2:** Frequency response functions for the cantilevered rectangular shell tube with three excitation points (In) and three response measurement points (Out).

response function matrix, while  $a_k \in \mathbb{C}^{c \times d}$  and  $b_k \in \mathbb{C}^{d \times d}$  are the unknown polynomial coefficient matrices of the pseudonumerator matrix,  $N(j\omega) = \sum_{k=0}^p z^k \alpha_k$ , and pseudodominator matrix,  $D(j\omega) = \sum_{k=0}^p z^k \beta_k$ , respectively. Lastly,  $z$  is a so-called  $z$ -domain function given by

$$z = e^{j\omega\Delta t} \quad (2.16)$$

in which  $\Delta t$  is the sampling time. Hence, the only unknowns of (2.15) are the polynomial coefficient matrices,  $\alpha$  and  $\beta$ , that can be derived through a minimization problem in which the residual,  $Re$ , between the analytical expression (2.15) and the measurement-based frequency response function matrix is minimized in the frequency interval of interest, i.e.

$$\exists \hat{\alpha}, \hat{\beta} : Re = \min \left\{ H_{\text{syn}}(j\omega) - H(j\omega) \right\}. \quad (2.17)$$

When the polynomial coefficients are derived from (2.17), the synthetic frequency response function matrix (2.15) is obtained and can, as a validation measure, be compared with the measurement-based counterpart, see e.g. Section 3.4 where this is done for the Whisper 500 blade. Subsequent of the validation, modal parameters can be extracted implicitly from  $H_{\text{syn}}(j\omega)$ . Since the asymptotic behavior

$$|H_{\text{syn}}(j\omega)| \rightarrow \infty \quad \text{as} \quad |D(\omega)| \rightarrow 0 \quad (2.18)$$

is present, each pole of  $H_{\text{syn}}(j\omega)$  contains resonance information, i.e. an eigenfrequency and a modal damping constant. This is visualized in Fig. 2.3 where a pole is plotted in the  $s$ -plane. It is noted that a complex conjugate of this mode exists in the third quadrant.

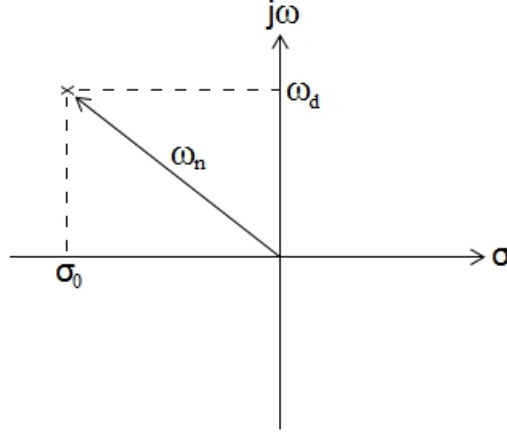


**Fig. 2.3:** Localization of pole in  $s$ -plane with  $\sigma$  being the damping axis and  $j\omega$  the frequency axis.  $\omega_n$  and  $\omega_d$  are the undamped and damped eigenfrequencies, respectively, and  $\sigma_0$  is the modal damping constant.

In Section 4.4, analytical expressions for the modal damping ratio,  $\xi_l$ , and the damped eigenfrequency,  $\omega_{d,l}$ , of mode  $l$  are presented, and it is shown how the complex conjugated poles of a modal equation of underdamped motion, see e.g. (4.5), can be expressed as

$$\lambda_l, \lambda_l^* = -\xi_l \omega_{n,l} \pm j\omega_{d,l}. \quad (2.19)$$

On the basis of Fig. 2.3, the formulation in (2.19) implies that the undamped and damped eigenfrequencies plus the modal damping ratio of mode  $l$  are found as

$$\omega_{n,l} = |\lambda_l| \quad \wedge \quad \omega_{d,l} = \text{Im}(\lambda_l) \quad \wedge \quad \xi_l = -\frac{\text{Re}(\lambda_l)}{|\lambda_l|}, \quad (2.20)$$

in which the poles themselves are obtained as the eigenvalues of the block companion matrix of  $D(j\omega)$ , i.e.

$$\det(C_D - \lambda I) = 0, \quad \text{where} \quad C_D = \begin{bmatrix} 0 & I & 0 & \cdots & 0 & 0 \\ 0 & 0 & I & \cdots & 0 & 0 \\ \cdot & \cdot & \cdot & \cdots & \cdot & \cdot \\ \cdot & \cdot & \cdot & \cdots & \cdot & \cdot \\ 0 & 0 & 0 & \cdots & 0 & I \\ -\hat{\beta}_0^T & -\hat{\beta}_1^T & -\hat{\beta}_2^T & \cdots & -\hat{\beta}_{N-2}^T & -\hat{\beta}_{N-1}^T \end{bmatrix} \quad (2.21)$$

with  $N$  being the number of modes. By solving this eigenvalue problem, a total of  $pd$  poles

will be obtained - with  $p$  being the model order and  $d$  the number of inputs. The non-physical mathematical poles, primarily occurring due to measurement noise, can subsequently be discarded on the basis of a so-called stabilization diagram, which is generated by repeating the analysis for increasing model order  $p$ . For each  $p$ , the poles are calculated from the estimated  $\beta$  coefficients, and here it is utilized that poles corresponding to physically relevant system modes tend to appear at nearly identical locations for each  $p$ , while non-physical mathematical poles tend to be non-consistent in their locations. In Section 3.4, a stabilization diagram obtained during the experimental tests of the Whisper 500 blade is presented.

The last  $m$  rows of the eigenvectors of the eigenvalue problem in (2.21) contain the modal participation factor vectors,  $\kappa_i$ , i.e. a scaling of how each mode participates in the total response. On the basis of  $\kappa_i$  and the valid, physical poles,  $\lambda_i$ , the mode shapes,  $\mathbf{v}_i$ , can be found implicitly via the pole-residue model

$$H_{\text{syn}}(j\omega) = \sum_{i=1}^N \left( \frac{\mathbf{v}_i \kappa_i^T}{j\omega - \lambda_i} + \frac{\mathbf{v}_i^* \kappa_i^H}{j\omega - \lambda_i^*} \right) - \frac{LR}{\omega^2} + UR, \quad (2.22)$$

where  $LR \in \mathbb{R}^{c \times d}$  and  $UR \in \mathbb{R}^{c \times d}$  are the unknown lower and upper residuals, respectively, modeling the influence of the out-of-band modes, while the superindexes  $T$ ,  $*$  and  $H$  denote transposed, complex conjugated and Hermitian transpose, respectively. The unknowns in (2.22), i.e.  $LR$ ,  $UR$  and the mode shapes,  $\mathbf{v}_i$ , are, in analogy to (2.17), derived via residual minimization, thus completing the extraction of modal parameters from a forced-response system.

## 2.2 Damage detection

Damage detection is the first level of the damage identification process. In the present section, it will be shown how detecting longitudinal cracks can be based directly on comparison between pre- and post-damage modal parameters, in the form of eigenfrequencies and mode shapes. This is done by use of the model in Fig. 2.1a plus a crack-introduced version of this model, see Fig. 2.1b. As shown in Section 2.1, the eigenfrequencies and mode shapes can be extracted from both free-response analysis and forced-response analysis. For the sake of simplicity, it is chosen to extract the aforementioned modal parameters from free-response analyses concerning the first seven modes.

In Table 2.1, the first seven eigenfrequencies of the system illustrated in Fig. 2.1a are presented. The corresponding eigenfrequencies for the crack-introduced model are derived via a finite element free-response analysis. In Fig. 2.4a the percentage deviation between these eigenfrequencies and the ones of the intact model are visualized. Furthermore, in Fig. 2.4b, a measure is given for the consistency between the mode shapes of the two models, in the form of the modal assurance criterion (MAC), presented in [35],

$$\text{MAC}_{il} = \frac{|\mathbf{v}_i^T \mathbf{v}_l|^2}{\mathbf{v}_i^T \mathbf{v}_i \mathbf{v}_l^T \mathbf{v}_l} \quad (2.23)$$

where  $\text{MAC}_{il} \in [0; 1]$ . A MAC value of zero implies no correlation between the compared mode shapes, while a value of one represents full correlation. The mode shapes are found as the local  $z$ -directional modal displacements in ten evenly spaced points (away from the clamped end)

along the topmost longitudinal edge in the damaged side, i.e. the amount of extraction points is increased compared to the analyses documented in the previous section in order to increase the accuracy of the mode shapes.

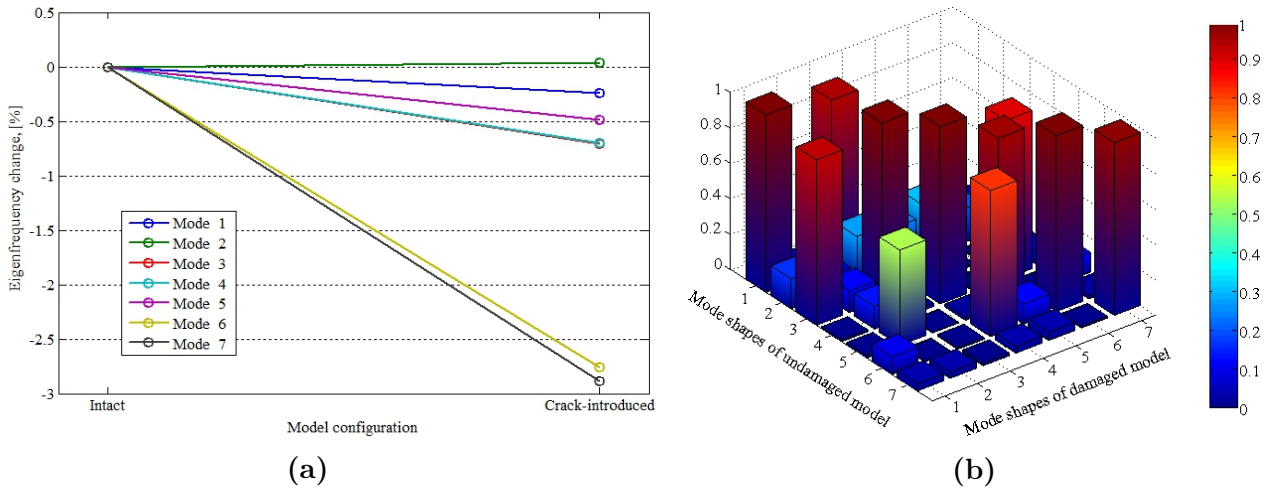


**Fig. 2.4:** Comparison of modal parameters derived from undamaged and damaged cantilevered rectangular shell tube. 2.1. (a) Percentage changes in eigenfrequencies. (b) Correlation between mode shapes in the form of MAC values.

When examining the frequency comparison plot in Fig. 2.4a, it is found that only mode 6 (second twisting mode) and mode 7 (fourth bending mode around  $y$ -axis) yield significant frequency changes. For the mode shapes, the crack primarily changes mode 2 (first bending mode around  $z$ -axis), mode 5 (third bending mode around  $y$ -axis) and mode 7. The MAC value of the latter mode is changed approximately 3 %, the MAC value of mode 5 is changed approximately 5 %, and the MAC value of mode 2 is changed approximately 90 %. This large change of mode 2 is primarily a result of the placement of measurement points, since these are directly above the actual crack edge and will, thus, experience the local deformations of the crack. Consequently, this huge change can generally not be expected.

For the modes higher than the seven processed here, the general tendency is that the deviations between the modal parameters of the intact model and the corresponding parameters of the crack-introduced model increase. Especially the MAC values decrease significantly in the high-frequency bending and twisting modes, thus suggesting that the mode shapes are more sensitive to longitudinal cracks than the eigenfrequencies.

## 2.3 Damage localization

As described in the previous section, the damage detection is based on a general examination of both the eigenfrequencies and the mode shapes. For damage localization, several methods utilizing these modal parameters separately and combined exist. However, most of these methods are based on beam structures and are not suitable for more complex structures because analytical expressions are employed. In the present section, three methods which do not use analytical expressions are tested for localization of the crack shown in Fig. 2.1b, and on the basis of the findings the final choice of damage localization method will be made.

### 2.3.1 Tested damage localization methods

It is chosen to discard methods utilizing only eigenfrequencies because of the inherent shortcoming of these methods; the eigenfrequencies are global parameters, making them inapplicable for localization of multiple damages. Furthermore, it is proven in the previous section that the eigenfrequencies are less sensitive to longitudinal cracks than the mode shapes, and since environmental effects can account for up to 5 % changes in eigenfrequencies [36], these are typically not suitable for damage identification besides in numerical analyses and controlled laboratory tests. Consequently, all the damage localization methods tested with the models shown in Fig. 2.1 utilize only the mode shapes or their derivatives, e.g. mode shape curvature (second order derivative).

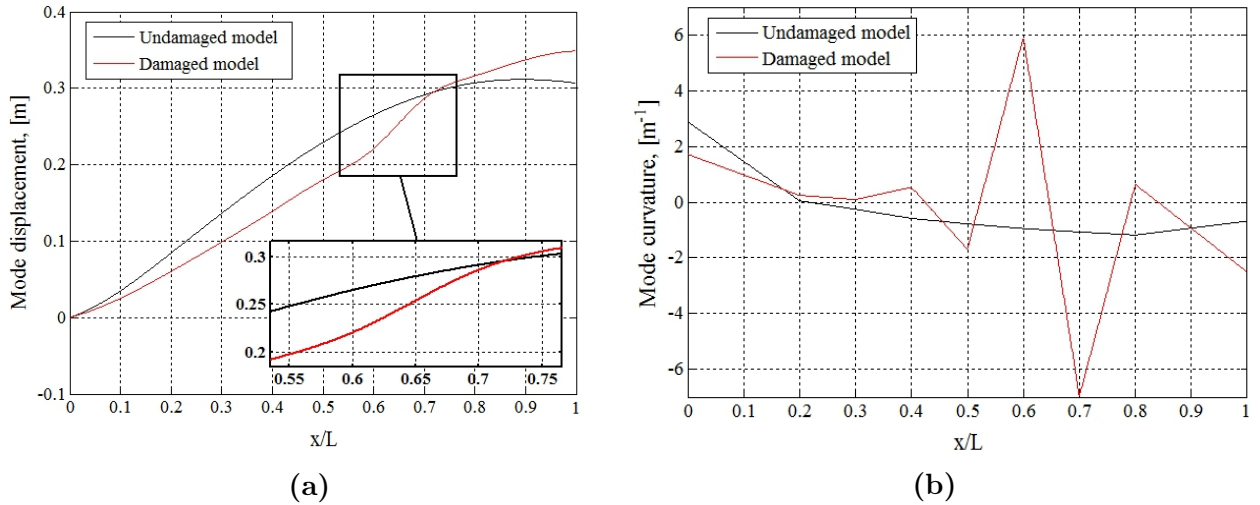


**Fig. 2.5:** Comparison of third mode displacement patterns of undamaged and damaged cantilevered rectangular shell tube. (a) Mode shapes. (b) Mode shape curvatures.

In Fig. 2.5, plots of the third mode shape and mode shape curvature of the models in Fig. 2.1 are given. Evidently, there are deviations between the results from the undamaged model and the damaged model, especially between the measurement points placed in  $x/L = 0.6$  and  $x/L = 0.7$  - note that the crack starts at  $x/L \approx 0.62$  and ends at  $x/L \approx 0.72$ . These deviations are to a certain extent observed for all the seven modes and the basic idea of all three localization methods is to exploit the deviations. Below, a listing of the three methods is given, and subsequently they are described in details and utilized to locate the crack in the model shown in Fig. 2.1b.

- COMAC method; utilizing the mode shapes of both the undamaged and damaged system/model to calculate coordinate modal assurance criteria (COMAC).
- MSC method; direct comparison of the mode shape curvatures (MSC) of both the undamaged and damaged system/model).
- WA method; utilizing the mode shapes or the  $n$ th derivative counterparts of the damaged system/model to conduct wavelet analysis (WA).

For all three methods it is chosen to employ a preliminary data analysis procedure in which extra measurements point are added by cubic spline interpolation to smooth the mode shapes



such that no artificial singularities are introduced. In this way, 100 data points are obtained between each set of adjacent measurement points, thus resulting in a total of 1000 data points for each mode shape and mode shape curvature. This is also the case for the plots in Fig. 2.5.

### COMAC method

In Fig. 2.5a, it is clearly seen how deviations between the mode shapes of the undamaged cantilevered rectangular shell tube and those of the damaged counterpart occur. The idea of the coordinate modal assurance criterion (COMAC) method, as presented in [35], is to expand the MAC formulated in (2.23), such that the measurement degree of freedom (d.o.f.) contributing negatively to the MAC value are localized. This is done through

$$\text{COMAC}_g = \frac{\left(\sum_{i=1}^N |v_{u,gi}v_{d,gi}|\right)^2}{\sum_{i=1}^N v_{u,gi}^2 \sum_{i=1}^N v_{d,gi}^2} \quad (2.24)$$

where  $g$  indicates the  $g$ th measurement point,  $N$  is the number of mode shapes, and  $v_{u,gi}$  and  $v_{d,gi}$  are the  $g$ th component of the  $i$ th undamaged mode shape and damaged mode shape, respectively. In analogy to the MAC value,  $\text{COMAC} \in [0; 1]$  where a value of zero implies no correlation while a value of one implies full correlation.

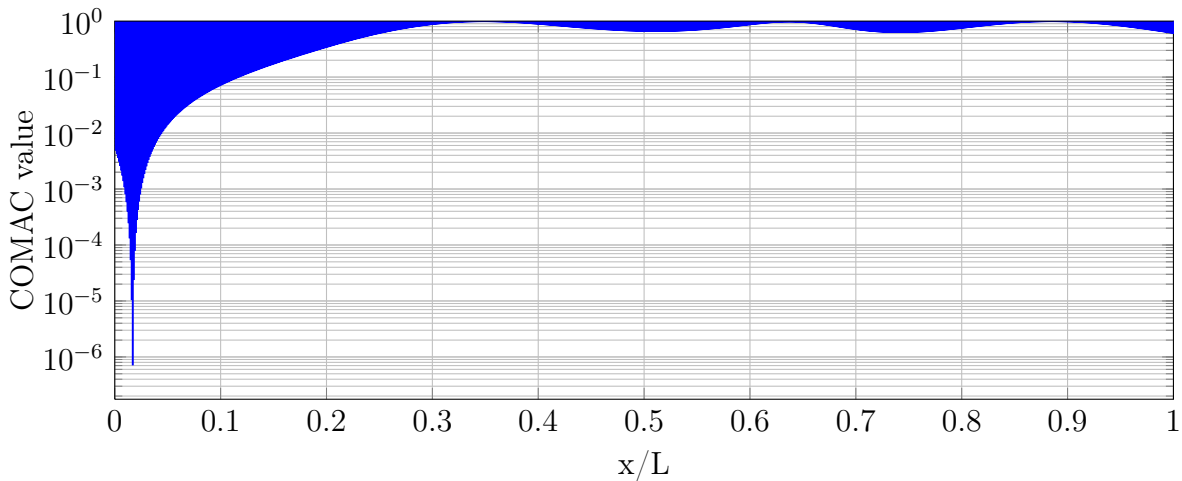


**Fig. 2.6:** Semilogarithmic plot of COMAC values for all mode shapes of undamaged and damaged cantilevered rectangular shell tube. The damage is placed at  $x/L \in [0.62; 0.72]$ .

In Fig. 2.6, the COMAC values obtained for all the undamaged and damaged cantilevered rectangular shell tube are plotted in a semilogarithmic coordinate system. Evidently, since the crack is introduced at  $x/L \in [0.62; 0.72]$ , the longitudinal crack is not localized correctly by use of the COMAC method. It is, however, noticed that the COMAC method succeeds at localizing the crack for few of the higher modes when these are treated separately.

### MSC method

As suggested in [37], the mode shape curvatures (MSCs) of the undamaged and damaged model, respectively, are compared by use of

$$\text{MSC}_g = \sum_{i=1}^N |v''_{d,gi} - v''_{u,gi}|, \quad (2.25)$$

in which  $v''_{u,gi} = d^2 v_{u,gi}/dx^2$  and  $v''_{d,gi} = d^2 v_{d,gi}/dx^2$  are the  $g$ th element of the  $i$ th mode shape curvature of the undamaged and damaged model, respectively. Each mode shape curvature is approximated by use of the central difference equation, i.e.

$$v''_{gi} = \frac{1}{(\Delta x)^2} (v_{g(i+1)} + v_{g(i-1)} - 2v_{gi}) \quad (2.26)$$

where  $v_{g(i\pm 1)}$  are the  $i \pm 1$ th measurement points, while  $\Delta x$  is the spacing of the measurement points. The applicability of the MSC method for beams is theoretically clear when looking at the governing differential equation

$$\nu(x) = \frac{M(x)}{EI}, \quad (2.27)$$

with  $\nu(x)$  being the curvature at location  $x$  along the length of the beam,  $M(x)$  the bending moment along the length of the beam,  $E$  the modulus of elasticity and  $I$  the moment of inertia. Hence, the curvature is inversely proportional to the flexural stiffness,  $EI$ , which implies that a reduction of stiffness associated with damage will lead to an increase in curvature. Therefore, deviations between pre- and post-damage curvature mode shapes will, in theory, be largest in the damaged region. When examining Fig. 2.5b, it is found that this also holds for the cantilevered rectangular shell tube since the numerically largest deviations occur at the initial measurement points closest to the crack, i.e.  $x/L = 0.6$  and  $x/L = 0.7$ . In Fig. 2.7, the numerical deviations between all the pre- and post-damage mode shape curvatures of the cantilevered rectangular shell tube are visualized. Evidently, the MSC method yields an acceptable prediction of the crack location when all modes are employed, but it is found that mode 7, i.e. the fourth bending moment around the  $y$ -axis, fails to yield an acceptable localization when treated separately.

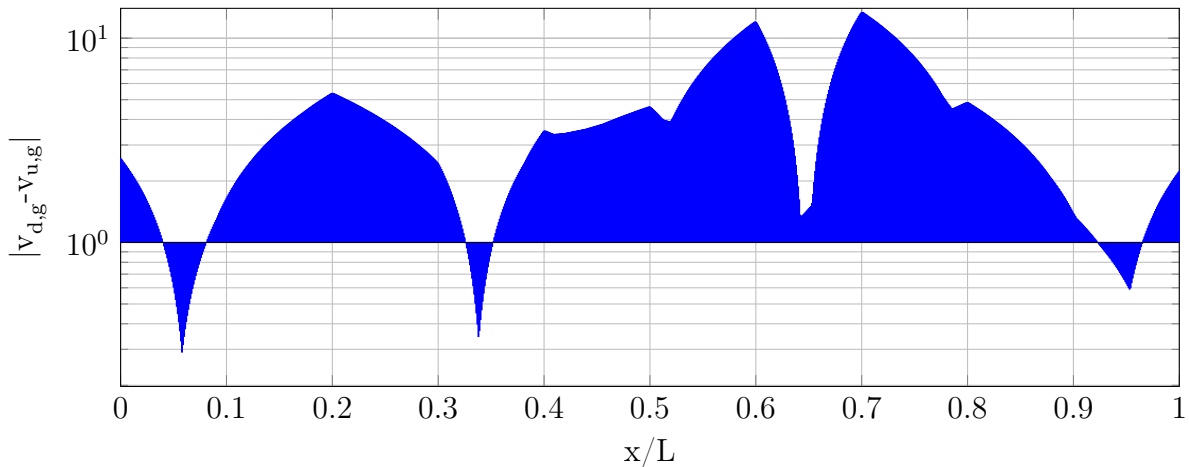


**Fig. 2.7:** Semilogarithmic plot of comparisons of mode shape curvatures of undamaged and damaged cantilevered rectangular shell tube. The damage is placed at  $x/L \in [0.62; 0.72]$ .

Although the MSC method generally locates the crack acceptably, a shortcoming of the method is also found since the numerically largest deviations between all the pre- and post-damage mode shape curvatures occur at  $x/L = 0.6$  and  $x/L = 0.7$ , i.e. the initial measurement points nearest the crack. This implies that the method is highly sensitive towards the amount of physical measurement points.

### WA method

The idea of wavelet analysis (WA) is to decompose a time series into time-frequency space and then determine modes of variability and their varying in time. In the WA method, wavelet transforms are utilized to locate potential discontinuities in the post-damaged spatial mode shape series or the  $n$ th derivative counterpart. The method has been widely employed for damage localization of simple one- and two-dimensional structures such as beams and plates, see e.g. [38,39].

Like the well-known Fourier transform, the continuous wavelet transform (CWT) uses inner products to measure the similarity between, e.g., a spatial signal in Hilbert space of measurable, square-integrable one-dimensional functions,  $f(x) \in \mathbf{L}^2(\mathbb{R})$ , and an analyzing function. In the Fourier transform, the analyzing functions are complex exponentials, whereas the analyzing function in the CWT is a so-called wavelet,  $\psi(x) \in \mathbf{L}^2(\mathbb{R})$ , which is a waveform satisfying the admissibility condition

$$\int_{-\infty}^{\infty} \frac{|\Psi(\omega)|^2}{|\omega|} d\omega < \infty \Rightarrow \Psi(0) = \int_{-\infty}^{\infty} \psi(x) dx = 0, \quad (2.28)$$

with  $\Psi(\omega)$  being the Fourier transform of  $\psi(x)$ . The wavelet can be both real- and complex-valued. However, in the present report, the use of real-valued wavelets is sufficient. The latter expression in (2.28) shows that a wavelet must have an average value of zero. Another essential characteristic of the wavelet is the effectively limited duration of the waveform. Often in wavelet analysis, irregular and asymmetric wavelets are chosen such a signal is partitioned into shifted and scaled versions of the original wavelet and due to the irregularity, signals with abrupt changes can be better analyzed with a wavelet than with a smooth sinusoid obtained from, e.g., a Fourier transform.

By comparing  $f(x)$  to  $\psi(x)$  at various scales,  $a_i \in \mathbb{R} \setminus \{0\}$ , and positions,  $b_i \in \mathbb{R}$ , the CWT function

$$\text{CWT}(a,b; f(x), \psi(x)) = \frac{1}{\sqrt{|a|}} \int_{-\infty}^{\infty} f(x) \psi^* \left( \frac{x-b}{a} \right) dx \quad (2.29)$$

is obtained as the inner product of  $f(x)$  and the so-called wavelet family, i.e. functions constructed from dilations and translations of  $\psi$ ,

$$\psi_{a,b}(x) = \frac{1}{\sqrt{|a|}} \psi \left( \frac{x-b}{a} \right). \quad (2.30)$$

Evidently, large values of  $a$  correspond to big wavelets and consequently coarse features of  $f(x)$ , while low values of  $a$  correspond to small wavelets and fine details of  $f(x)$ . In (2.30), the factor  $1/\sqrt{|a|}$  is applied as a normalization operator such that  $\|\psi_{a,b}(x)\| = \|\psi(x)\|$ .

By introducing the concept of convolution, the wavelet transform introduced in (2.29) can be restated on the basis of

$$\begin{aligned} \exists \psi_a^*(x) = \frac{1}{\sqrt{|a|}} \psi\left(\frac{-x}{a}\right) \implies \text{CWT}(a,b; f(x), \psi(x)) &= (f * \psi_a^*)(b) \quad \therefore \\ (f * \psi_a)(b) &= \int_{-\infty}^{\infty} f(x) \psi_a(b-x) dx, \end{aligned} \quad (2.31)$$

thus obtaining a compact formulation for the wavelet coefficients. This formulation will be utilized in the coming derivations.

Abrupt changes in signals result in CWT coefficients with large absolute values, thus, in theory, peaks of the coefficients for the post-damage mode shape series will occur in the crack area. Studies in e.g. [38,39], however, suggest that the effectiveness of wavelet analysis is typically increased when the derivatives of the mode shapes are examined. This can easily be exploited since the studies in [40] prove that

$$\exists \theta(x) : \psi(x) = (-1)^n \frac{d^n \theta(x)}{dx^n} \implies \int_{-\infty}^{\infty} \theta(x) dx \neq 0 \quad (2.32)$$

for wavelets with a fast decay and  $n$  vanishing moments, i.e.

$$\int_{-\infty}^{\infty} x^k \psi(x) dx = 0, \quad k = 0, 1, \dots, n-1. \quad (2.33)$$

In (2.33), it is stated how a wavelet has  $n$  vanishing moments when  $k = n-1$ . This means that a wavelet with  $n$  vanishing moments is orthogonal to polynomials up to degree  $n-1$ , thus resulting in zero-valued wavelet coefficients for these polynomials. When expressing the wavelet with  $n$  vanishing moments as the  $n$ th order derivative of  $\theta(x)$ , which is referred to as the smoothing function, the resulting wavelet transform becomes

$$\text{CWT}(a,b; f(x), \theta(x)) = a^n \frac{d^n}{db^n} (f * \theta_a^*)(b), \quad \theta_a^*(x) = \frac{1}{\sqrt{|a|}} \theta\left(\frac{-x}{a}\right), \quad (2.34)$$

from which it is seen that the CWT is found as the  $n$ th derivative of the data signal multiplied by a wavelet with  $n$  vanishing moments.

Several wavelet types have been employed in the analyses of the cantilevered rectangular shell tube, and it is found that a real-valued Gaussian wavelet with 4 vanishing moments, i.e.

$$\psi(x) = \frac{d^4}{dx^4} (C_4 e^{-x^2}) = 4C_4 e^{-x^2} (4x^4 - 12x^2 + 3), \quad (2.35)$$

yields the best results in the identification analyses. The constant in (2.35) is found such the Euclidean norm  $\|d^4 \theta(x)/dx^4\|^2 = 1$ , and hereby the function plotted in Fig. 2.8 is obtained. By employing scaling and position variables, the plot in Fig. 2.8 is dilated and translated.

By use of the specific Gaussian wavelet, the wavelet coefficients for  $a \in [1; 30]$  illustrated in Fig. 2.9 are obtained for the third mode of the cantilevered rectangular shell tube, and it is clearly seen that the WA method locates the crack acceptably. In order to obtain the coefficients, cubic extrapolation of both ends of the mode shape series have been conducted to

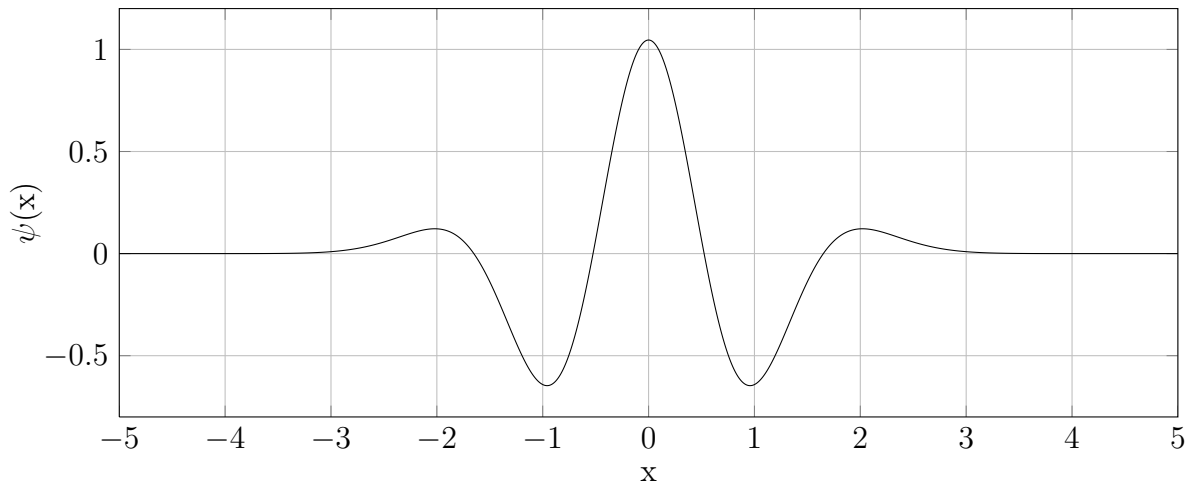


**Fig. 2.8:** Original Gaussian wavelet with 4 vanishing moments.

reduce inherent boundary effects which introduce artificial peaks in the wavelet transform. The occurrence of these effects have been observed in the studies associated with this report and in several other studies, see e.g. [39]. However, by performing wavelet analysis of the data series with extrapolated ends and subsequently truncating the signals back to the original length, the boundary effects have been reduced significantly. In this way, similar results are obtained for the six other modes of the model, i.e. the crack is localized acceptably for all modes.

As seen in Fig. 2.9, the WA method predicts irregularities, such as a crack, at  $x/L = 0.6$  and  $x/L = 0.7$ . This is the same as the results obtained by use of the MSC method, thus both methods allegedly have an inherent shortcoming in the form of high sensitivity towards the amount of physical measurement points.

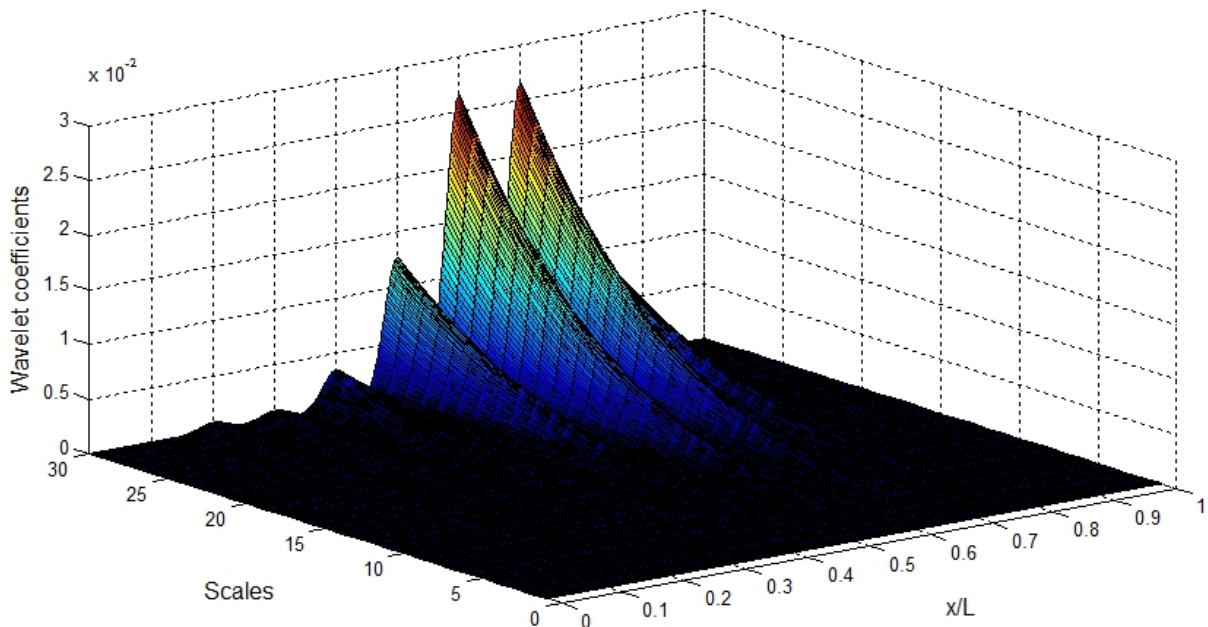


**Fig. 2.9:** CWT coefficients for third mode shape of damaged cantilevered rectangular shell tube. The damage is placed at  $x/L \in [0.62; 0.72]$ .

### 2.3.2 Choice of method

Based on the cantilevered rectangular shell tube shown in Fig. 2.1, three damage localization methods, namely the COMAC method, MSC method and WA method, have been tested. It is found that the COMAC method is inapplicable since it is unable to locate the crack correctly. The two other methods locate the crack acceptably and are therefore considered as applicable for later numerical analyses of the more complex structures, i.e. the Whisper 500 blade and the GE 1.5 XLE blade. However, since experimental tests will yield noise-contaminated signals, white Gaussian noise has been added to the signals obtained in the finite element analyses of the cantilevered rectangular shell tube, and hereby the robustness of the MSC method and the WA method is tested. The results are presented in Appendix D, and here it is found that the MSC method is very sensitive towards noise as it fails to locate the crack for a signal-to-noise ratio (SNR) smaller than 88 dB, see Appendix D for explanation of SNR. The WA method can locate the crack for  $\text{SNR} \geq 40$  dB when the scale interval  $a \in [1; 30]$  is utilized. It is found that the noise-governed wavelet peaks, unlike the damage-governed wavelet peaks, do not increase as the scale is increased, so for, e.g.,  $a \in [1; 100]$ , the WA method can locate the crack for  $\text{SNR} \geq 20$  dB, hence the WA method is very robust. However, it is noticed that the scale cannot be increased unlimited since this will result in diminishing degree of detail in the wavelet transformation and, thus, yield unambiguous damage localization. Still, the WA method is much more robust than the MSC method and therefore the former is preferred for damage localization.

The WA method also has clear advantages when it comes to spatial dimension expansion; the method is, from a computational point of view, easier to expand to two- and three-dimensional analyses, see e.g. [39]. Also, the WA method facilitates assessment of structural damages (level 3 identification) which will be treated in Subsection 2.4. In Appendix E, a two-dimensional wavelet analysis of the damaged cantilevered rectangular shell tube is presented, and it is shown how the crack is localized in analogy to the one-dimensional wavelet analysis approach. Furthermore, the theoretical background of multi-dimensional continuous wavelet transforms is presented. In Appendix F, a MATLAB pseudocode for wavelet analysis is presented. This will be utilized in all coming wavelet analyses. It is noticed that this pseudocode is a general wavelet analysis toolbox, namely YAWTb [41], to which specific files, produced by the authors of this report, have been added.

## 2.4 Damage assessment

As mentioned in Subsection 2.3.2, the WA method also facilitates level 3 damage identification, i.e. damage assessment. In the present section, this will be documented for both crack length and crack depth assessment on the basis of the third mode of the damaged cantilevered rectangular shell tube, see e.g. Fig. 2.5a. This particular mode shape is chosen because it is the one processed in the damage localization documentation in the previous section.

### 2.4.1 Crack length

The damage localization method inherently yields a direct assessment of the crack length. The accuracy of this crack length assessment highly depends on the number of measurement points. For instance, the plot in Fig. 2.9 implies that the crack is placed at  $x/L \in [0.6; 0.7]$ , with the

correct placement being  $x/L \in [0.62; 0.72]$ . This prediction is obtained because initial measurement points are placed with an increment of  $\Delta(x/L) = 0.1$ , thus, even though interpolation is conducted to refine the measurement series, peaks can only occur at  $x/L = 0, 0.1, \dots, 0.9, 1$ . By refining the increment to  $\Delta(x/L) = 0.01$ , and still employing the inter- and extrapolation procedure described in the previous section, an improved localization is obtained. The tendency of significant wavelet coefficients in non-damaged areas is still present, and therefore it is chosen to apply a threshold,  $\Pi$ , so all wavelet coefficients lower than  $\Pi$  at maximum scale are set to zero for all scales. In Fig. 2.10, a two-dimensional plot of the wavelet coefficients are given for the third mode of the damaged cantilevered rectangular shell tube with  $\Delta(x/L) = 0.01$  and  $\Pi = 0.5$ .

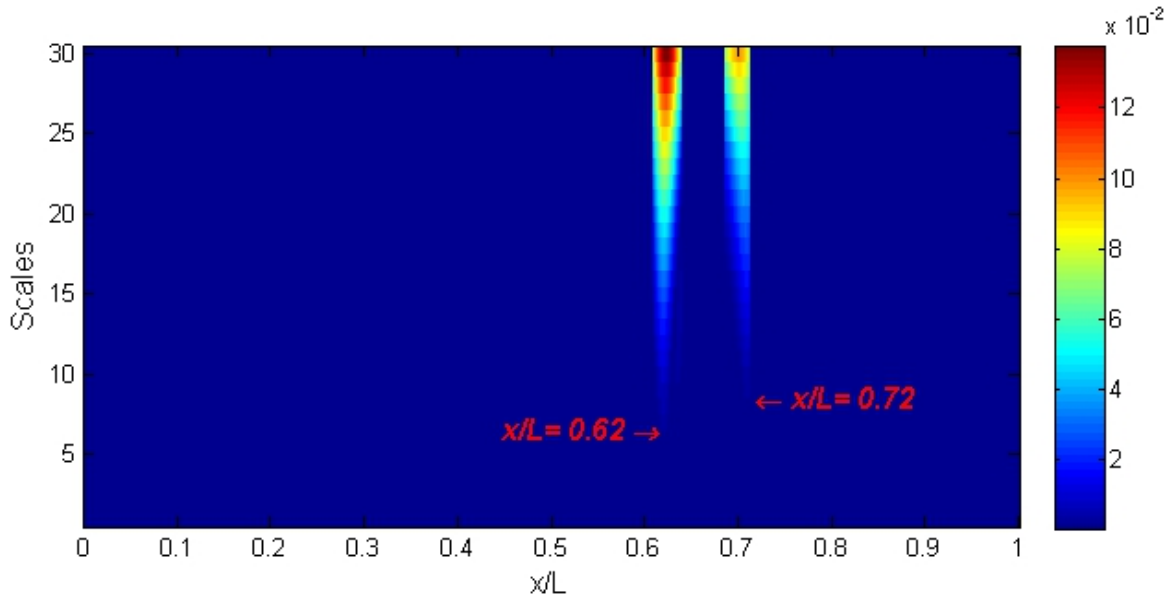


**Fig. 2.10:** CWT coefficients for third mode shape of damaged cantilevered rectangular shell tube. The damage is placed at  $x/L \in [0.62; 0.72]$  and a threshold of  $\Pi = 0.5$  is employed.

As seen in Fig. 2.10, the WA method accurately locates both the crack start and crack end, respectively, hence an accurate assessment of the crack length is obtained. In order to examine the robustness of this approach, it has been employed for a noise-contaminated signal. The result, which can be seen in Appendix D, reveals that an accurate prediction of the crack length is obtained as long as the general WA method succeeds to locate the crack. Therefore, this direct assessment approach will be utilized in the coming analyses of the Whisper 500 blade and the GE 1.5 XLE blade.

## 2.4.2 Crack depth

While the crack length assessment is an inherent result of the crack localization method, the crack depth assessment is conducted as a continuation of the WA method for damage localization; in the sense that the wavelet coefficients are utilized for further analyses. According to [38], each wavelet coefficient satisfies

$$|\text{CWT}(a,b; f, \theta)| \leq \Gamma |a|^{h+\frac{1}{2}} \Leftrightarrow \ln(|\text{CWT}(a,b; f, \theta)|) \leq \ln(\Gamma) + \left(h + \frac{1}{2}\right) \ln(|a|) \quad (2.36)$$

where  $\Gamma$  is an unknown factor and  $h$  is the Hölder exponent<sup>1</sup>. The Hölder exponent, generally, provides information about the differentiability of a function, e.g.  $h = 1.5$  implies that the function is one time differentiable but not two times differentiable. Thus, the Hölder exponent describes the type of singularity and should therefore, in theory, be constant, i.e. independent of the crack depth, which suggests that the factor,  $\Gamma$ , characterizes the depth of the crack. Consequently,  $\Gamma$  is denoted the intensity factor.

On the basis of (2.36), the Hölder exponent and the intensity factor can be determined by simple linear regression. This is done for the third mode shape of the cantilevered rectangular shell tube in Fig. 2.1b with different crack depths, stated as dimensionless relative depths,  $v$ , i.e. the fraction between the actual crack depth and the thickness of the shell. The results are plotted in Fig. 2.11, where the linear formula in (2.36) is applied for wavelets coefficient found at  $x/L = 0.62$  for the relative crack depths  $v = \{0.2, 0.4, 0.6, 0.8, 1\}$ . It is noticed that  $v = 1$  corresponds to a crack going through the shell, i.e. the damage scenario treated so far in the analyses.

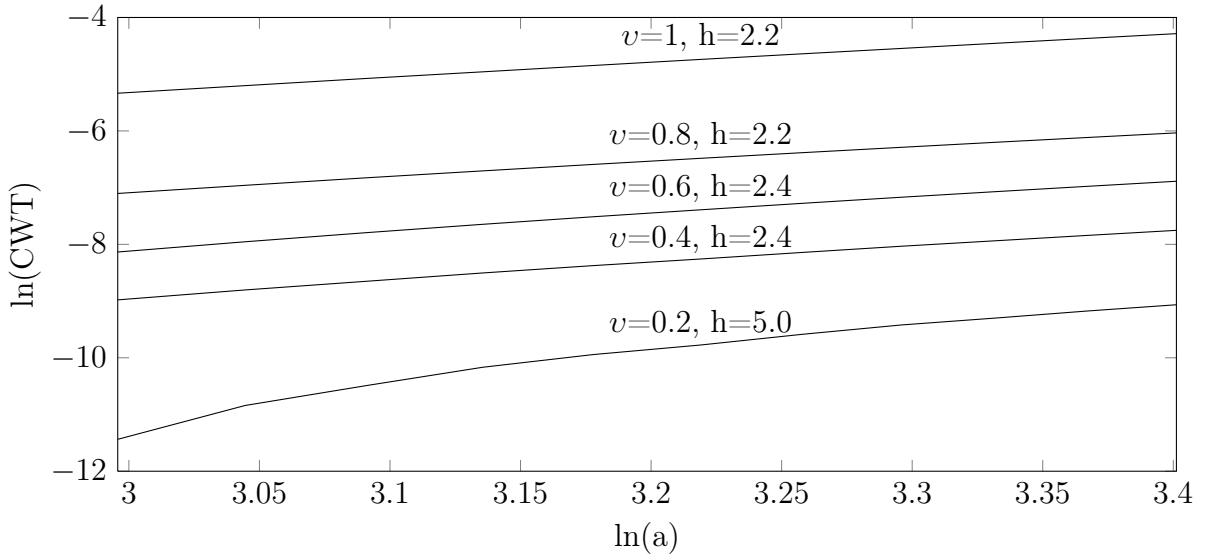


**Fig. 2.11:** Wavelet coefficient, CWT, versus scale,  $a$ , for different crack depth-configurations of the third mode of the cantilevered rectangular shell tube.  $v$  and  $h$  denote relative crack depth and Hölder exponent, respectively.

The plots in Fig. 2.11 are based on the scale interval  $a \in [20; 30]$ , which is chosen because the wavelet transformation fails to distinguish the discontinuities from the remaining signal at the lower scales for the small cracks. Evidently, by employing the aforementioned scale interval, the Hölder exponent, which is found by linear least squares fitting of the latter expression in (2.36), is nearly constant for  $v = \{0.4, 0.6, 0.8, 1\}$ , but for the smallest crack depth, i.e.  $v = 0.2$ , the Hölder exponent is significantly larger. This tendency is also found for the other modes where the differences between the Hölder exponents for each crack depth decrease for the lower modes, which implies that the lowest modes should be utilized. However, for all modes it is found that the crack depth must reach a certain extent before the Hölder exponent stabilizes and, thus, facilitates use of the proposed assessment method. Therefore, the  $v = 0.2$  crack

<sup>1</sup>If  $f$  is a function from an interval  $D \subseteq \mathbb{R}$  into  $\mathbb{R}$ ,  $f$  is said to be Hölder continuous if  $\exists \Gamma, h : |f(x) - f(y)| \leq \Gamma |x - y|^h, x, y \in D$ , where  $h$  is the so-called Hölder exponent.



is discarded and the Hölder exponent is set constant to  $h = 2.3$ , which is the mean of the remaining Hölder exponents. Hereby, the intensity factor can be plotted as a function of the relative crack depth as shown in Fig. 2.12.

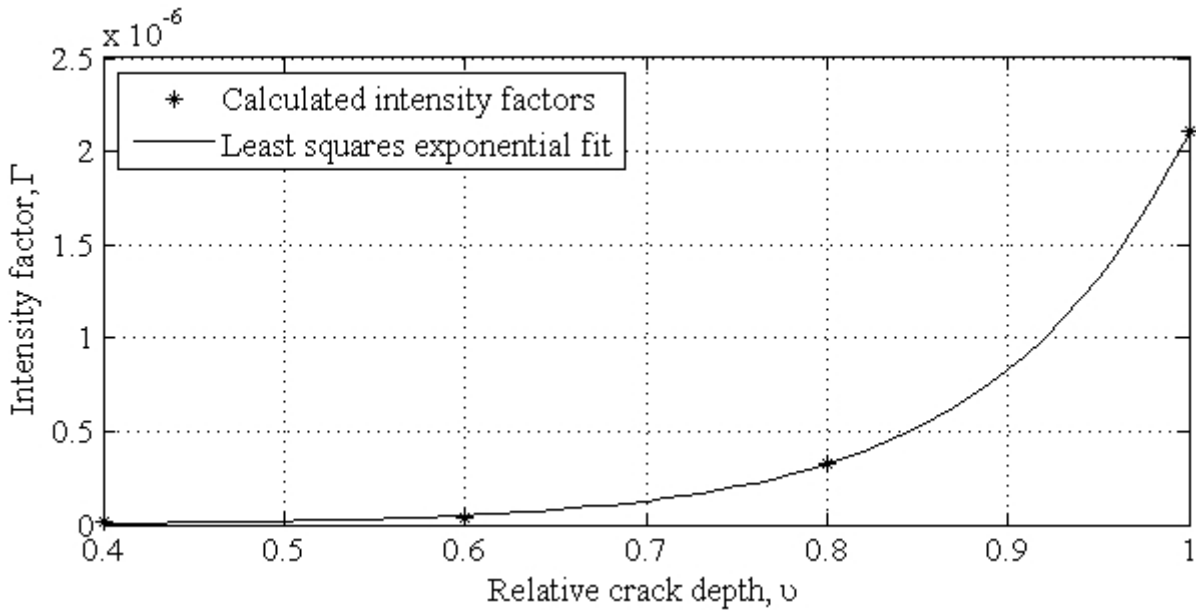


**Fig. 2.12:** Intensity factor,  $\Gamma$ , as function of relative crack depth,  $v$ , for the damaged cantilevered rectangular shell tube.

The idea of the crack depth assessment is, thus, to derive the continuous, analytical intensity function plotted in Fig. 2.12, from which a crack depth, in theory, can be determined. To validate this, a finite element analysis of the cantilevered rectangular shell tube with a  $v = 0.85$  crack has been conducted. The analysis results in  $\Gamma = 0.511 \cdot 10^{-6}$  and since the intensity function predicts  $\Gamma = 0.517 \cdot 10^{-6}$ , acceptable agreement is obtained.

In practice, where the data needed for generating the intensity function are typically not available through experimental tests, an approach could be to use finite element analyses to derive the intensity function. For this approach to be valid, the wavelet coefficients must be similar for, respectively, the numerical and experimental findings, hence the effect of noise-contamination must be examined. This is done in Appendix D where it is found that the method is slightly more sensitive towards noise than the method for localization and crack length assessment. The sensitivity is, however, found acceptable, thus the method can be applied in the analyses of the Whisper 500 blade and the GE 1.5 XLE blade.

It is important to notice that the wavelet coefficients, cf. (2.34), are proportional to the derivatives of the response signal, and therefore the wavelet coefficients, and thus the intensity factors, will change as the crack location changes. Additionally, the wavelet coefficients and intensity factors depend on the wavelet function, i.e. the same function must be used consistently throughout the analyses.

## 2.5 Summary

In the present chapter, a methodology for modal analysis-based level 1, 2 and 3 damage identification has been presented. Hereby, specific methods for, respectively, damage detection (level

1), damage localization (level 2) and damage assessment (level 3) have been chosen on the basis of numerical validation analyses of a cantilevered rectangular shell tube with and without structural damage. The structural damage is a longitudinal crack placed at  $x/L \in [0.62; 0.72]$ , where  $L$  is the length of the model.

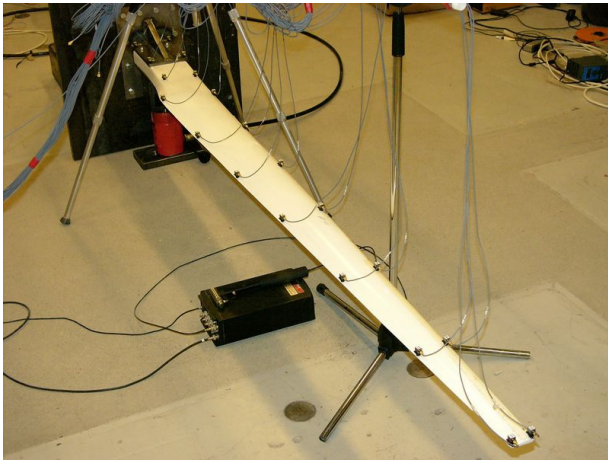
In Section 2.1, the general theory of modal analysis is outlined with emphasis on extraction of modal parameters from free and forced vibrations. These two vibration types are of particular interest because the finite element analyses are conducted as free vibration simulations while the experimental tests are carried out by use of an excitation hammer, yielding forced vibrations.

The first step of damage identification, i.e. damage detection, is based on direct comparisons of the eigenfrequencies and mode shapes extracted from pre- and post-damage configurations. As proven in Section 2.2, especially the mode shapes are sensitive towards structural damages and therefore these will be utilized as the main damage indicator. Additionally, the mode shapes and their derivatives are also employed in the different methods proposed for level 2 damage identification.

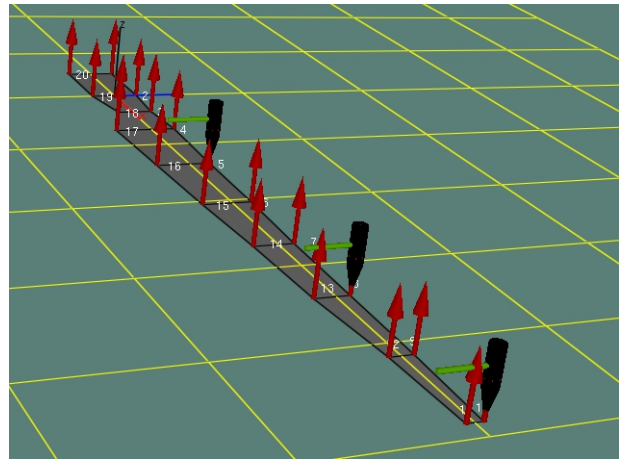
In Section 2.3, level 2 damage identification, i.e. localization, is treated for the cantilevered rectangular shell tube. Three methods, namely coordinate modal assurance criterion (COMAC), mode shape curvature (MSC) and wavelet analysis (WA), are presented and tested. It is found that the COMAC method is inapplicable since it fails to locate the introduced crack correctly, while both the MSC method and WA method succeed in localizing the crack. Both methods, however, have an inherent shortcoming since they highly depend on the number of measurement points. The final choice between the two methods is based on the study conducted in Appendix D, where the spatial mode shape and mode curvature shape signals of the cantilevered rectangular shell tube are contaminated with noise. Here, it is found that the WA method is less sensitive towards noise, thus this method is preferred over the MSC method. Furthermore, the WA method facilitates easy expansion of spatial dimensions, see e.g. Appendix E, plus level 3 damage identification. The latter is proven in Section 2.4 as the WA method for localization directly yields an accurate assessment of the crack length, while a crack depth assessment method can be derived as a continuation of the WA method for damage localization. The robustness of the damage assessment approach has been tested by employing it to the noise-contaminated mode shapes in Appendix D. It is found that while an accurate assessment of the crack length is obtained as long as the general WA method succeeds to locate the crack, the crack depth method is slightly more sensitive towards noise than the method for localization. However, the sensitivity is found acceptable, thus the method can, along with the chosen level 1 and 2 damage identification methods, be applied in the analyses of the Whisper 500 blade and the GE 1.5 XLE blade.

# EXPERIMENTAL SETUP FOR WHISPER 500 BLADE

In the experimental modal analysis of the Whisper 500 blade, the approach is to derive frequency response functions such that the modal parameters, namely eigenfrequencies and mode shapes, can be extracted. The frequency response functions are derived from measured hammer hit excitations and resulting acceleration responses. The experimental setup is visualized in Fig. 3.1a, and in Fig. 3.1b the model generated in the modal analysis software package Brüel and Kjær (B&K) PULSE LabShop and PULSE Reflex [42] is illustrated. In the model, numbering of excitation and measurement points is given. This numbering will be used, when relevant, in all the coming descriptions and analyses of the Whisper 500 blade.



(a)



(b)

**Fig. 3.1:** Experimental setup for Whisper 500 blade. (a) Blade with mounted accelerometers. (b) Model in B&K software in which the red arrows show the placement and measurement direction of accelerometers and the black hammer animations show the excitation points. Notice that accelerometers are also placed in the excitation points.

In the present chapter, details of the experimental setup are presented and described. The fixation of the blade is described in Section 3.1, the hammer excitation and the acceleration monitoring are treated in Section 3.2 and 3.3, respectively, while specific features of the data analyzer software are presented in Section 3.4. Lastly, the descriptions in the aforementioned sections are summarized in Section 3.5.

## 3.1 Fixation system

In order to obtain a simple, definable geometric boundary condition, the Whisper 500 blade is analyzed in a constrained-free configuration as shown in Fig. 3.2a. The blade root is constrained

by use of a welded steel construction, and additionally a hydraulic pump is employed for further stiffening.

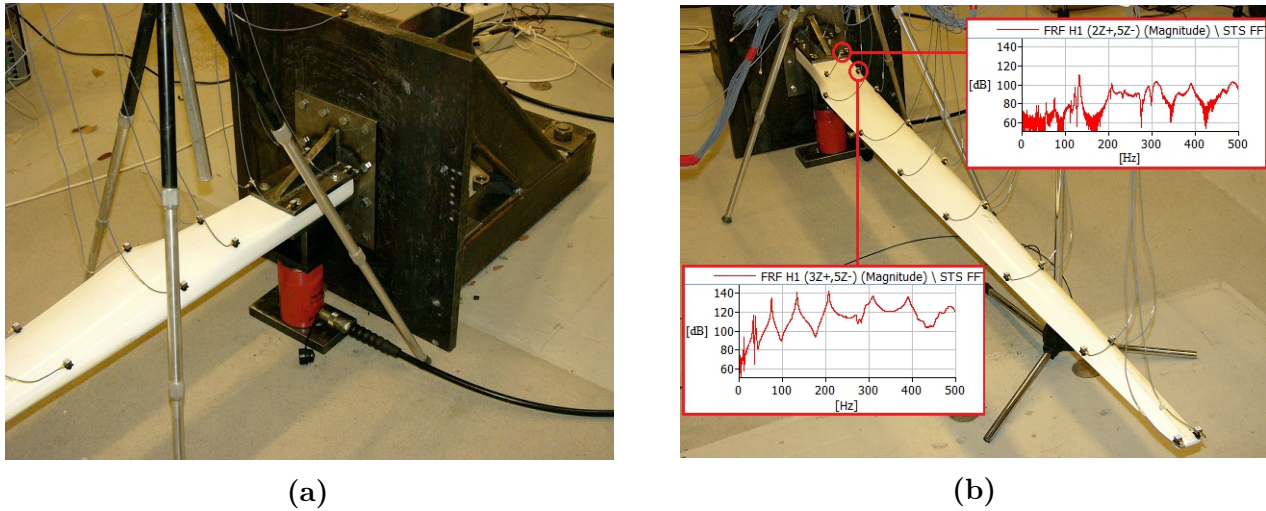


**Fig. 3.2:** Experimental setup for Whisper 500 blade. (a) Fixation consisting of welded steel construction and hydraulic pump. (b) Frequency response functions for accelerometer 2 and accelerometer 3.

To verify that no significant vertical movement is present at the fixation, four accelerometers are mounted on the fixation as control measures. The frequency response functions for accelerometer 2 and 3, with excitation in point 5, are presented in Fig. 3.2b. It is seen that the response measured in accelerometer 2 fails to yield distinguished frequency peaks, whereas the response measured in accelerometer 3 clearly identify eigenfrequencies. Therefore, it is concluded that no significant vertical movement occurs in the fixation. This conclusion is verified by the finite element boundary condition modeling in Section 4.3. It is remarked that by using the chosen boundary condition, the in-service effects of a turbine tower are not represented.

## 3.2 Impact hammer

As mentioned introductory in the present chapter, the experiments of the Whisper 500 blade are conducted with a hammer, namely the B&K 8202 hammer depicted in Fig. 3.3. A hammer hit compose an impulse load, as described in Appendix C where the theoretical background for this type of excitation is treated.



**Fig. 3.3:** B&K 8202 hammer used in the modal experiments.

The excitation of the blade, and thus the input for the frequency response function, is achieved by monitored hammer hits in downwards ( $-z$ -)direction, see Fig. 3.1b. To ensure proper excitation of the frequency range of interest, the input signal from the hammer impact is monitored in both frequency and time domain using a built-in double hit detector implemented in the measurement acquisition software. The experimental procedure consists of an excitation sequence of ten hammer hits in point 5, 7 and 9, respectively. The excitation points are visualized by animated hammers in Fig. 3.1b.

### 3.3 Accelerometers

The model in Fig. 3.1b shows how twenty accelerometers are mounted. The accelerometers are uniaxial B&K 4507 B integrated electronic piezoelectric (IEPE) transducers, see Fig. 3.4. It is chosen to mount 16 on the blade, evenly distributed along the trailing edge and leading edge, in order to catch all the desired modes properly. Furthermore, as described in the previous section, four accelerometers are mounted on the fixation to monitor the movements of this boundary.

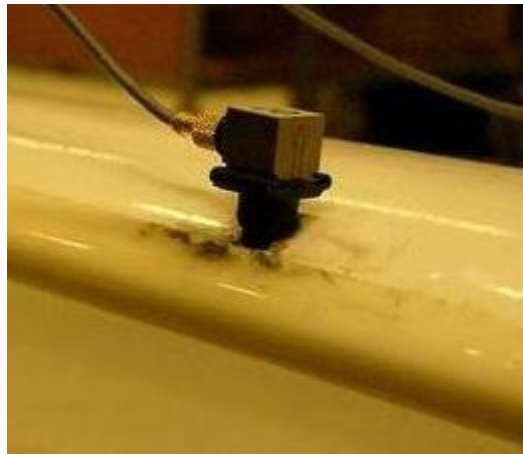


**Fig. 3.4:** Uniaxial B&K 4507 B IEPE accelerometer mounted on Whisper 500 blade by use of a B&K swivel base.

Since the accelerometers are placed close to the blade edges, the curvature in the area of the mounting points is large. Consequently, the accelerometers are mounted on B&K swivel bases to ensure alignment, thus facilitating vertical acceleration measurements. In Fig. 3.4, a picture of an accelerometer mounted on a swivel base is presented.

### 3.4 Data analyzer

The data analyzer package consists of B&K data acquisition hardware plus analyzing software in the form of B&K PULSE LabShop and B&K PULSE Reflex. LabShop is the fundamental data acquisition and analysis software while Reflex is the post-processing software in which the modal analysis is conducted.

### 3.4.1 Initial data analysis

The LabShop software facilitates real-time, multi-channel fast Fourier transformation spectrum analysis. In the experimental tests of the Whisper 500 blade, spectrum analyses were conducted with a frequency span of  $f \in [0 \text{ Hz}; 500 \text{ Hz}]$  and 6400 frequency lines, thus resulting in a frequency increment of  $\Delta f = 0.078125 \text{ Hz}$ .

The LabShop software has several additional features. One of these is the double hit detector mentioned in Section 3.2. Another feature is employment of windowing functions to reduce spectral leakage, which occurs inherently when a signal is made finite by cutoffs. The cutoffs cause erroneous frequencies to appear because the Fourier transform of the finite-length signal assumes that the signal is periodic within the sample record length. No use of windows corresponds to applying a rectangular window, which clearly illustrates the meaning of spectral leakage since the Fourier transform of an unscaled rectangular temporal function is the sinc function shown in Fig. 3.5. Evidently, the sinc function contains sidelobes which are classified as spectral leakage.

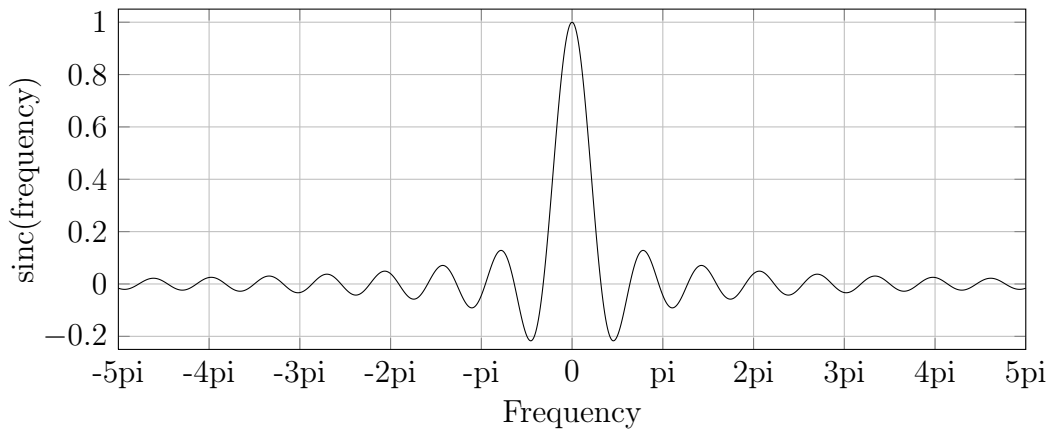


**Fig. 3.5:** sinc frequency function derived by Fourier transform of unscaled rectangular temporal function.

The windows shown in Fig. 3.6 are applied to reduce the spectral leakage. In Fig. 3.6a, it is illustrated how a so-called transient window is applied to the hammer input signal, while the exponential window shown in Fig. 3.6b is applied to the acceleration output. Besides spectral leakage, inherent noise is present in the signals. To reduce these noise contaminations, each windowed signal is divided into overlapping segments, and then a power spectral density is computed for each segment by use of the expression in (2.12). Subsequently, the power spectral densities are averaged, resulting in Welch's power spectral density estimate. Welch's method is implemented in the MATLAB file `spectral_analysis.m` which is a part of the signal analysis MATLAB pseudocode presented in Appendix B. For a comprehensive description of the Welch's method, see e.g. [34].

In Fig. 3.7, the typical effects of applying an exponential window and Welch's method is illustrated for a noise-contaminated sinusoidal signal with two governing frequencies,  $f_1 = 40 \text{ Hz}$  and  $f_2 = 50 \text{ Hz}$ . Evidently, the leakage and noise is reduced significantly, but it is also seen that the resolution, i.e. the ability to discriminate spectral features, is reduced gradually as the window and Welch's method are implemented. Therefore, when performing spectral analysis, it is necessary to make a compromise between estimate reliability and frequency resolution. In



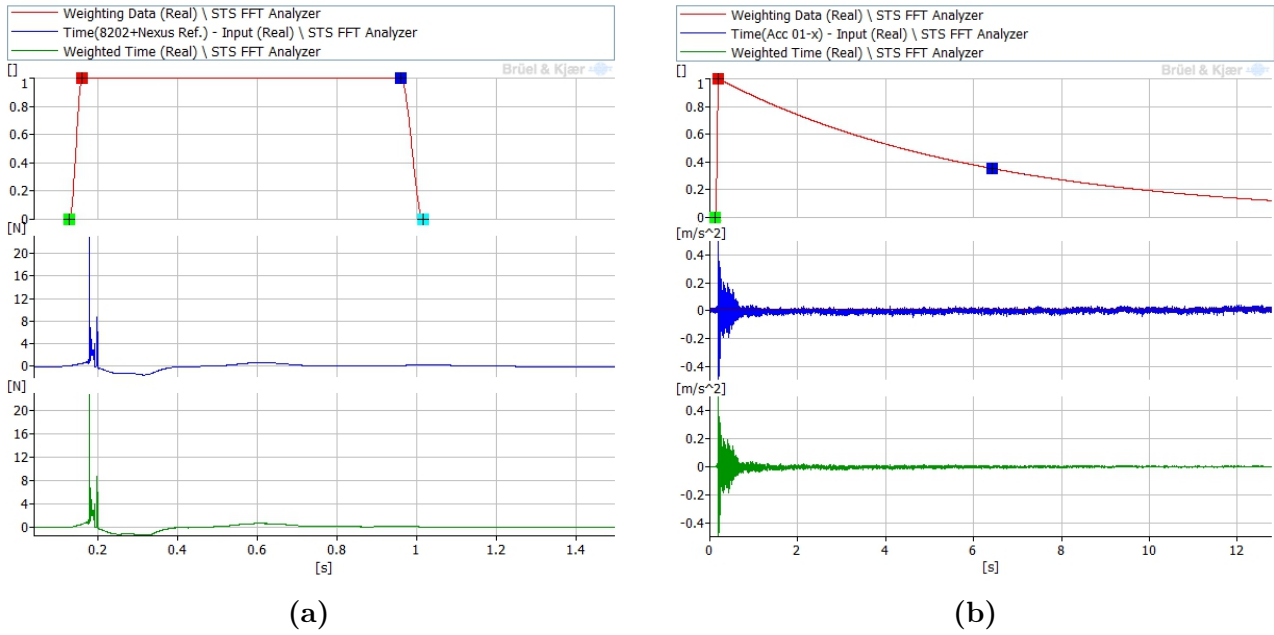


**Fig. 3.6:** Signal windowing in B&K PULSE LabShop. (a) Transient windowing of a hammer input signal. (b) Exponential windowing of an acceleration output signal.

the experimental tests of the Whisper 500 blade, it is, based on an iterative study, chosen to employ the windows illustrated in Fig. 3.6 and the Welch's method with ten segments and 50 % overlapping.

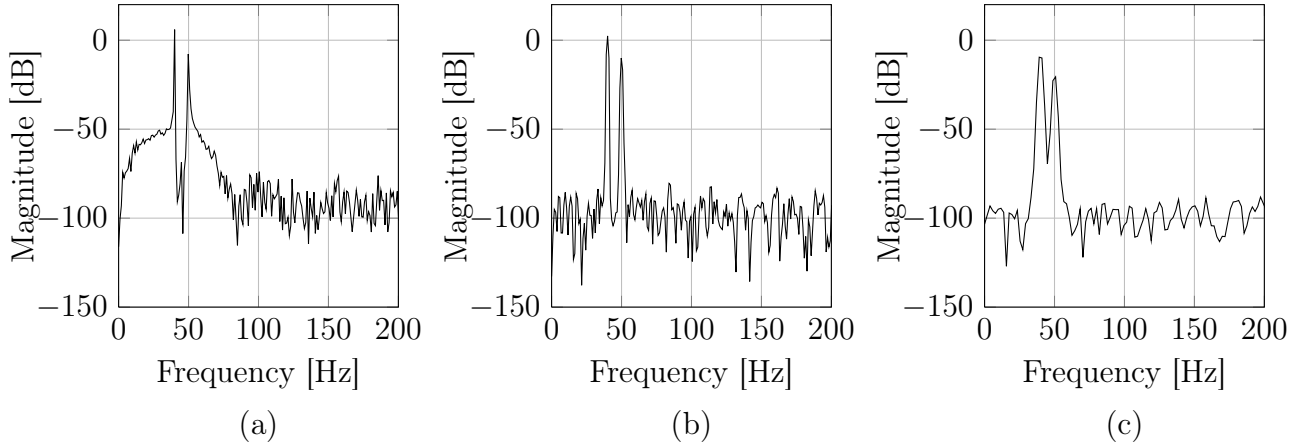


**Fig. 3.7:** Power spectral density of noise-contaminated sinusoidal signal. (a) Without implementation of window or Welch's method. (b) With implementation of window. (c) With implementation of window and Welch's method with three segments overlapping 50 %.

According to Subsection 2.1.2, a way to examine the noise in a signal is by studying the coherence functions, which, as described in the aforementioned subsection, state the measurement consistency and thus provide an indication of the amount of noise contamination. For the Whisper 500 blade, the coherence function derived by excitation in point 5 and acceleration response in point 7 is presented in Fig. 3.8. Since a coherence value of one implies full consistency between the input signal and output signal, the measurement is generally not severely

contaminated by noise. However, local coherence reductions occur at the anti-resonances, presumably due to typical signal analysis contamination factors, e.g. noise and leakage. At the anti-resonances, the output signal is low and thus vulnerable to noise, and therefore it is chosen to derive each frequency response function through (2.13b) since this is less vulnerable to noise in the output signal than that obtained by (2.13c).

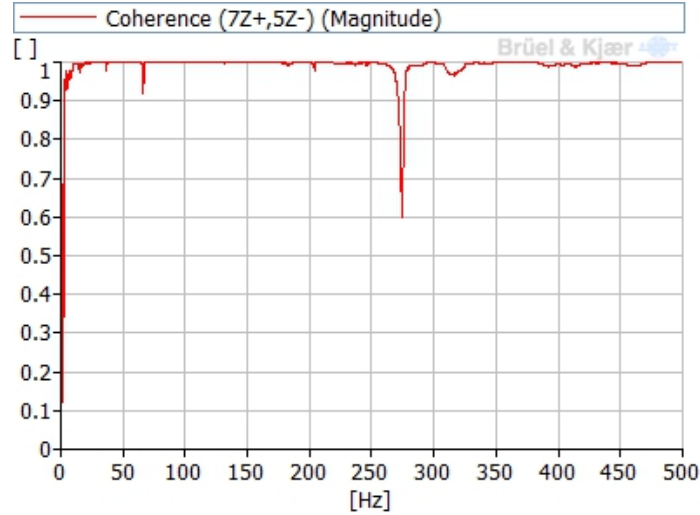


**Fig. 3.8:** Coherence function for excitation in point 5 and acceleration response in point 7, extracted from B&K PULSE LabShop software.

### 3.4.2 Synthesizing considerations

When the frequency response functions have been derived in the LabShop software, they are exported to the Reflex software. Here, the frequency response functions are used to fit synthetic frequency response functions by use of the Rational Polynomial Fraction-Z method, see e.g.

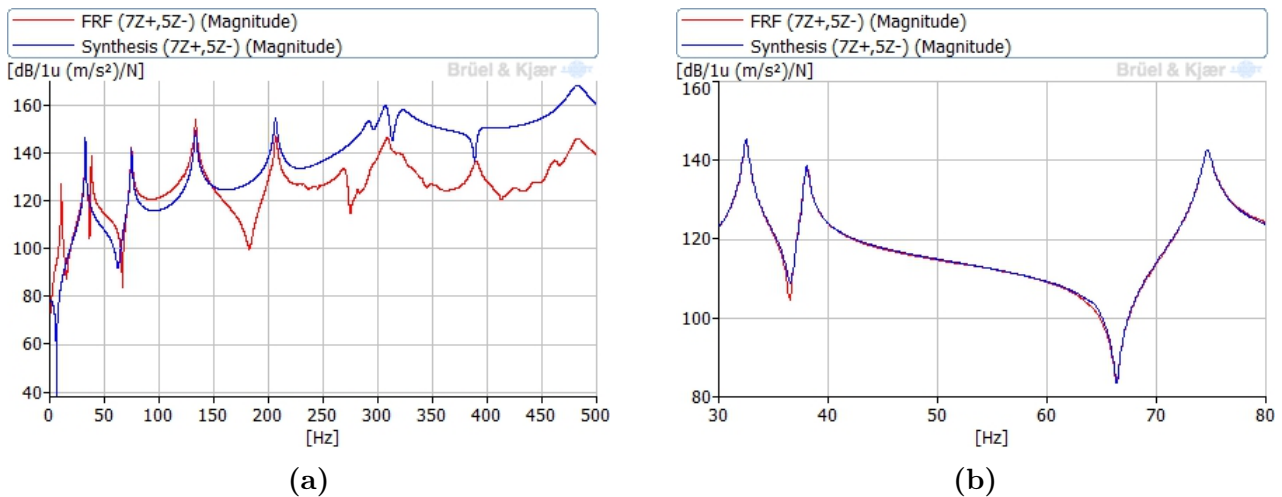


**Fig. 3.9:** Frequency response function and synthesized counterpart for excitation in point 5 and acceleration response in point 7, extracted from B&K PULSE Reflex software. (a) Polynomial fit with  $f \in [0 \text{ Hz}; 500 \text{ Hz}]$ . (b) Polynomial fit with  $f \in [30 \text{ Hz}; 80 \text{ Hz}]$ .



Subsection 2.1.2. In Fig. 3.9, the frequency response function and synthesized counterpart for excitation in point 5 and acceleration response in point 7 are illustrated. The importance of the applied frequency span is emphasized since a polynomial fit over the entire frequency span, i.e.  $f \in [0 \text{ Hz}; 500 \text{ Hz}]$ , yields a poor synthetic regression of the real frequency response function. When the frequency span is reduced, to e.g.  $\Delta f = 50 \text{ Hz}$ , the synthetic frequency response function becomes a good approximation of the real function, and therefore a span of 50 Hz is used in the experimental tests of the Whisper 500 blade. The specific span presented in Fig. 3.9b is chosen solely for illustrative purposes; it contains several modes, of which two are closely spaced. In the actual tests, spans of  $f_1 \in [1 \text{ Hz}; 50 \text{ Hz}]$ ,  $f_2 \in [51 \text{ Hz}; 100 \text{ Hz}]$ , ...,  $f_{10} \in [451 \text{ Hz}; 500 \text{ Hz}]$  are utilized.

As described in Subsection 2.1.2, the modal parameters can be directly extracted from a synthetic frequency response function. This is done for a combined synthetic frequency response function which is an average of all synthetic functions. In order to locate the eigenmodes, the complex mode indicator function (CMIF) and a stabilization diagram are utilized. The principle of a stabilization diagram is described in Subsection 2.1.2 and in Fig. 3.10, a stabilization diagram obtained in the experimental tests of the Whisper 500 blade is visualized. The CMIF is defined as the eigenvalues, which are the square of the singular values obtained by singular value decomposition, solved from the normal matrix formed from the frequency response function matrix, i.e.  $H(j\omega)^H H(j\omega)$  where  $H(j\omega)^H$  is the Hermitian transpose of  $H(j\omega)$ . The CMIF is then the plot of these eigenvalues on a log magnitude scale as a function of frequency, and since the number of singular values equals the number of references in the frequency response function dataset, the CMIF enables identification of repeated roots, i.e. multiple modes at same frequency, plus closely coupled modes. For further information about the CMIF, see e.g. [43].

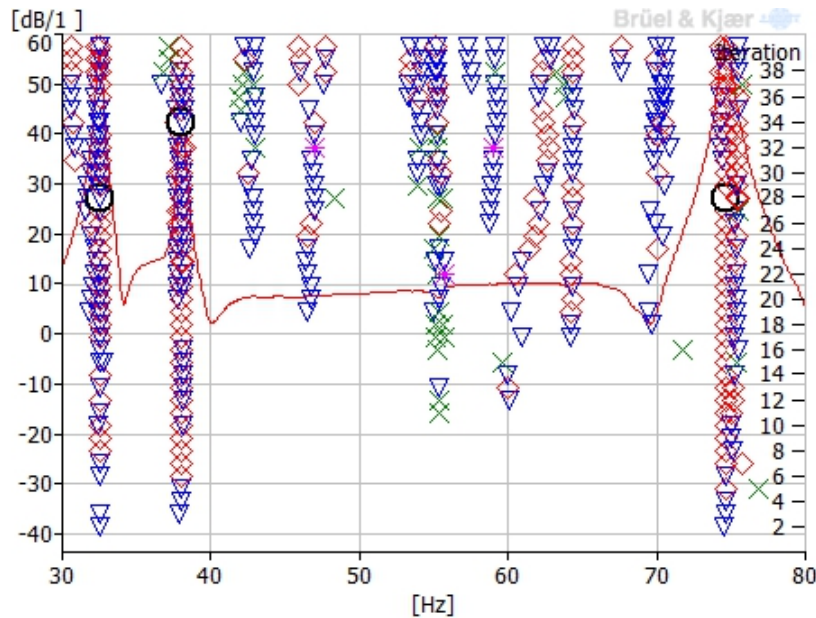


**Fig. 3.10:** Stabilization diagram for  $f \in [30 \text{ Hz}; 80 \text{ Hz}]$ , extracted from B&K PULSE LabShop software. The circles mark the chosen poles.

Fig. 3.10 shows how the physical poles are stabilized during the iterations, as described in Subsection 2.1.2, hence the eigenmodes can easily be localized and picked. The mode picking

can be performed both manually and automatically in the PULSE Reflex software. In the experimental tests of the Whisper 500 blade, the automatic method yields accurate results when the frequency span for each polynomial fit is  $\Delta f = 50$  Hz.

### 3.5 Summary

In the preceding sections in this chapter, the essential details regarding the experimental tests of the Whisper 500 wind blade are presented and described. Firstly, the used fixation system is treated in Section 3.1, where it is described how the system consists of a steel construction and a supplementary hydraulic pump. The fixation system serves to provide a boundary condition which restrains against movement at the blade root. Based on frequency response functions obtained from accelerometers mounted on the fixation system, it is concluded that no significant vertical movement occurs in the fixation. This finding is further tested in Section 4.3 where finite element modeling of the boundary condition is conducted.

The experiments are carried out with hammer hits as excitation and measured accelerations as response. The hammer and accelerometers in question are presented in Section 3.2 and Section 3.3, respectively. The hammer is a B&K 8202 hammer which provides a signal of the impulse load generated by each hammer hit. The accelerometers are uniaxial B&K IEPE transducers and because these are mounted close to the blade edges, where the curvature is generally large, the accelerometers are mounted on B&K swivel bases to ensure alignment such vertical measurements are obtained. A total of 16 accelerometers are mounted on the blade, distributed along both the trailing and leading edge to capture the desired modes properly.

The excitation procedure is composed by a sequence of ten hammer hits near accelerometer 5, ten hammer hits near accelerometer 7 and ten hammer hits near accelerometer 9, thus resulting in 480 frequency response functions for the 16 accelerometers mounted on the blade. The frequency response functions are derived in the B&K PULSE LabShop software and subsequently exported to the B&K PULSE Reflex software, where a combined synthetic frequency response function, i.e. the average of all synthetic functions, is derived by piecewise regressions of the real frequency response functions and subsequent averaging. From this combined synthetic frequency response function, the modal parameters can be directly extracted by use of CMIF and a stabilization diagram. The results, in the form of eigenfrequencies and mode shapes, are presented in Subsection 5.1.1.

---

# FINITE ELEMENT MODEL OF WHISPER 500 BLADE

---

In the present chapter, a finite element model of the Whisper 500 blade is developed in the commercial finite element program ANSYS Workbench. In Section 4.1, the geometric representation of the Whisper 500 blade with and without cracks is described, and next the material modeling of the blade is conducted in Section 4.2 where different material models will be presented. In Section 4.3, it is, on the basis of a simple steel beam, examined how the fixation system shown in Section 3.1 can be represented by simple geometrical boundary conditions. Then, in Section 4.4, the damping of the Whisper 500 blade is treated and it is shown how the structural damping can be omitted since the blade is very lightly damped. In Section 4.5, the blade is discretized and reduced by use of substructuring, and finally the model is calibrated against experimental test findings in Section 4.6. This is necessary since no material data are known for the blade. In Section 4.7, the development process of the finite element model is summarized.

As stated introductory in Chapter 2, all analyses, including the finite element analyses of the Whisper 500 blade, are performed on the assumptions that the systems are linear and time-invariant.

## 4.1 Geometry

The geometry of the blade, shown in Fig. 4.1, is modeled directly in ANSYS Workbench. The modeling is conducted in accordance with the cross-sectional measurements performed on a 2.2 m long Whisper 500 blade in [44]. Here, eight distinct cross-sections along the blade were measured, thus the model is divided into seven sections. The model consists of two components;

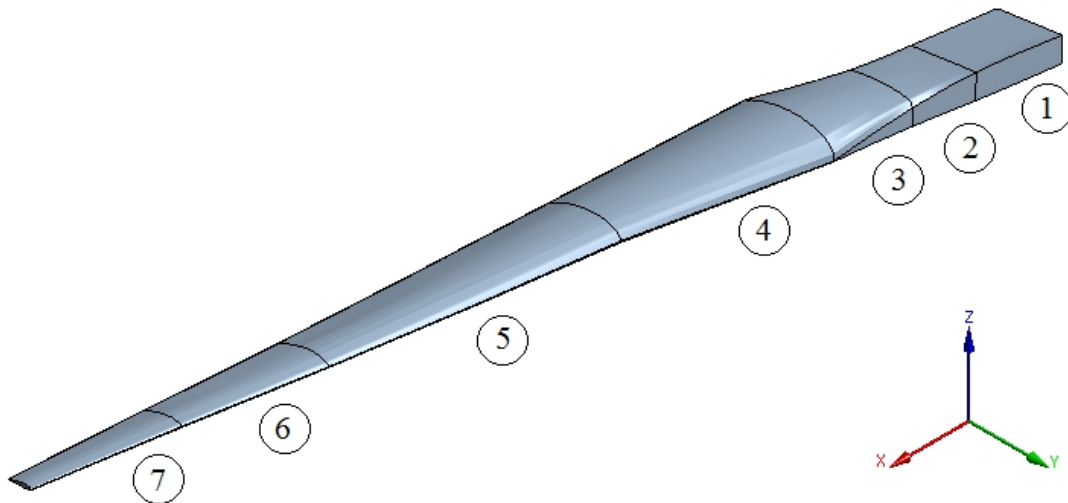


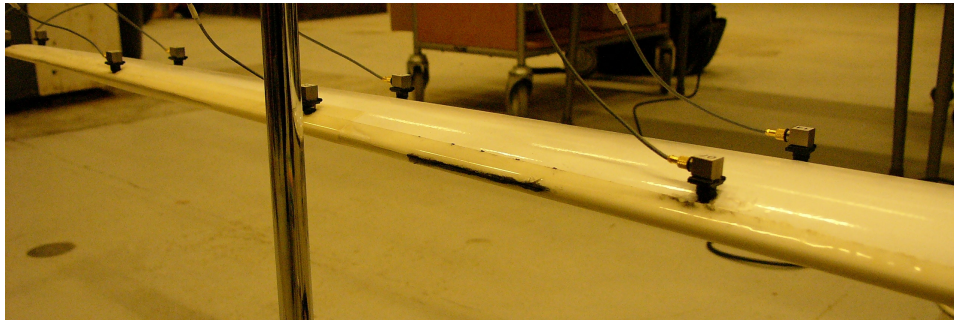
**Fig. 4.1:** Model of Whisper 500 blade with section numbering and global coordinate system.

an outer shell and an inner foam core in sections 1 and 2, i.e. the blade is hollow in sections 3 to 7. In Section 4.2, the materials of the two components are described.

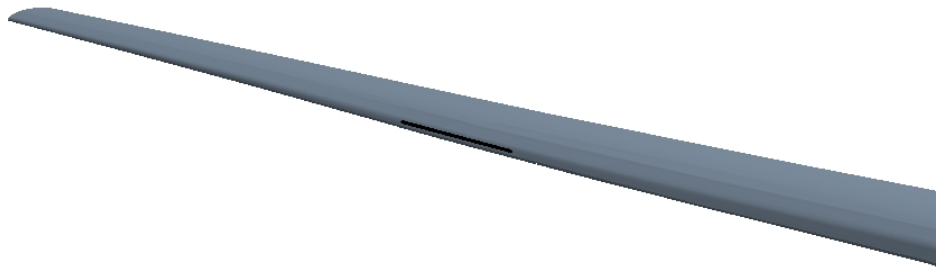
The coordinate system presented in Fig. 4.1 is global with origin in the leftmost top corner of the start of section 1. The coordinate system will be used consistently in the finite element analyses of the Whisper 500 blade.

### 4.1.1 Crack modeling

According to [45], the leading edge in the assembly between the top and bottom blade shell is a stressed area where the material can easily be damaged. Consequently, it is chosen to introduce the crack edgewise in the assembly;  $2/3$  of the blade length from the root which is a specifically critical area [45]. In order to examine the sensitivity towards the crack size, three different sizes, namely 50 mm, 100 mm and 200 mm, are introduced. These are chosen on the basis of cracks found in several 100 kW wind turbine blades [9] which are then scaled proportionally to the Whisper 500 blade. Hereby, a realistic damage situation is simulated. In Fig. 4.2a, the blade with a 100 mm crack is depicted, and in Fig. 4.2b the corresponding finite element model is illustrated.



(a)



(b)

**Fig. 4.2:** Crack-introduced Whisper 500 blade. (a) A picture of the real blade with a crack. (b) Finite element model with crack.

In the modeling of the blade cracks, two approaches have been examined. In the first approach, the crack is introduced by simply removing a small amount of material in the model, see Fig. 4.3a. In the second approach, the crack is modeled by cutting in the blade model without removing any material, thus resulting in inconsistencies along the crack, as shown in Fig. 4.3b. For the small cracks introduced in the actual blade, it is found that the approaches

approximately yield the same results, i.e. the amount of material removed in the first approach has insignificant mass. However, when a significant amount of material is removed, the two approaches will, of course, deviate. Since the actual cracks are introduced by use of a utility knife, it is assessed that the first approach, i.e. removal of material, is the most representative, and therefore this approach is utilized.

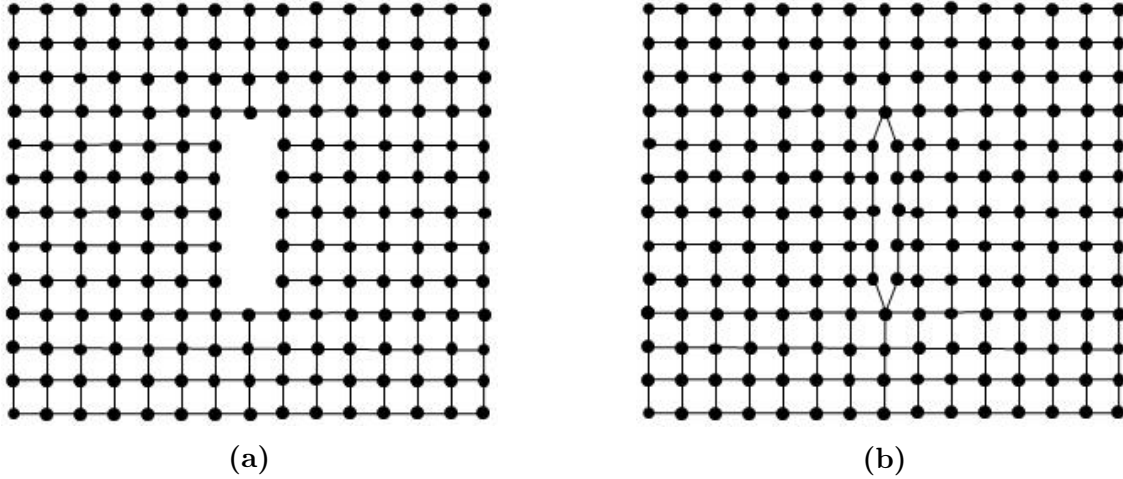


**Fig. 4.3:** Illustrative description of two crack modeling methods on a plane element mesh. (a) A mesh with crack simulated by removing nodes. (b) A mesh with crack simulation by addition of nodes.

## 4.2 Materials

As described in Section 1.3, the Whisper 500 blade consists of two structural components; an inner PVC foam core and an outer glass- and carbon-reinforced composite shell. Since no destructive material tests have been possible, the material data for the two components must be determined by use of calibration. This is done in Section 4.6 where the calibration is performed on the basis of the initial parameter values and appertaining ranges given in the present section, see Table 4.1.

Initially, the material behavior of the structural components were defined by an isotropic material model which is documented in DAMAS paper 2<sup>1</sup>. The studies in this paper showed how the finite element model lacks the ability to validly represent twisting modes when an isotropic material model is utilized, i.e. when the general stiffness expression (2.2) has the constitutive matrix

$$D = \frac{E}{2(1+\nu)(1-2\nu)} \begin{bmatrix} 2(1-\nu) & 2\nu & 2\nu & 0 & 0 & 0 \\ 2\nu & 2(1-\nu) & 2\nu & 0 & 0 & 0 \\ 2\nu & 2\nu & 2(1-\nu) & 0 & 0 & 0 \\ 0 & 0 & 0 & 1-2\nu & 0 & 0 \\ 0 & 0 & 0 & 0 & 1-2\nu & 0 \\ 0 & 0 & 0 & 0 & 0 & 1-2\nu \end{bmatrix}. \quad (4.1)$$

<sup>1</sup>DAMAS paper 2 can be found on the enclosed DVD.

Evidently, the isotropic material model assumes that each material has the same quantities in all directions, resulting in three unknown material parameters in the form of the density,  $\rho$ , Young's modulus,  $E$ , and Poisson's ratio,  $\nu$ . However, since the blade shell is made of various layers of fibrous composite materials, it is plausible that the shell material is indeed not isotropic. Hence, to represent the material behavior validly, and thereby improving the general finite element model of the blade, an orthotropic material model is employed for the shell. Hereby, the constitutive matrix

$$D = \begin{bmatrix} E_x\eta(1 - \nu_{yz}\nu_{zy}) & E_x\eta(\nu_{yx} + \nu_{zx}\nu_{yz}) & E_x\eta(\nu_{zx} + \nu_{yx}\nu_{zy}) & 0 & 0 & 0 \\ E_y\eta(\nu_{xy} + \nu_{xz}\nu_{zy}) & E_y\eta(1 - \nu_{zx}\nu_{xz}) & E_y\eta(\nu_{zy} + \nu_{zx}\nu_{xy}) & 0 & 0 & 0 \\ E_z\eta(\nu_{xz} + \nu_{xy}\nu_{yz}) & E_z\eta(\nu_{yz} + \nu_{xz}\nu_{yx}) & E_z\eta(1 - \nu_{xy}\nu_{yx}) & 0 & 0 & 0 \\ 0 & 0 & 0 & G_{xy} & 0 & 0 \\ 0 & 0 & 0 & 0 & G_{yz} & 0 \\ 0 & 0 & 0 & 0 & 0 & G_{xz} \end{bmatrix} \quad (4.2)$$

is used for the shell, with the parameter  $\eta$  being

$$\eta = \frac{1}{1 - \nu_{xy}\nu_{yx} - \nu_{yz}\nu_{zy} - \nu_{zx}\nu_{xz} - \nu_{xy}\nu_{yz}\nu_{zx} - \nu_{yx}\nu_{zy}\nu_{xz}}. \quad (4.3)$$

According to Maxwell's reciprocal theorem,  $D$  must be symmetric, thus (4.2) contains nine unknown elastic parameters, meaning that the amount of unknown material parameters for the shell is increased to the density,  $\rho$ , the directional Young's moduli,  $E_x$ ,  $E_y$  and  $E_z$ , the Poisson's ratios,  $\nu_{xy}$ ,  $\nu_{yz}$  and  $\nu_{xz}$ , and the shear moduli,  $G_{yz}$ ,  $G_{zx}$  and  $G_{xy}$ . The PVC foam core is still assumed isotropic, i.e. the total number of unknowns in the material model of the Whisper 500 blade is 13. The initial values of the material properties, and the appertaining ranges, are presented in Table 4.1. These values and ranges are chosen in accordance with [46,47].

**Table 4.1:** Initial material parameters and ranges for the isotropic core and the orthotropic shell. In the table, the abbreviations Min. (Minimum), Max. (Maximum), Ini. (Initial) and NA (Not available) are used. The unit of the Young's and shear moduli,  $E$  and  $G$ , is GPa and the unit of the densities,  $\rho$ , is kg/m<sup>3</sup>.

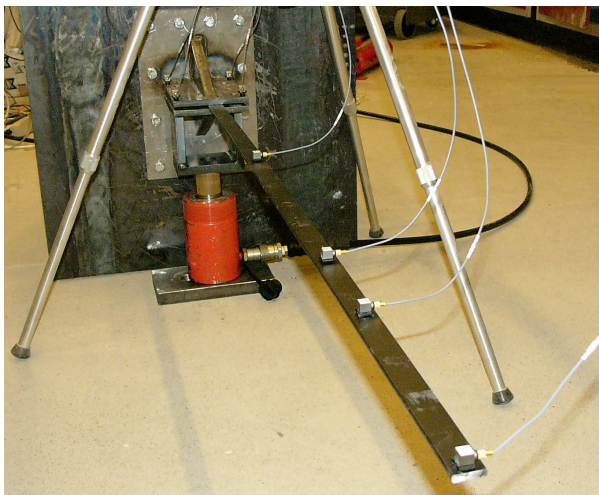
	Core			Shell									
	$E$	$\nu$	$\rho$	$E_x$	$E_y$	$E_z$	$\nu_{xy}$	$\nu_{yz}$	$\nu_{xz}$	$G_{xy}$	$G_{yz}$	$G_{xz}$	$\rho$
Min.	0.032	0.32	40	NA	NA	NA	0.25	0.25	0.25	NA	NA	NA	1,530
Max.	1.26	0.32	1,561	NA	NA	NA	0.32	0.32	0.32	NA	NA	NA	2,210
Ini.	0.2	0.32	70	18	18	18	0.3	0.3	0.3	6.92	6.92	6.92	1,800

In Appendix A, a tutorial on orthotropic material modeling in ANSYS Workbench is presented. The tutorial stresses out the importance of knowing the default orientation of each element when assigning a directional parameter. For shell elements, a local element coordinate system is default, while solid elements utilize the global coordinate system [48]. This is seen in Fig. 4.5 where the elements used for discretization of the Whisper 500 blade are illustrated.

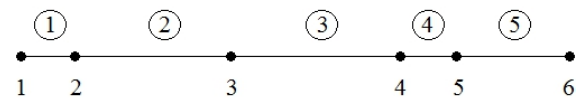


### 4.3 Boundary conditions

Since the finite element analyses of the blade are conducted as free-response simulations, no static boundary conditions are applied. The geometric boundary conditions must be chosen such that a valid representation of the fixation system shown in Fig. 3.2a is obtained. An intuitive way to do this is to model the fixation system and implement it in the analyses. However, the fixation system contains bolts, thus the analyses will become non-linear because contact problems will be introduced. Since the chosen modal analysis-based SHM technique is only valid for linear systems, these contact problems are not permitted. A way to omit the non-linearities is to leave out the bolts and only model the plates. Due to the stiffness of the plates compared to the blade, it is suggested that this approach can be simulated by simply constraining against translational movement in the area of the blade held by the fixation system. An even simpler approach is to clamp the blade at the end of the fixation system. The two suggested approaches are tested by use of an experimental modal analysis of a steel beam constraint by use of the fixation system, see Fig. 4.4a. Analogous finite element analyses are also conducted to find out which geometric boundary condition yields the best agreement with the experimental findings.



(a)



(b)

**Fig. 4.4:** Steel beam used for geometric boundary condition study. (a) Beam mounted with 4 accelerometers and constraint in the fixation system. (b) 2-dimensional beam element model with node and element numbering (the fixation system spans element 1).

The cantilevered beam is constructed in structural steel, namely S235. Young's modulus is found empirically through a series of static deflection tests, while the other relevant material parameters are set to standard values. On the basis of these material parameters, two different boundary conditions are applied, alternately, to the beam element model shown in Fig. 4.4b. It is noted that the length of element 1 is identical to the length of the fixation system.

First, an analysis is conducted with a fixed boundary condition (all d.o.f. restrained) applied at node 2, i.e. node 1 and element 1 are omitted, and then an analysis in which element 1 is restrained against translational displacements is conducted. The first configuration is referred to as configuration 1, while the other is configuration 2. The results of the two analyses and the corresponding experimental findings are presented in Table 4.2.

**Table 4.2:** Eigenfrequencies of steel beam found via experiments and finite element analyses. In the table, the abbreviations EF (Eigenfrequency), no. (number), Exp. (Experimental), config. (configuration) and FEA (Finite element analysis) are used.

EF no.	Exp. findings [Hz]	FEA results of config. 1 [Hz]	FEA results of config. 2 [Hz]
1	3.47	3.55	3.48
2	21.34	22.23	21.41
3	59.47	62.22	59.93

Evidently, the configuration with element 1 restrained yields acceptable results compared to the experimental findings. Consequently, it is chosen to use a modified version of this boundary condition in the finite element analyses of the blade model. The modification consists of a change from line constraint to surface constraints applied on the top and bottom of section 1, see e.g. Fig. 4.1. As mentioned in Section 3.3, accelerometers are mounted on the fixation system to control whether significant vertical movement is present. In Section 3.1, it is verified that no significant vertical movement occurs in the fixation system when conducting experiments with the blade, hence the chosen geometric boundary condition is a valid representation of the real conditions.

## 4.4 Damping properties

The general free-response finite element modal analysis is conducted on the basis of the homogeneous part of (2.1), which, as shown in Appendix G, can be rewritten to implicitly express complex-valued eigenvalues and eigenfrequencies. However, in the present section, it will be shown that the Whisper 500 blade is so lightly damped in the frequency interval of interest that the damping can be omitted, hence the modal parameters can be calculated by use of (2.7).

The damping exhibited in (2.1) is viscous damping. On the basis of this damping type, it is proven in Appendix G that, just as for the undamped modes (see e.g. Subsection 2.1.1), a fully-ranked set of orthogonal eigenvectors can be derived. Consequently, (2.1) can be decoupled to a set of modal s.d.o.f. equations, i.e.

$$m_l \ddot{q}_l + c_l \dot{q}_l + k_l q_l = r_l \Rightarrow \ddot{q}_l + 2\xi_l \omega_{n,l} \dot{q}_l + \omega_{n,l}^2 q_l = \frac{r_l}{m_l} \quad \because \quad \xi_l = \frac{c_l}{2m_l \omega_{n,l}}, \quad (4.4)$$

with  $q_l = q_l(t)$  being the time-dependent modal displacement of the  $l$ th mode and  $\xi_l$  the modal damping ratio of the  $l$ th mode. This ratio dictates how much each damped eigenfrequency,  $\omega_{d,l}$ , differs from the undamped counterpart,  $\omega_{n,l}$ , because

$$\ddot{q}_l + 2\xi_l \omega_{n,l} \dot{q}_l + \omega_{n,l}^2 q_l = 0 \Rightarrow \lambda_l, \lambda_l^* = -\xi_l \omega_{n,l} \pm \omega_{n,l} j \sqrt{1 - \xi_l^2}, \quad (4.5)$$

where  $\lambda_l$  and  $\lambda_l^*$  are the complex conjugated roots of the characteristic equation, correctly assuming that the motion is underdamped, and  $\omega_{n,l} \sqrt{1 - \xi_l^2}$  is the damped eigenfrequency, denoted  $\omega_{d,l}$ . Thus, the differences between the damped eigenfrequencies and the undamped counterparts can be found directly from the damping ratios. These ratios are derived in the



modal analysis software when an experimental test is performed, and it is found that the biggest percentage deviation between the undamped and damped eigenfrequencies occurs in mode 1 where  $\omega_{n,1} = 10.52$  Hz (presented in Subsection 5.1.1) and  $\xi_1 = 1.02$  %, thus  $\omega_{d,1} \approx 10.52$ . It is therefore concluded that damping can be validly omitted in the finite element analyses.

## 4.5 Discretization

In this section, it is described how the blade model shown in Fig. 4.1 is discretized into a finite element model. In Subsection 4.5.1, a brief description of the element types and sizes chosen for discretization of the blade components is provided. The element sizes are chosen on the basis of a convergence study of the model eigenfrequencies. In Subsection 4.5.2, a study regarding use of dynamic substructuring for the blade core is presented to examine whether this blade component can be represented validly by use of a superelement.

### 4.5.1 Element types and sizes

Due to the thin-walled nature of the blade shell, this component is meshed with second order shell elements (SHELL281), see Fig. 4.5a. The SHELL281 element is an 8-node hexahedral element with six d.o.f., i.e. three translational and three rotational, at each node. The blade core is meshed with 20-node brick solid elements (SOLID186), i.e. a second order element. The SOLID186 element, which is illustrated in Fig. 4.5b, has three translational d.o.f. at each node but no rotational d.o.f.

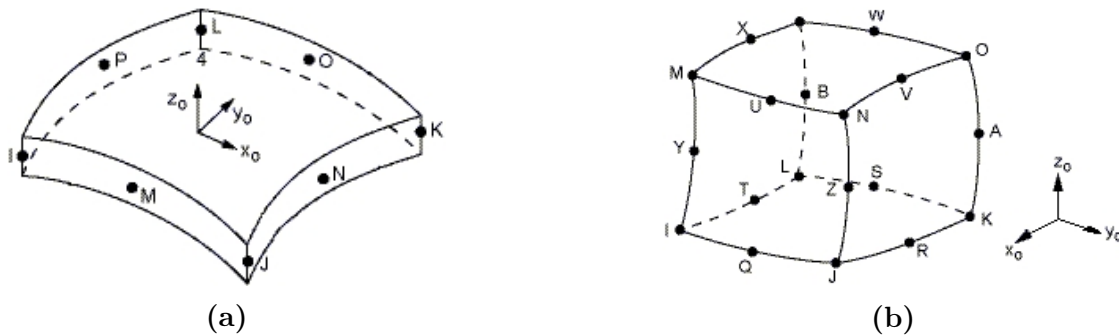


**Fig. 4.5:** Structural elements used in the discretization of the Whisper 500 blade model [48]. (a) SHELL281 element with local coordinate system used for the blade shell. (b) SOLID186 element with local (corresponding to global) coordinate system used for the blade core.

In order to obtain an appropriate mesh, an adaptive convergence study is performed, resulting in the mesh configuration shown in Fig. 4.6. When applying the initial material parameters presented in Table 4.1, the eigenfrequencies tabulated in Fig. 4.6 are obtained. In the converged model, the core is meshed with 10 mm SOLID186 elements, while the shell is globally meshed with 20 mm SHELL281 elements. In the crack-introduced models, a local mesh refinement with 1 mm SHELL281 elements will be employed in the crack area.

Due to the use of solid elements in the blade core discretization, a significantly finer mesh must be used for this component compared to the shell to represent bending and twisting accurately. The converged mesh settings shown in Fig. 4.6 result in 15,345 nodes, of which 9,165 are in the core.

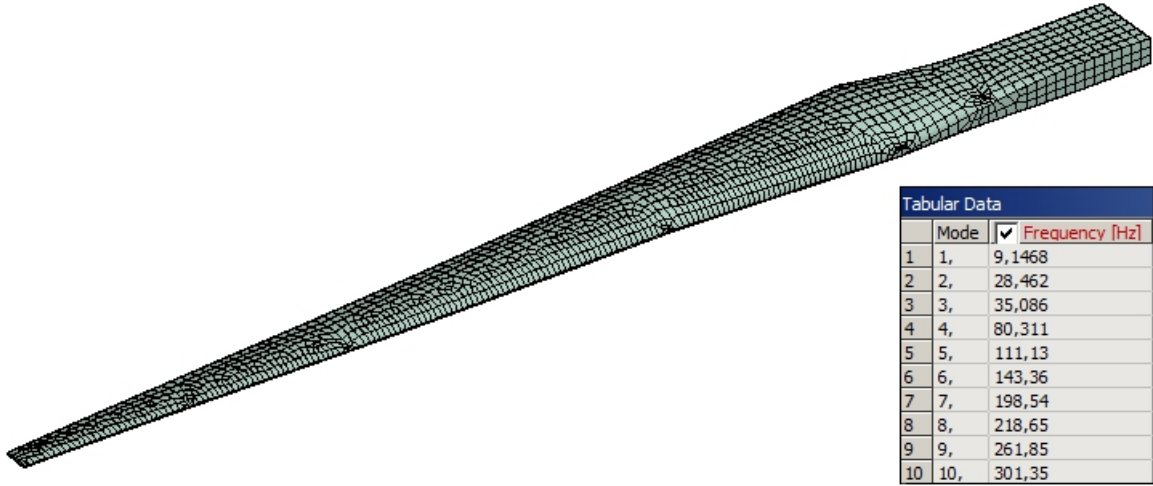


**Fig. 4.6:** Element mesh of the Whisper 500 blade model, with the resulting eigenfrequencies tabulated.

## 4.5.2 Substructuring

To reduce computational time, it is chosen to examine whether the core can be condensed into a superelement by use of substructuring in ANSYS Workbench. In the present subsection, two different substructuring methods, namely Guyan reduction and Craig-Bampton, are briefly described, and subsequently a comparison of the full blade model and reduced models containing the two different superelement types will be conducted. Based on this comparison, the use of superelements will be validated and furthermore it will be shown that the Craig-Bampton method is the best to employ in the substructure of the blade model.

### Guyan reduction method

The main idea of Guyan model reduction is to divide the d.o.f. into masters and slaves, respectively. The slaves are the d.o.f. which are condensed, thus it is crucial to make sure that the choice of slaves do not compromise the initial dynamic character of the full system. I.e., d.o.f. carrying a significant amount of mass and/or d.o.f. that respond significantly when the system is excited should not be chosen as slaves.

By choosing masters and slaves, the dynamic equilibrium equations (2.1) can be partitioned like

$$\begin{bmatrix} M_{11} & M_{12} \\ M_{21} & M_{22} \end{bmatrix} \begin{bmatrix} \ddot{\mathbf{x}}_1 \\ \ddot{\mathbf{x}}_2 \end{bmatrix} + \begin{bmatrix} C_{11} & C_{12} \\ C_{21} & C_{22} \end{bmatrix} \begin{bmatrix} \dot{\mathbf{x}}_1 \\ \dot{\mathbf{x}}_2 \end{bmatrix} + \begin{bmatrix} K_{11} & K_{12} \\ K_{21} & K_{22} \end{bmatrix} \begin{bmatrix} \mathbf{x}_1 \\ \mathbf{x}_2 \end{bmatrix} = \begin{bmatrix} \mathbf{0} \\ \mathbf{0} \end{bmatrix}, \quad (4.6)$$

where  $\mathbf{x}_1$  are the displacements connected to the master d.o.f., while  $\mathbf{x}_2$  are the displacements connected to the slave d.o.f.. Hereby, it is assumed that  $\mathbf{x}_2$  can be considered as static or quasistatic responses, thus

$$K_{21}\mathbf{x}_1 + K_{22}\mathbf{x}_2 = \mathbf{0} \Leftrightarrow \mathbf{x}_2 = -K_{22}^{-1}K_{21}\mathbf{x}_1, \quad (4.7)$$

by which the total displacement vector,  $\mathbf{x} = [\mathbf{x}_1 \ \mathbf{x}_2]^T$ , can be expressed as

$$\mathbf{x} = \begin{bmatrix} I \\ -K_{22}^{-1}K_{21} \end{bmatrix} \mathbf{x}_1. \quad (4.8)$$

Via (4.8), it is evident that the total displacement vector is only expressed by the displacements connected to the master d.o.f. Consequently,  $[I \ -K_{22}^{-1}K_{21}]^T$  must express the base of the dynamic response of the system, hence condensed system matrices are obtained as

$$\psi = \begin{bmatrix} I \\ -K_{22}^{-1}K_{21} \end{bmatrix} \Rightarrow \begin{cases} M_{\text{kon}} = \psi^T M \psi, \\ C_{\text{kon}} = \psi^T C \psi, \\ K_{\text{kon}} = \psi^T K \psi. \end{cases} \quad (4.9)$$

Again, these matrices are formulated by assuming that the slave d.o.f. do not influence significantly on the dynamic character of the initial system. In Fig. 4.7, the first ten eigenfrequencies obtained with the reduced blade model containing a Guyan superelement are compared with the corresponding results obtained with the full model, see Fig. 4.6.

### Craig-Bampton method

In the Craig-Bampton method a structure is divided into substructures, which are connected by the d.o.f. in between, so-called attachment d.o.f. Hereby, the initial structure is reduced to the attachment d.o.f. plus the component modes of each substructure, i.e. the vibration modes of each substructure with fixation of its attachment d.o.f. The component modes, which form internal nodeless d.o.f., can be found through the generalized eigenvalue problem

$$\{K_{nn,j} - \omega^2 M_{nn,j}\} \bar{\mathbf{d}}_{l,j} = \mathbf{0}, \quad (4.10)$$

where  $K_{nn,j}$  and  $M_{nn,j}$  are the system matrices of the  $j$ th substructure with fixation of the attachment d.o.f, while  $\bar{\mathbf{d}}_{l,j}$  is the  $l$ th eigenvector of the  $j$ th substructure. The eigenvectors are gathered in the modal matrix

$$\Phi_j = [\bar{\mathbf{d}}_1 \ \bar{\mathbf{d}}_2 \ \bar{\mathbf{d}}_3 \ \cdots \ \bar{\mathbf{d}}_k]_j, \quad (4.11)$$

with the number of extracted eigenmodes,  $k$ , influencing on both the accuracy of the substructuring and the computational time, i.e. an increased number of extracted eigenmodes increases the accuracy but also the computational time.

In addition to the component modes, the redundant static constraint modes,  $\Psi$ , are also used. These are found as

$$\begin{bmatrix} K_{nn} & K_{na} \\ K_{na}^T & K_{aa} \end{bmatrix}_j \begin{bmatrix} \Psi \\ I \end{bmatrix}_j = \begin{bmatrix} \mathbf{0} \\ \mathbf{q} \end{bmatrix}_j \Leftrightarrow \Psi_j = -K_{nn,j}^{-1} K_{na,j}, \quad (4.12)$$

in which the subscript  $a$  is the attachment d.o.f.,  $I$  is the  $a \times a$ -identity matrix, and  $\mathbf{q}$  is the resulting vector of reactions at the attachment d.o.f. Evidently, the constraint modes compose the static displacement vectors of each substructure produced by applying a unit displacement to each attachment d.o.f., alternately, while keeping the other attachment d.o.f. fixed.

As seen in 4.12, a crucial part of the Craig-Bampton method is based on a partitioned matrix system, just like the Guyan reduction method. Consequently, expressions analogous to the latter in (4.9) are obtained for the reduced substructure matrices, namely

$$\begin{aligned} M_{\text{red,sub},j} &= T_j^T M_{\text{sub},j} T_j, \\ C_{\text{red,sub},j} &= T_j^T C_{\text{sub},j} T_j, \\ K_{\text{red,sub},j} &= T_j^T K_{\text{sub},j} T_j, \end{aligned} \quad (4.13)$$

where  $K_{\text{sub},j}$  is the substructure stiffness matrix formulated in (4.12),  $M_{\text{sub},j}$  and  $C_{\text{sub},j}$  are the corresponding mass and damping matrices, and  $T_j$  is the transformation matrix for the  $j$ th substructure.  $T_j$  is derived implicitly by describing the displacement vector of the internal d.o.f.,  $\mathbf{d}_{n,j}$ , as a hybrid linear combination of the component modes,  $\Phi_j$ , and the constraint modes,  $\Psi_j$ , i.e.

$$\mathbf{d}_{n,j} = \{\Phi \mathbf{a} + \Psi \mathbf{d}_a\}_j \Rightarrow \begin{bmatrix} \mathbf{d}_n \\ \mathbf{d}_a \end{bmatrix}_j = \begin{bmatrix} \Phi & \Psi \\ \mathbf{0} & I \end{bmatrix}_j \begin{bmatrix} \mathbf{a} \\ \mathbf{d}_a \end{bmatrix}_j \quad \therefore T_j = \begin{bmatrix} \Phi & \Psi \\ \mathbf{0} & I \end{bmatrix}_j, \quad (4.14)$$

where  $\mathbf{a}_j$  is a vector containing the modal coordinates, and  $\mathbf{d}_a$  is a vector containing the attachment d.o.f. Evidently, the second column of  $T$  contains the same elements as the Guyan transformation matrix (4.9), thus implying that the Craig-Bampton method is a mixture between static and dynamic condensation.

When the reduced matrices in (4.13) are derived, they can be assembled to yield reduced global system matrices which can be used for, e.g., modal analysis of a structure. In Fig. 4.7, the first ten eigenfrequencies obtained with the reduced blade model containing a Craig-Bampton superelement with 10 component modes are compared with the corresponding results obtained with the full model and a Guyan-reduced model.

### Choice of substructuring method

To validate the use of superelement for the blade core, modal analyses of the full model derived in Section 4.5 and reduced versions of this model are conducted. In Fig. 4.7, the obtained

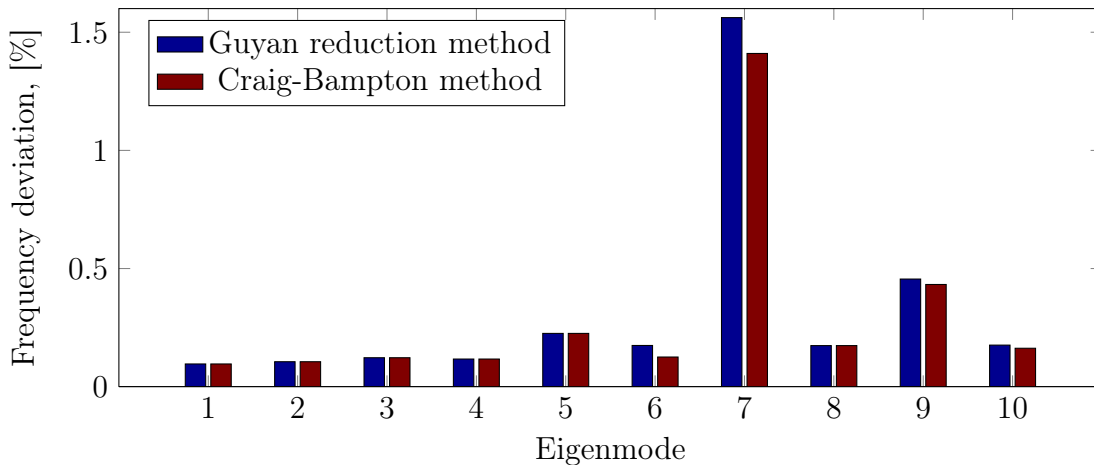


**Fig. 4.7:** Frequency deviations between the Whisper 500 blade model and the reduced models.

deviations between the full model and the reduced ones with Guyan and Craig-Bampton superelements are illustrated. In the modal analyses, the initial material parameters presented in Table 4.1 are used.

As shown in Fig. 4.7, both substructuring methods yield frequencies which are in acceptable agreement with the corresponding eigenfrequencies of the full model. Since this is the case with use of the Guyan reduction method, it can be concluded that the internal blade core d.o.f. do not carry significant amounts of mass. In Appendix H, a simple substructuring analysis which exemplifies inappropriate choice of masters and slaves in the Guyan reduction method is presented. The simple analysis example in Appendix H also serves to present the technicalities regarding employment of substructuring in ANSYS Workbench and to illustrate the general superiority of the Craig-Bampton method.

Since the Craig-Bampton method, cf. Fig. 4.7, yields the most accurate results, it is chosen to condensate the blade core into a superelement by use of this method. Consequently, the number of nodes is reduced from 15,345 to 6,180.

## 4.6 Model calibration

As the last part of the finite element modeling of the Whisper 500 blade, calibration against the experimental findings is conducted. To ensure that the calibration is carried out validly, studies with simpler systems have been made. These studies have resulted in the ANSYS Workbench calibration tutorial in Appendix I.

In DAMAS paper 2, it is documented how a finite element model with isotropic material models is calibrated against the first six experimental modes of the Whisper 500 blade. The calibration is executed as an optimization problem with constraints in the form of an experimentally determined static deflection and the blade mass. In the present section, further calibration is conducted as the isotropic shell material model is converted to a orthotropic model in order to, validly, represent the first ten modes of the Whisper 500 blade, i.e. including the twisting modes. Since the approach to the coming calibration is similar to the one performed in the aforementioned paper, it is chosen not to document the initial calibration in the present report. Hence, the calibration documented here succeeds the initial calibration from the paper where only the bending modes were represented validly. This leads to the idea of tuning only the shear moduli to examine whether change in these are sufficient to include representative twisting modes.

### 4.6.1 Sensitivity study

Before the actual tuning of the shear moduli is conducted via calibration, sensitivity studies of these moduli are performed. The studies are based on the two twisting modes, i.e. modes 7 and 10, whose experimental characteristics are presented in Subsection 5.1.1. Since the tendencies revealed by the studies are identical for the two modes, only the results obtained for mode 7 are presented in this subsection. The plot in Fig. 4.8 illustrates the design points utilized in the calibration study of mode 7 for which the interval  $G_{ij} \in [3 \text{ MPa}; 6.92 \text{ MPa}]$  is employed for all shear moduli.

By interpolating the design points and their appertaining eigenfrequency values presented in Fig. 4.8, the comprehensive data obtained clearly reveal the sensitivity of each shear modulus. This is evident in Fig. 4.9a where the local sensitivities are presented. It is seen how the twisting

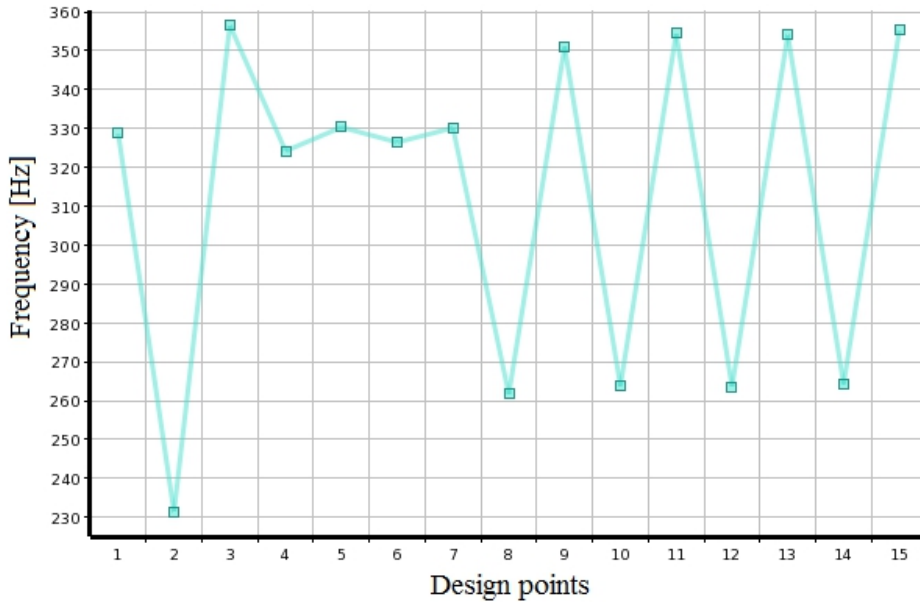
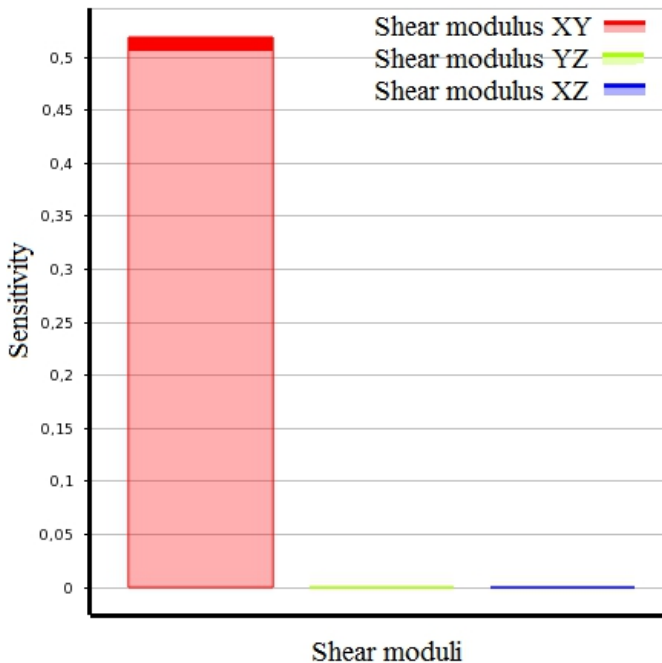
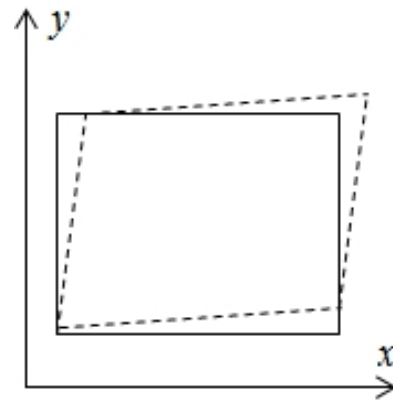


**Fig. 4.8:** Design points in calibration of mode 7 of Whisper 500 blade model. The corresponding experimental finding is 292.47 Hz.

modes are primarily sensitive towards the shear modulus  $G_{xy}$ . When recalling the orientation of the coordinate system for the shell element, see e.g. Fig. 4.5a, it is expectable that only  $G_{xy}$  influences the twisting modes significantly since this modulus governs the in-plane shear deformation of the shell element, see Fig. 4.9b.



(a)



(b)

**Fig. 4.9:** Sensitivity study of shear moduli for Whisper 500 blade. (a) Sensitivity of mode 7 towards shear moduli. (b) In-plane shear deformation.

### 4.6.2 Final calibration

In order to reduce the computational time of the calibration procedure, the shear moduli  $G_{yz}$  and  $G_{xz}$ , which do not affect the twisting modes significantly, are assigned values in agreement with the isotropic relation

$$G = \frac{E}{2(1 + \nu)}. \quad (4.15)$$

Consequently, the calibration procedure only has one variable parameter, namely  $G_{xy}$ , which is tuned so the finite element model of the Whisper 500 blade yields modes in agreement with those obtained in the experimental tests, see e.g. Subsection 5.1.1. In Table 4.3, the final material values obtained through calibration are presented along with initial counterparts. In Section 5.2, the eigenfrequencies and mode shapes of the calibrated finite element model are compared directly to the corresponding experimental findings.

**Table 4.3:** Initial and final material parameters for the finite element model of the Whisper 500 blade. In the table, the abbreviations Ini. (Initial) and Fin. (final) are used. The unit of the Young's and shear moduli,  $E$  and  $G$ , is GPa and the unit of the densities,  $\rho$ , is  $\text{kg}/\text{m}^3$ .

	Core			Shell									
	$E$	$\nu$	$\rho$	$E_x$	$E_y$	$E_z$	$\nu_{xy}$	$\nu_{yz}$	$\nu_{xz}$	$G_{xy}$	$G_{yz}$	$G_{xz}$	$\rho$
Ini.	0.2	0.32	70	18	18	18	0.3	0.3	0.3	6.92	6.92	6.92	1,800
Fin.	0.08	0.32	209	15.3	15.3	15.3	0.3	0.3	0.3	4.16	5.88	5.88	1,520

## 4.7 Summary

In the present chapter, a finite element model of the Whisper 500 blade has been developed. In Section 4.1, the geometry of the blade is modeled in ANSYS Workbench on the basis of cross-sectional measurements conducted in [44]. The model consists of two structural components, namely an isotropic PVC foam core and an orthotropic glass- and carbon-reinforced composite shell, for which no material parameters are known in advance. In Section 4.2, the employed material models are described and here typical values for each material parameter are presented. These values are then later tuned in the calibration procedure executed in Section 4.6. However, before this is done, essential aspects in the form of boundary conditions, damping properties and discretization are treated.

In Section 4.3, the boundary conditions applied to the Whisper 500 blade are presented. Since the finite element analyses of the blade are all free-vibration simulations, no static boundary condition is applied. For geometric boundary condition, it is, based on a simple example with a steel beam, chosen to apply surface constraints on the top and bottom of the blade root such that these are restrained against translational movement.

With regard to the damping properties, it is shown in Section 4.4 that the blade is very lightly damped, hence the damping term is omitted in the finite element formulation.

As a last measure before calibration, the blade model is discretized in Section 4.5 where it is chosen to employ second order shell elements for the composite shell and second order solid

elements for the PVC core. Subsequently, the core is condensed into a superelement such that the total amount of model nodes is reduced significantly. In Section 4.6, this reduced model is calibrated against the analogous experimental findings, thus ensuring that the finite element model of the Whisper 500 blade represents the actual blade validly.

The calibrated finite element model of the Whisper 500 blade is utilized for damage identification analyses in Chapter 5. Here, the modal parameters extracted from the model will also be compared to corresponding experimental findings, hence the validity of the model will be verified.



---

# DAMAGE IDENTIFICATION FOR WHISPER 500 BLADE

---

On the basis of the experimental work documented in Chapter 3 and the finite element model developed in Chapter 4, modal and wavelet analysis-based level 1, 2 and 3 damage identification for the Whisper 500 blade is conducted in the present chapter in agreement with the methodology given in Chapter 2. In Section 5.1, initial modal analyses are performed for four different blade configurations, namely an intact and three damaged as listed below.

1. Intact blade, i.e. 0 mm crack.
2. Damaged blade with 50 mm longitudinal crack.
3. Damaged blade with 100 mm longitudinal crack.
4. Damaged blade with 200 mm longitudinal crack.

Through the modal analyses, the pre- and post-damage modal parameters are extracted for use in the actual damage identification. In Section 5.2, level 1 identification, i.e. damage detection, is conducted, and subsequently level 2 identification is presented in Section 5.3 as the crack is localized. In Section 5.4, level 3 identification, i.e. damage assessment, is carried out, and finally the findings in the aforementioned sections are summarized in Section 5.5, thus concluding the work with the Whisper 500 blade. It is noticed that the experimental tests with the Whisper 500 blade were conducted before level 2 and 3 damage identification was considered. This and the limited amount of available accelerometers have resulted in a non-optimal measurement setup, which will be treated in Section 5.4.

## 5.1 Modal analysis

Modal analyses are conducted both experimentally, see Subsection 5.1.1, and numerically, see Subsection 5.1.2, to extract the eigenfrequencies and mode shapes from the blade configurations listed introductory in the present chapter. In Subsection 5.1.3, the experimental and numerical results are compared and hereby the validity of the finite element model of the blade is verified. Further comparisons, i.e. of the alteration tendencies of the modal parameters for pre- and post-damage modes, are performed in Section 5.2 since this falls under damage detection.

### 5.1.1 Experimental

As described in Subsection 2.1.2, mode extractions from the experimental tests are carried out with polynomial fits of the frequency response functions by use of the Rational Fraction Polynomial-Z method. This is done in the PULSE Reflex software which is described in Chapter 3. In Fig. 5.1, an example of the frequency response functions obtained from the tests of the intact blade is given. Since the polynomial fits only yield valid approximations of the actual

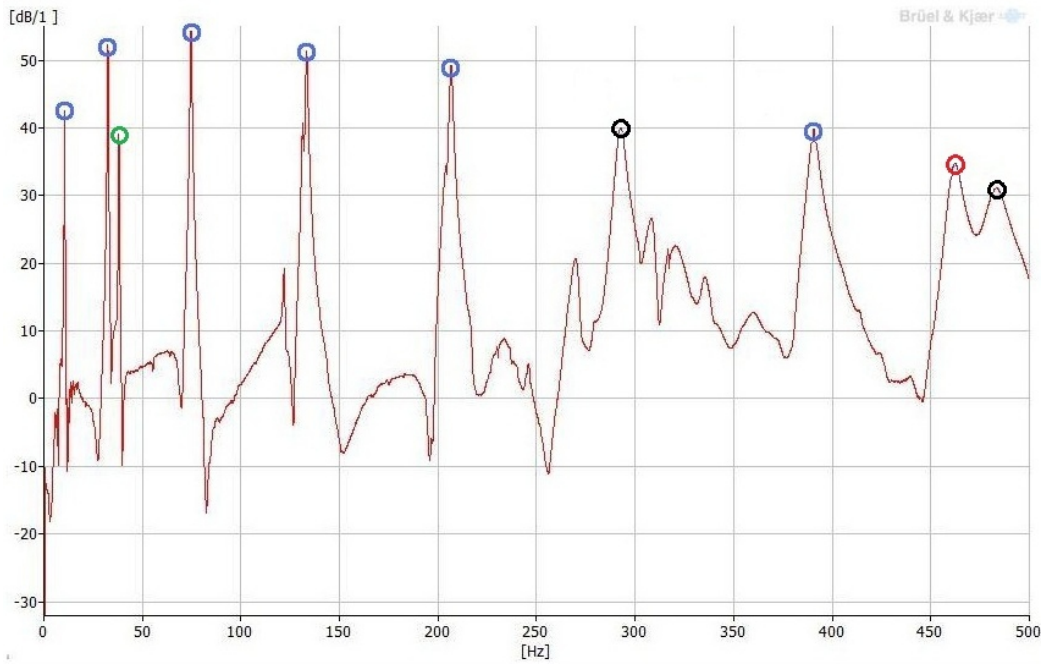


**Fig. 5.1:** Frequency response function extracted from B&K PULSE Reflex software. The blue circles mark flapwise bending modes, the green circle lagwise bending, the red circle edgewise bending and the black circles twisting.

frequency response functions when these are divided into small intervals, it is not possible to illustrate the synthesized counterpart to the function in Fig. 5.1.

The ten modes marked by circles in Fig. 5.1 were found consistently in all the tests of the

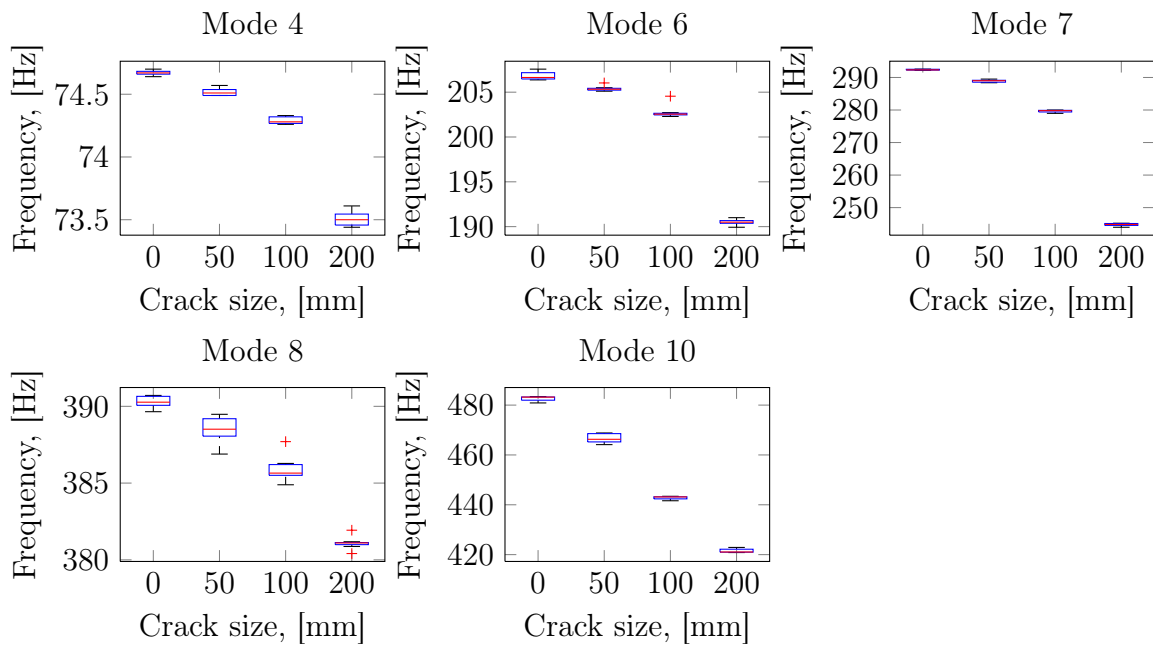


**Fig. 5.2:** Box-and-whisker plots of eigenfrequencies for modes 4, 6, 7, 8 and 10 based on different blade configurations.

intact blade and therefore these modes are chosen to post-process. As indicated in Fig. 5.1, the modes include flap-<sup>1</sup>, lag-<sup>2</sup> and edgewise<sup>3</sup> bending plus two twisting modes. In Table 5.1, the obtained eigenfrequency results and MACs for the ten modes are presented. Evidently, introduction of 50 mm, 100 mm and 200 mm cracks do not change modes 1, 2, 3, 5 and 9. In order to quantify the frequency changes in the other modes, the measurement uncertainties are considered through the box-and-whisker plots given in Fig. 5.2. The plots, which are based on ten independent tests, clearly show that the frequency changes in modes 4, 6, 7, 8 and 10 cannot be categorized as measurement uncertainties.

**Table 5.1:** Experimental findings for eigenfrequencies and corresponding MAC values. The reference of each MAC is the corresponding mode shape of the intact blade.

Modal results		Intact blade	50 mm crack	100 mm crack	200 mm crack
Mode 1	Frequency [Hz]	10.52	10.54	10.53	10.55
	MAC	1.0000	1.0000	1.0000	1.0000
Mode 2	Frequency [Hz]	32.50	32.50	32.50	32.50
	MAC	1.0000	0.9999	1.0000	1.0000
Mode 3	Frequency [Hz]	37.99	38.00	37.99	38.00
	MAC	1.0000	0.9990	0.9991	0.9994
Mode 4	Frequency [Hz]	74.65	74.51	74.29	73.50
	MAC	1.0000	0.9997	0.9996	0.9968
Mode 5	Frequency [Hz]	133.25	133.24	133.21	133.26
	MAC	1.0000	1.0000	1.0000	0.9995
Mode 6	Frequency [Hz]	206.60	205.71	202.70	190.50
	MAC	1.0000	0.9960	0.9826	0.7625
Mode 7	Frequency [Hz]	292.47	289.02	279.91	244.82
	MAC	1.0000	0.9568	0.6519	0.2827
Mode 8	Frequency [Hz]	390.52	388.28	385.38	381.03
	MAC	1.0000	0.9842	0.9330	0.7604
Mode 9	Frequency [Hz]	461.59	461.28	461.44	461.34
	MAC	1.0000	0.9974	0.9893	0.9818
Mode 10	Frequency [Hz]	482.47	467.00	443.42	421.42
	MAC	1.0000	0.8306	0.8419	0.5070

In order to reduce the amount of post-processing, it is chosen only to treat four modes, namely modes 1, 4, 6 and 7, in the later damage identification analyses. These specific modes are chosen because they, cf. Fig. 5.2 and Table 5.1, compose a mixture of modes which are, respectively, unaffected and affected by the cracks. In this way, the robustness of the identification methods is examined. In Fig. 5.3, the four chosen modes of the intact blade are illustrated. Furthermore, plots of all the intact blade mode shapes are presented in Appendix J.

<sup>1</sup>Flapwise: Direction perpendicular to the surface swept by the non-deformed rotor blade axis [49].

<sup>2</sup>Lagwise: In the plane of rotation, negative in rotational direction [49].

<sup>3</sup>Edgewise: Direction parallel to the local chord of the blade [49].

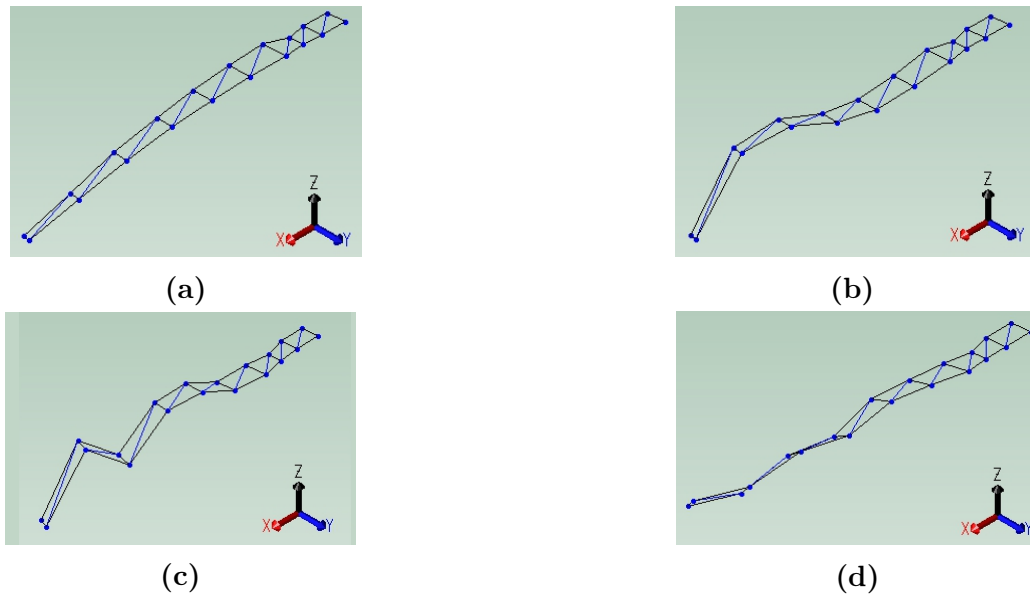


**Fig. 5.3:** Experimental findings for mode shapes of intact Whisper 500 blade model. (a) Mode shape 1. (b) Mode shape 4. (c) Mode shape 6. (d) Mode shape 7.

### 5.1.2 Finite element

By use of the calibrated finite element model developed in Chapter 4, the eigenfrequencies and MACs presented in Table 5.2 are obtained for the ten modes chosen in the experimental tests. It is noticed that the results differ from those presented in DAMAS paper 2. This is, of course, due to the change from isotropic to orthotropic material model for the shell. In Fig. 5.4, the

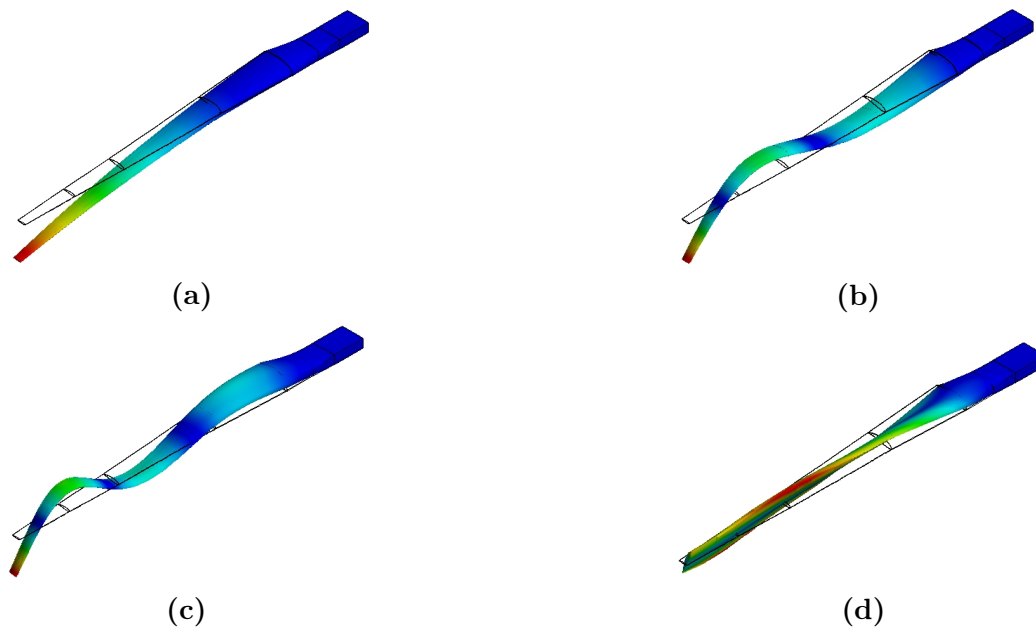


**Fig. 5.4:** Finite element-derived mode shapes of intact Whisper 500 blade model, with the wireframes being the undeformed states. (a) Mode shape 1. (b) Mode shape 4. (c) Mode shape 6. (d) Mode shape 7.

**Table 5.2:** Finite element analysis results for eigenfrequencies and corresponding MAC values. The reference of each MAC is the corresponding mode shape of the intact blade.

Modal results		Intact blade	50 mm crack	100 mm crack	200 mm crack
Mode 1	Frequency [Hz]	10.47	10.48	10.47	10.46
	MAC	1.0000	1.0000	1.0000	1.0000
Mode 2	Frequency [Hz]	33.24	33.22	33.22	33.21
	MAC	1.0000	1.0000	1.0000	0.9993
Mode 3	Frequency [Hz]	37.01	37.03	36.99	37.01
	MAC	1.0000	1.0000	0.9995	0.9983
Mode 4	Frequency [Hz]	75.66	75.53	75.38	74.17
	MAC	1.0000	1.0000	0.9995	0.9967
Mode 5	Frequency [Hz]	133.01	133.01	133.03	133.01
	MAC	1.0000	1.0000	0.9998	0.9995
Mode 6	Frequency [Hz]	198.60	197.99	194.87	181.73
	MAC	1.0000	0.9979	0.9461	0.7453
Mode 7	Frequency [Hz]	291.80	287.56	274.60	241.31
	MAC	1.0000	0.9399	0.6020	0.2355
Mode 8	Frequency [Hz]	405.94	403.38	399.95	393.89
	MAC	1.0000	0.9843	0.9246	0.7377
Mode 9	Frequency [Hz]	466.99	466.76	466.93	466.51
	MAC	1.0000	0.9981	0.9864	0.9797
Mode 10	Frequency [Hz]	497.01	474.69	450.03	432.11
	MAC	1.0000	0.8495	0.8411	0.4640

finite element-derived mode shapes of mode 1, 4, 6 and 7 are depicted. These four modes are used in the coming damage identification analyses.

### 5.1.3 Comparison of modal analysis results

In Table 5.3, the eigenfrequency results of modes 1, 4, 6 and 7 obtained through the finite element model, see Table 5.2, are compared with the corresponding experimental findings, see Table 5.1. Evidently, good correlation is obtained as it is seen that the biggest deviation occurs in mode 6 of the 200 mm cracked blade configuration where the finite element analysis result is 4.60 % smaller than the corresponding experimental finding. Furthermore, it is noticed that similar correlation is obtained for the remaining modes, i.e. modes 2, 3, 5, 8, 9 and 10, for which the biggest deviation occurs in mode 8 of the intact blade where the finite element analysis result is 3.95 % larger than the corresponding experimental finding.

To verify that the modes found in the finite element analyses are corresponding to the experimental findings, the consistency of the mode shapes is examined via the MAC values. In Fig. 5.5, the MAC values for mode shapes 1, 4, 6 and 7 are illustrated. Evidently, the mode shapes obtained in the finite element analyses correlate acceptably with the corresponding experimental mode shapes since the MAC values in the diagonals approach unity. The biggest

**Table 5.3:** Percentage deviation between experimental eigenfrequency findings and corresponding finite element-derived results. The experimental values are used as reference.

Mode	Intact blade	50 mm crack	100 mm crack	200 mm crack
1	0.48	0.57	0.57	0.85
4	-1.35	-1.37	-1.47	-0.91
6	3.87	3.75	3.86	4.60
7	0.23	0.51	1.90	1.43

deviation between the diagonal MAC values is found in mode 6 of the blade with a 100 mm crack, where the MAC value is 0.8745. When comparing the results in Tables 5.1 and 5.2, the reason to this relatively low MAC value is displayed; the experimental mode shape only changes 1.74 % in proportion to the corresponding intact blade mode shape, while the analog FE mode shape changes 5.39 % compared to its corresponding intact blade mode shape. By comparison of the results in Tables 5.1 and 5.2, it is also seen, due to the unity condition, that acceptable correlations are obtained for the percentage changes of the experimental and numerical MAC values. The maximum decrease for both is approximately 75 %, obtained in mode 7 for the blade configuration with 200 mm crack. This is further addressed in Section 5.2.

It can be concluded that the finite element model represents the four chosen modes validly, but it is noticed that the MAC values generally decrease with increasing modes. This is due

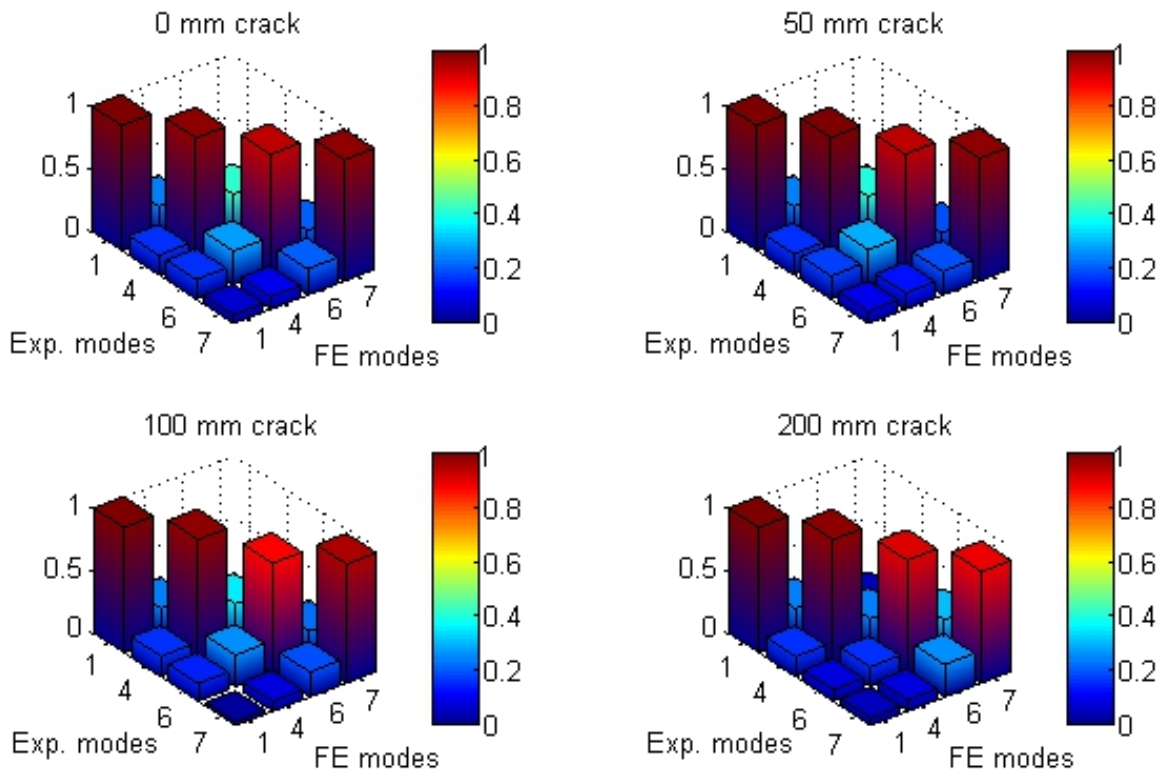


**Fig. 5.5:** Comparison of experimental (Exp.) and finite element (FE) mode shapes of the Whisper 500 blade via MAC values.

to an increased sensitivity towards structural deviations in the high-frequency modes. For the remaining modes, i.e. modes 2, 3, 5, 8, 9 and 10, the same tendencies are obtained.

## 5.2 Damage detection

The damage detection is a natural continuation of the modal analysis since the detection, cf. Section 2.2, consists of direct comparison of the pre- and post-damage eigenfrequencies and mode shapes. This is done in Fig. 5.6 where change of the modal parameters are plotted versus the crack size.

It is seen in Fig. 5.6a that the eigenfrequency of mode 1 is insignificantly changed in both the experimental findings and the finite element analysis results. Eigenfrequency number 4 is slightly decreased with enlarged crack size. The same goes for eigenfrequency number 6 with 50 mm and 100 mm cracks, but with a 200 mm crack, this eigenfrequency is decreased sig-

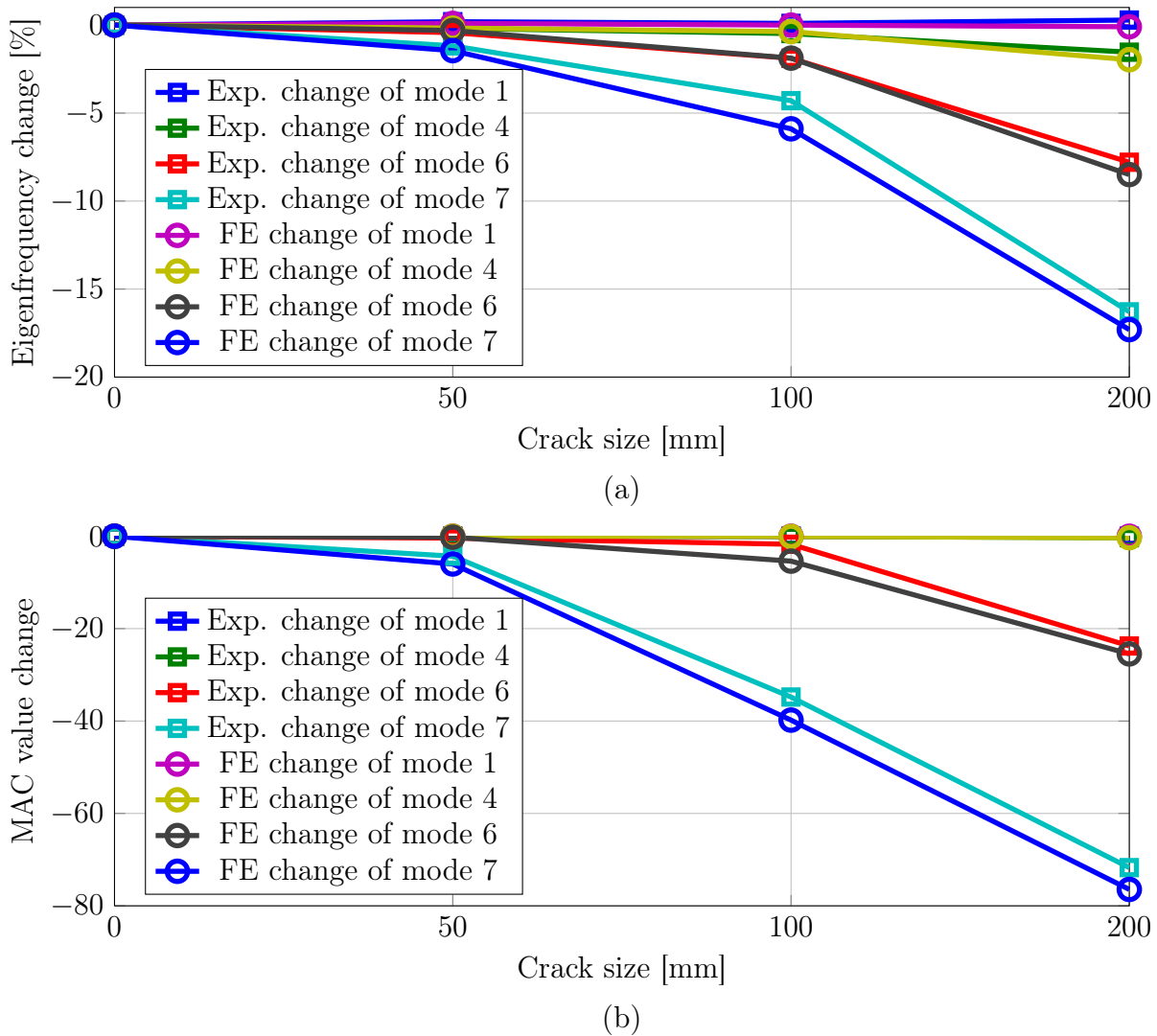


**Fig. 5.6:** Change of modal parameters as function of crack size. (a) Percentage frequency change. (b) MAC value change.

nificantly due to slight introduction of twisting in the tip of the blade. This phenomenon is captured in both the experiments and in the FE analysis. Finally, it is seen that the eigenfrequency of mode 7, i.e. a twisting mode, is sensitive towards even the 50 mm crack which results in eigenfrequency decreases of approximately 1.2 % and 1.5 % in the experimental test and finite element analysis, respectively. However, as stated in Subsection 2.3.1, environmental effects can account for up to 5 % changes in eigenfrequencies, thus based on solely the eigenfrequencies the crack is only detected in modes 6 and 7 with a 200 mm crack. The biggest eigenfrequency change is obtained in the latter mode where decreases of 16 % and 17 % are found via experimental test and finite element analysis, respectively.

Contrary to the eigenfrequencies, the plots in Fig. 5.6b imply that the mode shapes are very sensitive towards the cracks, and since the mode shapes are not as affected by environmental effects as the eigenfrequencies, a MAC change of, e.g., 5 % is a clear indication of abnormalities such as structural damage. This MAC change is evidently obtained in mode 7 already with a 50 mm crack, thus confirming the statement given in Section 2.2 that the mode shape of a twisting mode is highly sensitive towards longitudinal cracks. This is further confirmed by the other twisting mode of the Whisper 500 blade, i.e. mode 10, see Tables 5.1 and 5.2.

### 5.3 Damage localization

The damage detection shall be regarded as an initial examination of the health of the specific structure. Further details of the damage are obtained when employing the localization and assessment methods. As shown in Sections 2.3 and 2.4, the chosen localization method, i.e. wavelet analysis, is also utilized for damage assessment. This will be shown for the Whisper 500 blade in Section 5.4.

In the present section, wavelet analysis of both experimentally and numerically derived mode shapes for modes 1, 4, 6 and 7 is conducted. It is noticed that the numerical mode shapes are obtained on the basis of modal displacements at the locations of the accelerometers in the experimental setup, thus the same measurement points are used in the analyses. Since the amount of mounted accelerometers is relatively sparse, placed solely along the two blade edges, a one-dimensional wavelet analysis approach is chosen. By applying the Gaussian wavelet and the inter- and extrapolation procedure described in Subsection 2.3.1 to the mode shapes of the Whisper 500 blade, the damage localization plots illustrated in Fig. 5.7 are obtained for the 50 mm crack configuration. Since the crack is placed between accelerometers 7 and 8, it is seen that the crack, despite the sparse number of accelerometers, is localized acceptably in all modes. However, especially for the experimental findings, wavelet peaks not governed by the crack are introduced, due to both noise contamination and sparse sampling density. This is also the case for the other damage configurations, i.e. with a 100 mm and 200 mm crack, where the peaks at accelerometers 7 and 8, however, become more distinct.

Tables 5.1 and 5.2 show that the MAC values obtained for mode 1 imply that no change occurs in this mode shape when the cracks are introduced. Despite this, the cracks are detected and localized by use of wavelet analyses. With a crack length of 50 mm, however, the localization is ambiguous since some peaks in non-damaged areas are larger than the peak at accelerometer 8, but generally it is concluded that the low-frequency bending modes can be utilized in damage identification. This conclusion is further validated in the damage assessment, see Section 5.4, where an increase in measurement points results in accurate damage localization in mode 1 with the 50 mm crack.



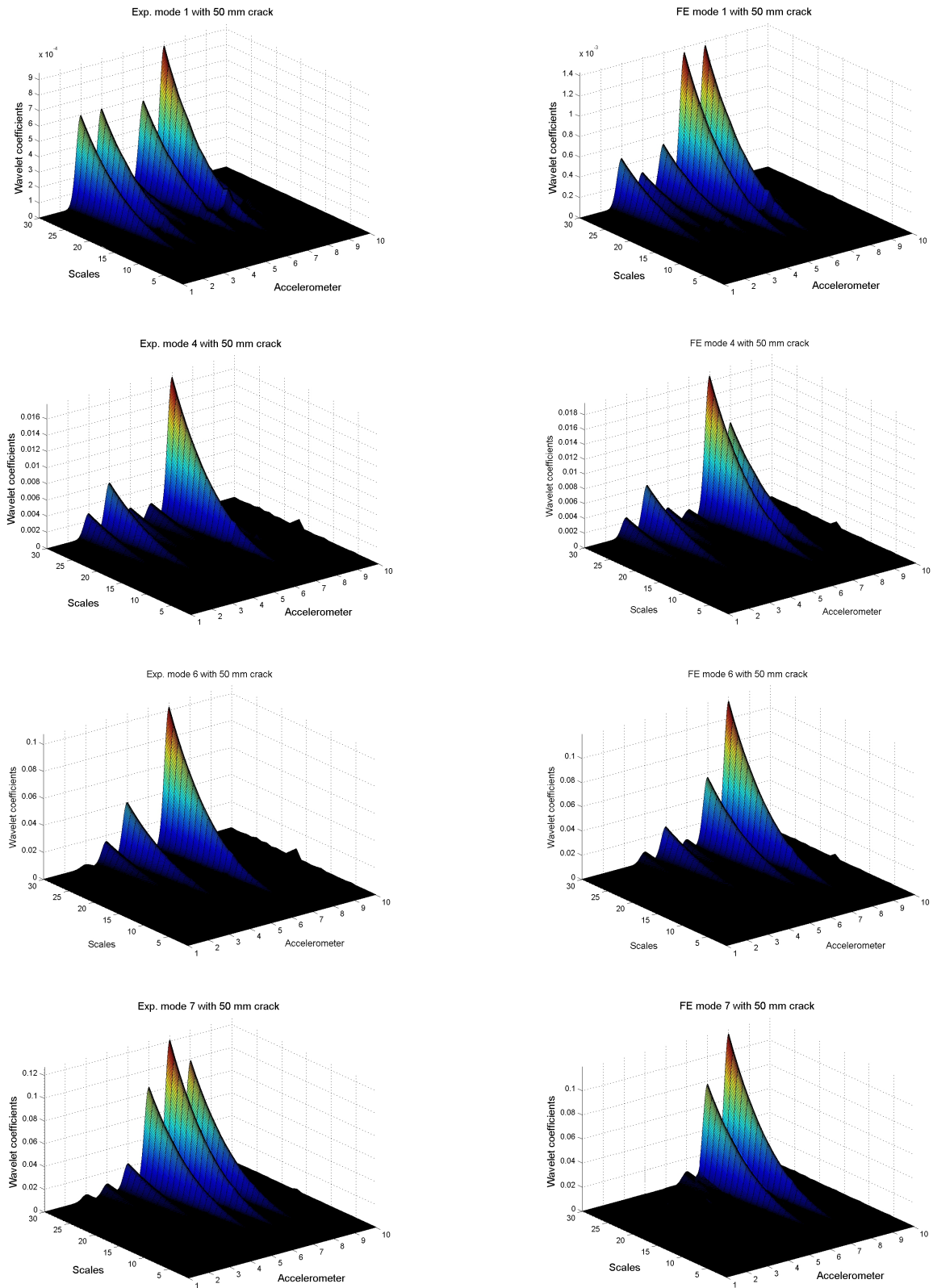


**Fig. 5.7:** Crack localization based on mode shapes 1, 4, 6 and 7 of the Whisper 500 blade for both experimental test and finite element analysis with a 50 mm crack placed between accelerometers 7 and 8.

## 5.4 Damage assessment

In Section 2.4, it is described how level 3 damage identification is divided into damage length assessment and damage depth assessment, respectively. Due to the sparse number of accelerometers mounted on the Whisper 500 blade, neither length assessment nor depth assessment can be conducted accurately. However, as the plots in Fig. 5.7 suggest, both the experimental findings and the finite element analysis results for modes 4, 6 and 7 yield wavelet coefficient peaks at the measurement points nearest the crack, i.e. at accelerometers 7 and 8. Regarding the depth assessment, it is also seen in Fig. 5.7 that reasonable agreement between the experimentally and numerically derived wavelet coefficient magnitudes are obtained. Indeed, this, and the locations of the wavelet coefficient peaks for modes 4, 6 and 7, imply that an increase of measurement points will enhance the damage assessment. Despite that mode 1 fails to yield localization of the damage, the influence of increased measurement points will be examined by using this mode. Mode 1 is chosen because it is preferable, in general, if this mode can be utilized since it typically is easiest to obtain in practice and is least sensitive towards structural deviations, hence it is easier to reach agreement between experimental findings and a finite element model. Furthermore, use of mode 1 means that the more complicated orthotropic material model can be omitted in favor of a significantly simpler isotropic material model. It will therefore be tested if the small sensitivity towards structural deviations is sufficient to assess the damage length and depth when 45 instead of the initial ten measurement points are applied along each blade edge. 45 measurement points yield spatial measurement increment of  $\Delta x = 50$  mm and ensure that measurement points are placed precisely at the start and end of the 50 mm crack.

### 5.4.1 Crack length

The crack length assessment is carried out in analogy to the method presented in Subsection 2.4.1, i.e. a threshold,  $\Pi$ , is applied to emphasize the damage-governed wavelet coefficient peaks. By use of  $\Pi = 0.7$ , the wavelet coefficients plotted in Fig. 5.8 are derived. It is noticed that the crack starts at the location of measurement point 30 and ends at the location of measurement point 31, thus the crack is accurately localized which means that the crack length is also accurately assessed to 50 mm. It is noticed that the applied threshold is higher than the one utilized in Subsection 2.4.1, i.e.  $\Pi = 0.5$ . The value of the threshold must be chosen in accordance with the signal purity which is governed by, e.g., noise contamination, number of measurement points and structural complexity. This suggests that a statistical measure, such as root mean square (RMS) value, can be used as threshold. However, this statistical approach has been tested for both the cantilevered rectangular shell tube and the Whisper 500 blade, and it is found that the RMS is inapplicable since it generally yields too small a value. For instance, the wavelet coefficients for the first mode of the Whisper 500 blade with 45 measurement points yield

$$\text{RMS} = \sqrt{\frac{1}{n}(x_1^2 + x_2^2 + \dots + x_n^2)} = 9.9 \cdot 10^{-6} \quad (5.1)$$

when using only the coefficients at maximum scale, i.e.  $a = 30$ , with  $n$  samples. By comparison, the four largest wavelet coefficients are  $\max_1(\text{CWT}) = 5.5 \cdot 10^{-5}$ ,  $\max_2(\text{CWT}) = 5.3 \cdot 10^{-5}$ ,  $\max_3(\text{CWT}) = 3.1 \cdot 10^{-5}$  and  $\max_4(\text{CWT}) = 2.4 \cdot 10^{-5}$  at  $a = 30$ . The first two maxima are

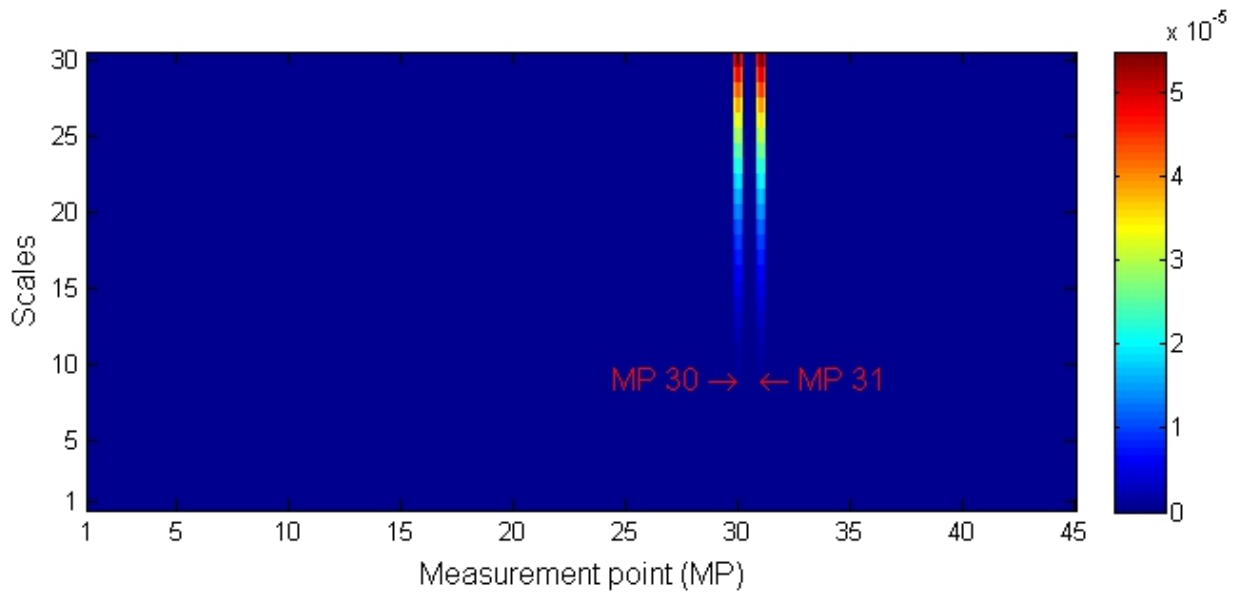


**Fig. 5.8:** CWT coefficients for first mode shape of Whisper 500 blade with a 50 mm crack starting and ending at measurement points 30 and 31, respectively. The threshold  $\Pi = 0.7$  is applied.

located at measurement points 30 and 31, respectively, while the two other maxima are located at measurement points 29 and 32, respectively, thus the threshold of  $\Pi = 0.7$  is necessary to obtain an accurate crack length assessment.

### 5.4.2 Crack depth

As described in Section 2.4.2, the crack depth assessment is based on the assumption of a constant Hölder exponent. In Fig. 5.9, the validity of this assumption for the Whisper 500

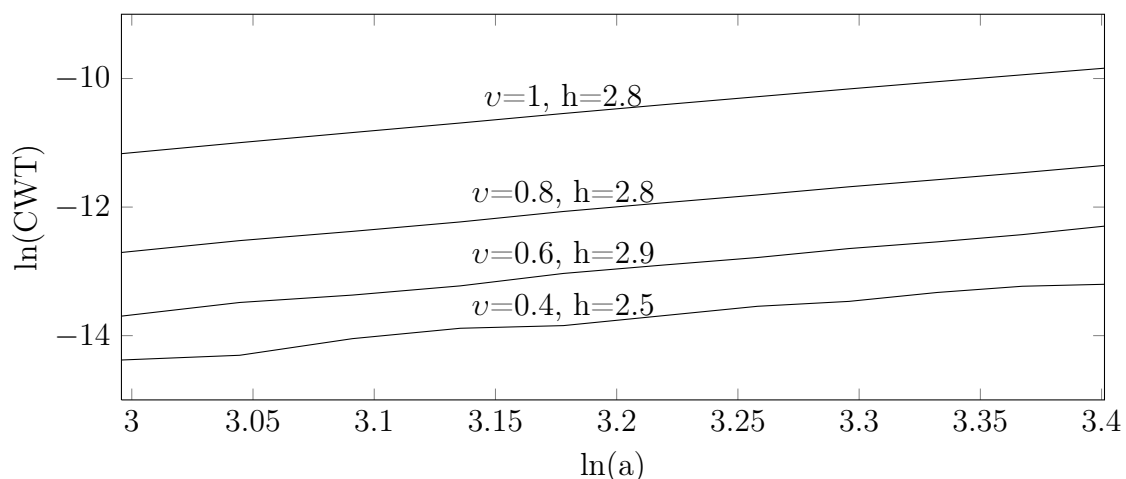


**Fig. 5.9:** Wavelet coefficient, CWT, versus scale,  $a$ , for different crack depth-configurations of the first mode of the Whisper 500 blade with a 50 mm long crack.  $v$  and  $h$  denote relative crack depth and Hölder exponent, respectively.

blade is examined, and here it is seen that the relative crack depth must be  $v \geq 0.6$  for the Hölder exponent to be approximately constant. When increasing the crack length to 100 mm and 200 mm, respectively, it is found that the Hölder exponent stabilizes for smaller relative crack depths, thus facilitating assessment of cracks with smaller depths. More ambiguous results are obtained when examining the effects of utilizing the higher modes, as it is found that some modes yield stabilization with smaller crack depths than the first mode while other modes demand bigger crack depths.

Since a constant Hölder exponent is necessary to make the crack depth assessment method applicable, the results for a crack with a relative depth of  $v = 0.4$  are omitted in the further analyses. Consequently, the intensity function, which is plotted in Fig. 5.10, facilitates crack depth assessment of cracks with  $v \geq 0.6$ . In order to validate this, a crack with  $v = 0.75$  has been introduced in the finite element model of the blade and hereby an intensity factor of  $\Gamma = 1.12 \cdot 10^{-10}$  has been derived. The corresponding value predicted by the intensity function in Fig. 5.10 is  $\Gamma = 1.04 \cdot 10^{-10}$ , thus it is concluded that accurate crack depth assessment for  $v \geq 0.6$  can be conducted by use of the proposed intensity function method.

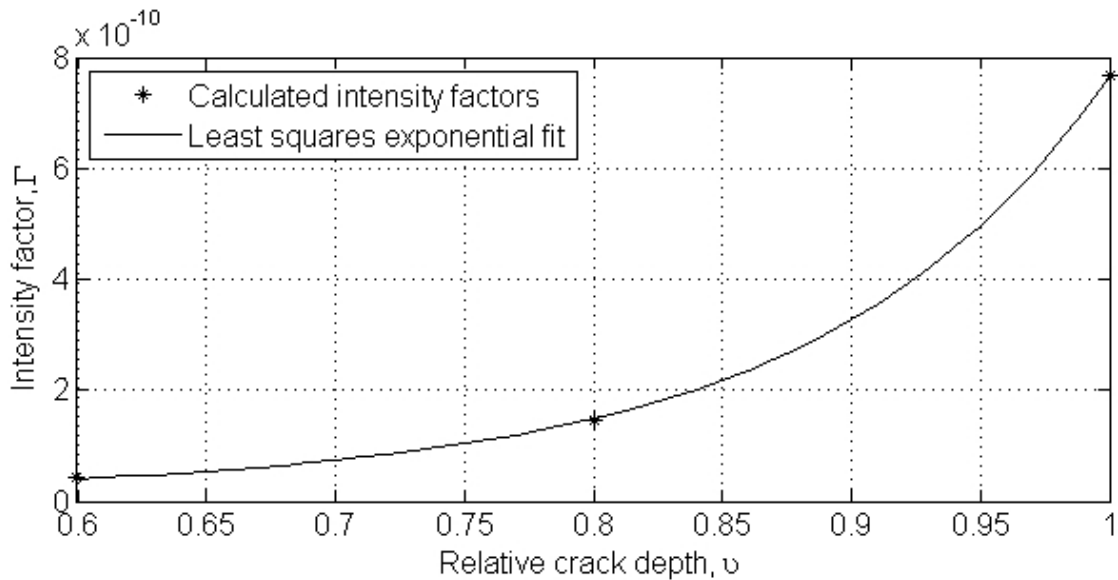


**Fig. 5.10:** Intensity factor,  $\Gamma$ , as function of relative crack depth,  $v$ , for the Whisper 500 blade with a 50 mm long crack.

## 5.5 Summary

The present chapter documents the results obtained by modal and wavelet analysis-based level 1, 2 and 3 damage identification for a residential-sized wind turbine blade, namely Whisper 500, introduced to 50 mm, 100 mm and 200 mm longitudinal cracks. The theory behind the employed methods is described and validated in Chapter 2.

In Section 5.1, the results of the experimental and numerical modal analyses of the Whisper 500 blade are presented and compared. The results, in the form of eigenfrequencies and MAC values, are presented in Tables 5.1 and 5.2 for the experimental tests and finite element analyses, respectively. When comparing these results, as done in Table 5.3, it is evident that

acceptable agreement is obtained, thus it can be concluded that the calibrated finite element model composes a valid representation of the ten modes examined for the Whisper 500 blade. To reduce the amount of post-processing, it is chosen only to treat modes 1, 4, 6 and 7, see e.g. Fig. 5.3 and Fig. 5.4, in the damage identification analyses. The specific modes are chosen because they compose a mixture of modes which are, respectively, unaffected and affected of the cracks. In this way, the robustness of the identification methods are examined.

Level 1 damage identification, i.e. damage detection, is conducted in Section 5.2, where it is documented how the modal parameters of the four selected modes are affected by the different cracks. As expected, due to the analyses in Chapter 2, Fig. 5.6 shows that the mode shapes are much more sensitive towards the cracks than the eigenfrequencies and when recalling that environmental effects can account for up to 5 % changes in eigenfrequencies, the crack can by use of solely eigenfrequencies in practice only be detected in modes 6 and 7 when the crack is 200 mm. For comparison, the MAC value of mode shape 7 decreases approximately 5 % when the 50 mm is introduced and since the mode shapes are less sensitive towards environmental effects, this change clearly implies abnormalities, e.g. structural damage. Consequently, the mode shapes are regarded as primary damage indicator.

Through wavelet analysis of the post-damaged mode shapes of modes 1, 4, 6 and 7, damage localization has been conducted in Section 5.3. The results for the 50 mm crack are illustrated in Fig. 5.7, and it is found that generally the global wavelet coefficient maxima are located at the measurement points closest to the crack for all three crack configurations. Thus, despite that the MAC values for, e.g., mode 1 imply that no significant mode shape change occurs when introducing a longitudinal crack, see Fig. 5.6b, the wavelet analyses capture discontinuities as a result of the cracks.

Due to the sparse number of measurement points, level 3 identification, i.e. damage length and depth assessment, cannot be conducted based on the experimental findings. Instead, the number of measurement points is increased in the finite element model and hereby the damage assessment can be conducted accurately. This is documented in Section 5.4, where the plot in Fig. 5.8 shows that the crack is accurately localized and length-assessed when 45 measurement points are applied on each blade edge instead of the initial ten. Furthermore, it is found in Section 5.4 that the crack depth can be assessed by use of intensity factors derived from wavelet analyses.

Summarizing the findings in the present chapter, it can be concluded that the modal analysis-based damage identification approach succeeds in level 1, 2 and 3 identification when an appropriate amount of measurement points are employed. The results in Fig. 5.7 suggest that the noise contamination of the experimental findings is limited and therefore the influence of noise is not investigated. This is, however, done for the full-scale blade in Chapter 7 as it can be expected that significant noise contamination occurs in measurements of blades in in-service conditions.

---

# FINITE ELEMENT MODEL OF GE 1.5 XLE BLADE

---

The GE 1.5 XLE finite element blade model developed in the present chapter is based on a geometry from [31]. In Section 6.1, this blade geometry is described briefly. Subsequently, the material properties of the blade are tabulated in Section 6.2, where the employed material model is also presented. In Section 6.3, the geometric boundary conditions are described, and then, in Section 6.4, the discretization of the blade is treated. The chapter is concluded in Section 6.5, where a summary of the descriptions in the aforementioned sections is provided.

It is noticed that several finite element aspects treated in this chapter are similar to those described in the development of the Whisper 500 blade finite element model, and therefore these aspects will not be elaborated in the present chapter. Instead, the reader is referred to Chapter 4.

## 6.1 Geometry

The GE 1.5 XLE wind turbine blade is 41.2 m long and composed of an outer surface and an inner shear web along the entire blade length. The blade geometry is presented in Fig. 6.1a and also in Fig. 6.1b, where a split view is given to specify the blade components.

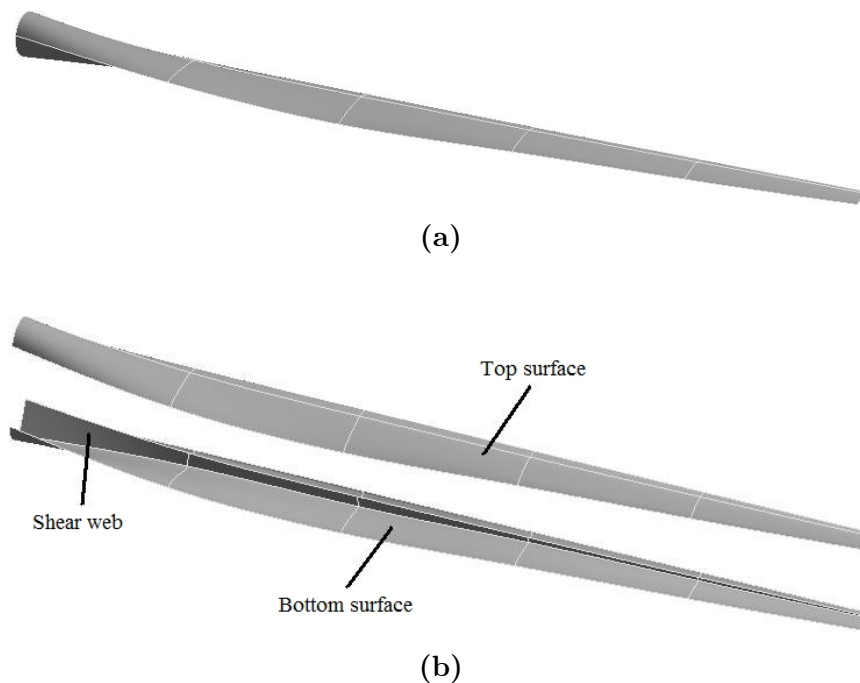


**Fig. 6.1:** GE 1.5 XLE blade model. (a) Full blade geometry. (b) Split geometry view with specification of blade components.

The shear web has a constant thickness of 0.02 m while the outer surface is of linear varying thickness, expressed by [31]

$$T(x) = 0.03 - 0.00048485x, \quad (6.1)$$

where  $x$  is the longitudinal blade coordinate, see Fig. 6.2, i.e.  $x = 0$  m is at the blade root and  $x = 41.2$  m is at the blade tip. The varying thickness is principled illustrated in Fig. 6.2, where the global coordinate system is also shown. This coordinate system will be utilized throughout the analyses of the GE 1.5 XLE blade. In Appendix K, a tutorial on how to apply varying thickness in ANSYS Workbench is given.

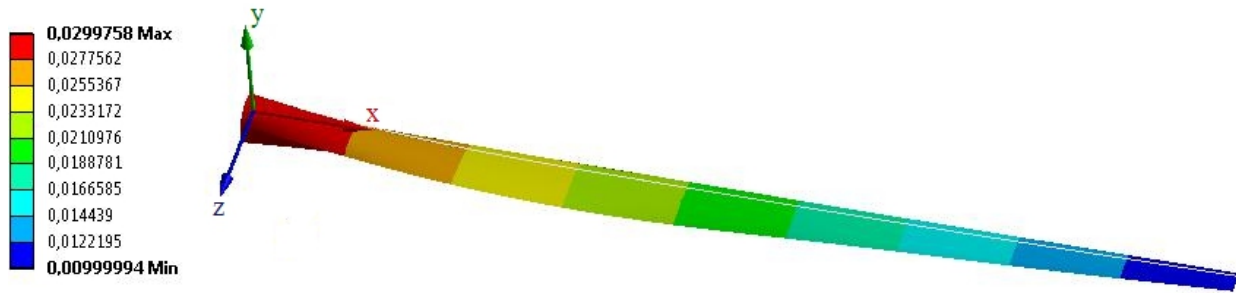


**Fig. 6.2:** Illustrative description of the varying thickness, in meters, of the GE 1.5 XLE blade surface with specification of global coordinate system.

The damage modeling for the GE 1.5 XLE blade is conducted in analogy to the procedure for the Whisper 500 blade, see Subsection 4.1.1, and will therefore not be described in the present section.

## 6.2 Material

In the lack of specific material data for the GE 1.5 XLE blade, both the outer surface and the shear web is assigned a one-layer glass fibre reinforced plastic (GFRP) material with an orthotropic material model. The material parameters are presented in Table 6.1, where the coordinates are for the local element coordinate system, see e.g. Fig. 4.5a. For more information about orthotropic material modeling, see Section 4.2 and Appendix A of the present report.

**Table 6.1:** Material parameters used in analyses of the GE 1.5 XLE wind turbine blade [50]. The unit of the Young's and shear moduli,  $E$  and  $G$ , is GPa and the unit of the density,  $\rho$ , is  $\text{kg}/\text{m}^3$ .

Material parameters for GFRP									
$E_x$	$E_y$	$E_z$	$\nu_{xy}$	$\nu_{yz}$	$\nu_{xz}$	$G_{xy}$	$G_{yz}$	$G_{xz}$	$\rho$
11.511	11.511	4.552	0.204	0.305	0.305	2.922	1.406	1.406	1400

## 6.3 Boundary conditions

Since the finite element analyses of the GE 1.5 XLE blade model are conducted as free-vibration analyses, no static boundary conditions are applied. The geometric boundary condition is chosen as a fixation, i.e. no translational and rotational movements, of the outer surface root.

## 6.4 Discretization

The blade model is discretized by use of second order shell elements, i.e. SHELL281 as presented in Subsection 4.5.1, with a size of 0.15 m. The element size is chosen on the basis of a convergence study of the low-frequency modes of the GE 1.5 XLE blade model. In order to enhance the mesh regularity, the Mapped Face Meshing function<sup>1</sup> is applied, thus resulting in the mesh shown in Fig. 6.3.

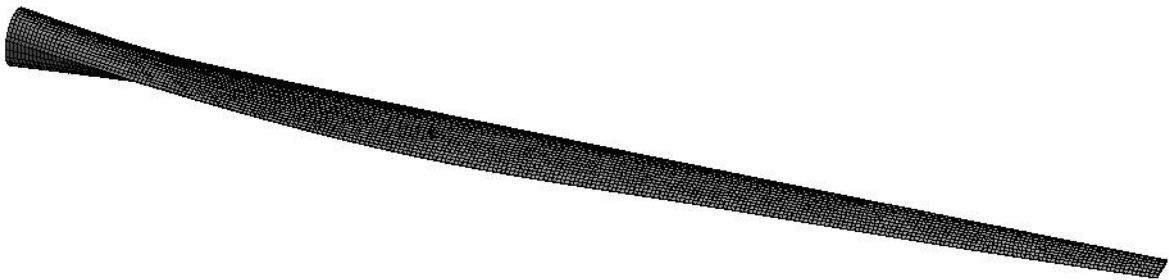


**Fig. 6.3:** Element mesh of the GE 1.5 XLE blade model.

Since all components are modeled with shell elements in a single layer, no substructuring is necessary. The full model with 0.15 m-sized elements contains 6,322 elements, of which only 1,097 are in the shear web, thus no significant reduction of computational time will be obtained by implementing a superelement for this component.

## 6.5 Summary

In the preceding sections of this chapter, the finite element model of the GE 1.5 XLE wind turbine blade is described in terms of geometry, material, boundary condition and discretization. In Section 6.1, the geometry is presented and the structural components, i.e. blade surface and shear web, are specified with regard to dimensions. Next, it is described in Section 6.2 how the blade is assigned an orthotropic material model, with glass fibre reinforced plastic (GFRP) being the material. The boundary conditions are addressed in Section 6.3, and as it is described here, only a geometric boundary condition is applied since the analyses are conducted as free-vibration analyses. Finally, the model discretization is treated in Section 6.4, where it is chosen to discretize the entire model by use of second order shell elements (SHELL281).

---

<sup>1</sup>Mapped Meshing: restricts element shapes to quadrilaterals and hexahedra and seeks a regular mesh pattern.



# DAMAGE IDENTIFICATION FOR GE 1.5 XLE BLADE

In the present chapter, identification analyses are conducted for the GE 1.5 XLE wind turbine blade finite element model developed in the previous chapter. The identification analyses are not conducted in the same stringent manner as it was done for the rectangular shell tube and the Whisper 500 blade, see e.g. Chapters 2 and 4, because the scope of the GE 1.5 XLE blade analyses is to examine the influence of different damage scenarios and noise contamination. The damage scenarios refer to the type of damage, in accordance with the classification presented in Section 1.1, plus damage placement, damage size and number of damages, i.e. both single- and multi-damage configurations are analyzed.

In Section 7.1, the different damage scenarios are presented, and in Section 7.2 it is shown how the points for extraction of modal displacements are placed. In Section 7.3, the criteria for valid damage identification are established. These criteria serve to ensure consistent evaluation of the identification analysis results such that the influence of the damage scenarios and noise contamination can be documented in Section 7.4, where the single-damage scenarios are treated. On the basis of these scenarios, different multi-damage scenarios are chosen and examined in Section 7.5. The damage identification analyses in Sections 7.4 and 7.5 are primarily conducted for the first mode of the blade, because it, due to the structural simplicity and easy accessibility, is desirable if this mode can be employed. The first mode of the blade is the flapwise bending mode depicted in Fig. 7.1a. However, as it will be evident from the damage identification

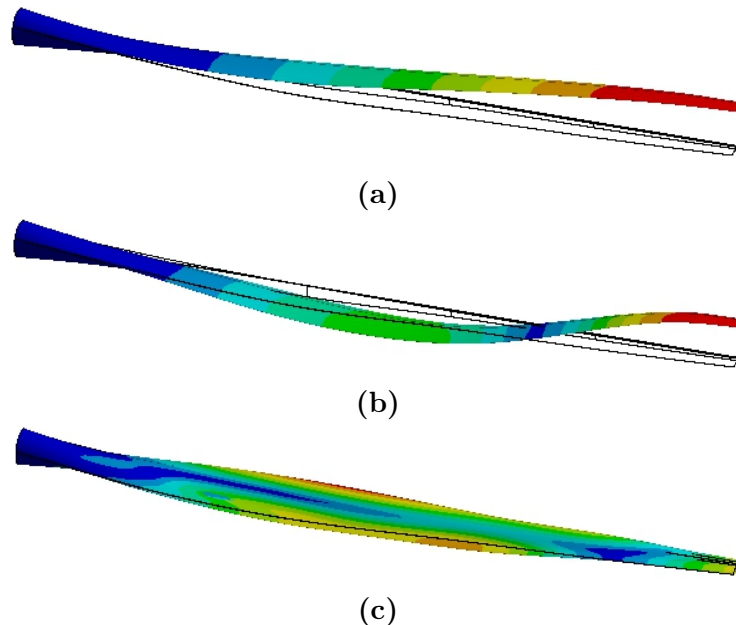


**Fig. 7.1:** Structural modes of GE 1.5 XLE blade model, with the wireframes being the undeformed states. (a) First mode (first flapwise bending). (b) Third mode (second flapwise bending). (c) Seventh mode (first twisting).

analyses, all the introduced damages cannot be identified in mode 1, and therefore also the second flapwise bending mode, i.e. mode 3, and the first twisting mode, i.e. mode 7, will be employed when necessary. These mode are shown in Fig. 7.1b and Fig. 7.1c, respectively.

## 7.1 Description of individual damages

The damage types treated in the present chapter are edge damages, in the form of debondings, and cracks in longitudinal and transverse direction, chosen because they, c.f. Section 1.1, compose the most critical damage types. The debondings are introduced along the leading and trailing edges, while the longitudinal and transverse cracks are introduced on the top blade surface. It is noticed that all the damages, due to their structural nature, are treated as trough-going, i.e. the debondings penetrate the entire joint between the top and bottom blade surfaces and the cracks penetrate the entire top blade surface thickness.

Generally, the damage types are analyzed in terms of both size and location. The former implies that multiple damage lengths are introduced alternately, in accordance with damage inspections conducted in [9], such that the damage lengths introduced in the GE 1.5 XLE blade proportionally correspond to the findings in [9]. In the listing below, the introduced damage lengths and widths are presented. It is noticed that the transverse cracks are unscaled since no data for the width of the inspected blades are accessible.

- Debondings: 0.5 m, 1 m and 2 m long.
- Longitudinal cracks: 0.5 m, 1 m and 2 m long. All with a width of 0.005 m.
- Transverse cracks: 0.05 m long and with a width of 0.005 m.

In order to organize the different damage locations, the blade is divided into five sections in which all the different damages are introduced and analyzed in turns. This is illustrated in Fig. 7.2.

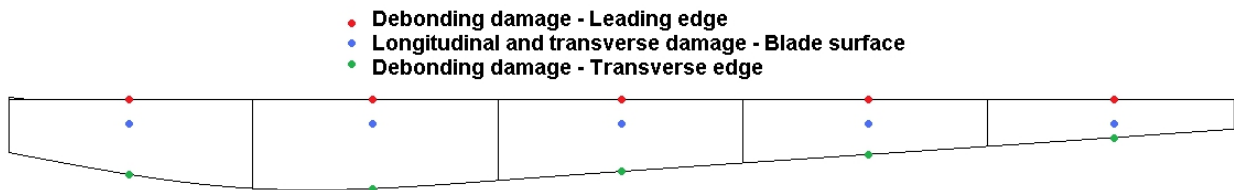


**Fig. 7.2:** Illustration of section-divided GE 1.5 XLE blade with marking of the damage location-center for each damage type.

## 7.2 Measurement points

The mode shapes employed for damage identification analyses are based on the modal displacements, which are extracted at predefined measurement points. It is chosen to place the measurement points with an increment of 0.15 m in longitudinal direction and an increment of 0.05 m in transverse direction.

For the debonding damages, one-dimensional wavelet analyses are conducted for each edge, while cracks are analyzed by use of two-dimensional wavelet analyses. In Fig. 7.3, the measurement points are illustrated. Evidently, a grid is applied on a part of the top blade surface to facilitate two-dimensional wavelet analyses. The specific grid configuration is chosen such that the amount of post-processing is limited, but still such that the damaged areas are covered. It is noticed that the density of measurement points is not investigated, because studies of available measurement technologies, equipment installation, etc. have not been a focus area in the present report.



**Fig. 7.3:** Measurement lines (red) for one-dimensional wavelet analyses of debondings, and measurement grid (blue surface) for two-dimensional wavelet analyses of cracks. It is remarked that a local coordinate line,  $\zeta_t$ , is placed along the trailing edge.

## 7.3 Criteria for valid identification

In order to evaluate the quality of the damage identification in a consistent way, a classification system is introduced. In Subsection 7.3.1, the criteria for valid damage localization are presented, and subsequently the criteria for accurate assessment are described in 7.3.2.

### 7.3.1 Localization

The damage localization of each damage scenario is evaluated by use of the scores 1, 2 and 3. The meaning of these scores and when to apply them is defined in Table 7.1. The scores are utilized consistently in the damage identification analyses of the GE 1.5 XLE blade.

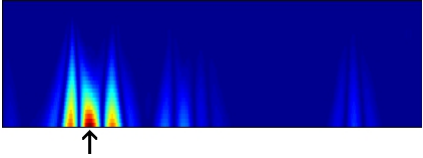
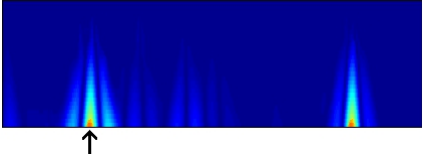
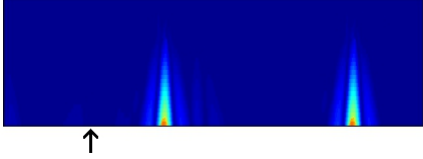
### 7.3.2 Assessment

After the damage localization score is given, an additional assessment score, in the form of + or ÷, is given. The meaning of these latter scores and when to apply them is defined in Table 7.2. It is noticed that valid assessment is obtained for assessed damage lengths that lie within 80-120 % of the actual damage length. This percentage interval is chosen as a result of brief damage assessment studies.

## 7.4 Single-damage identification analyses

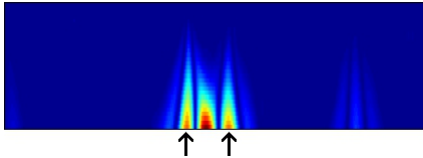
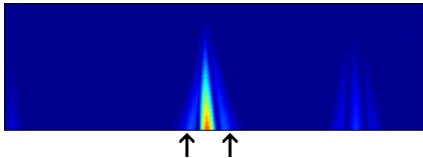
In the present section, the damages emphasized in Section 7.1 are introduced alternately, thus composing 50 single-damage scenarios. These scenarios are analyzed with regard to damage identification in Subsections 7.4.1 - 7.4.4, and subsequently the findings are compared and summarized in Subsection 7.4.5.

**Table 7.1:** Overview of damage localization scores. The arrows on the wavelet plots mark the damage location.

Score	Score meaning	Wavelet result
1	Unambiguous damage localization, seen by occurrence of distinct maximum peak at damage location.	
2	Ambiguous damage localization, seen by multiple similar maximum peaks at and away from damage location.	
3	No damage localization, seen by distinct maximum peaks away from the damage location.	

It is noticed that, unless stated otherwise, the identification analyses are based on the first flapwise bending mode depicted in Fig. 7.1a, both with and without noise contamination. The noise is added as white Gaussian noise with regard to a signal-to-noise ratio (SNR), as described in Appendix D, to examine the robustness of the damage identification method for a full-scale wind turbine blade. The specific SNRs employed in the analyses are chosen on the basis of preliminary analyses which have implied how much noise is needed to completely eliminate the applicability of the wavelet analysis method. The lowest SNR, i.e. the ratio yielding most

**Table 7.2:** Overview of damage assessment scores. The arrows on the wavelet plots mark the damage start and end, thus composing the damage length.

Score	Score meaning	Wavelet result
1	Valid damage assessment, since the assessed length is within 80-120 % of the actual damage length.	
2	Invalid damage assessment, since the assessed length is not within 80-120 % of the actual damage length.	

noise, has then been set to a value slightly higher than the found minimum, resulting in the use of SNR = 60 dB, SNR = 50 dB and SNR = 40 dB for the first flapwise bending mode shape signal. In Fig. 7.4, this mode shape signal along the leading edge of the undamaged GE 1.5 XLE blade model is plotted for the employed noise settings to illustrate the amount of added noise.

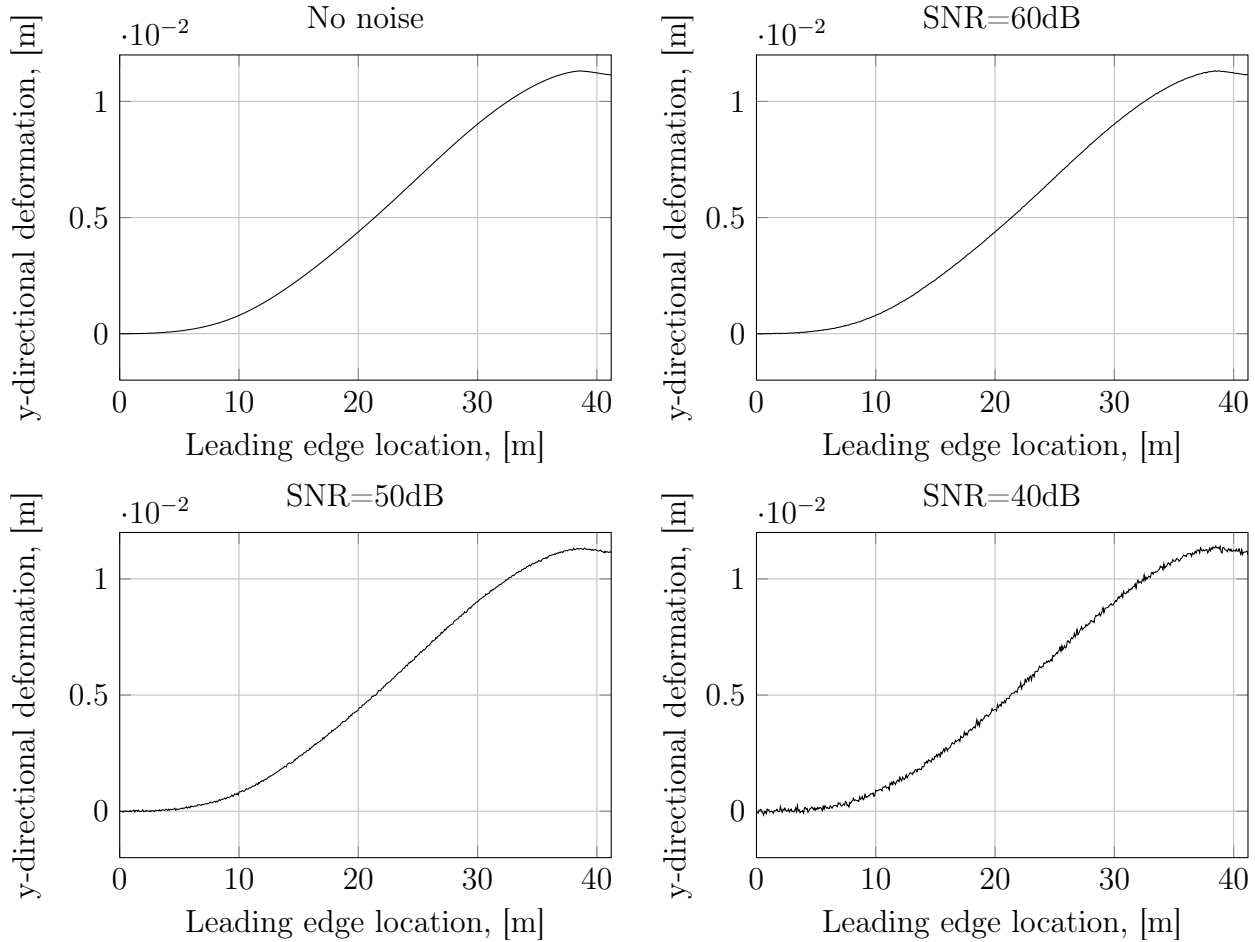


**Fig. 7.4:** Leading edge displacement signal for the first flapwise bending mode of the undamaged GE 1.5 XLE blade model with different noise settings.

### 7.4.1 Debonding of leading edge

15 leading edge debonding damage scenarios are introduced alternately in agreement with the description in Section 7.1, and subsequently the derived mode shape signals along the leading edge are investigated by use of one-dimensional Gaussian wavelet analysis. The obtained results are presented in Table 7.3, where it is seen how sensitive the first flapwise bending mode is towards the different leading edge debondings. Evidently, each individual debonding is localized and assessed acceptably when no noise occur in the mode shape signal. This is verified in Fig. 7.5 which displays the wavelet coefficients obtained from mode shape 1 without noise contamination. When noise is introduced, the wavelet peaks governed by the debondings in sections 1, 2 and 3 quickly become difficult to distinguish from the noise, and for SNR = 50 dB

**Table 7.3:** Damage identification for first flapwise bending mode of GE 1.5 XLE blade with debonding damages in leading edge. The number  $x \in [1; 3]$  and the signs  $\pm$  indicate the scores given in agreement with the classification established in Section 7.3.

Blade section	Debonding length [m]	Signal noise (SNR)			
		No noise	60 dB	50 dB	40 dB
1	0.5	2+	2+	3÷	3÷
	1.0	1+	2+	2÷	3÷
	2.0	1+	1+	2÷	2÷
2	0.5	2+	2÷	2÷	3÷
	1.0	2+	2+	2÷	2÷
	2.0	1+	1+	1÷	2÷
3	0.5	2+	2+	3÷	3÷
	1.0	2+	2+	2÷	2÷
	2.0	1+	1+	2+	2÷
4	0.5	1+	1+	1÷	2÷
	1.0	1+	1+	1+	2+
	2.0	1+	1+	1+	1+
5	0.5	1+	1+	2÷	2÷
	1.0	1+	1+	1+	2÷
	2.0	1+	1+	1+	2+

the debonding lengths cannot be assessed accurately in neither section 1 nor section 2. On the other hand, the sensitivities towards debondings in sections 4 and 5 are really high, and as seen in Table 7.3, acceptable localization is, as a minimum, obtained even for a noisy signal with  $\text{SNR} = 40$  dB.

There are several ways to improve the damage identification presented in Table 7.3, of which the two most obvious are section-divided analyses and employment of higher modes. When examining the plots in Fig. 7.5, it is evident that the former suggestion, i.e. conducting analyses for each section, will result in better results because peaks from other sections will be removed. Secondly, since sensitivity towards structural damage increases as higher modes are employed, see e.g. Fig. 5.6, it is also expectable that the other suggestion, i.e. employment of higher modes, will improve the damage identification. This is tested for the second flapwise bending mode depicted in Fig. 7.1b, and hereby the improvement-expectation has been validated. To exemplify this, Fig. 7.6 illustrates the wavelet coefficients for the second flapwise bending mode with a 2 m leading edge debonding in section 3, i.e. the debonding is centered at  $x = 20.6$  m, and an  $\text{SNR} = 40$  dB. Recalling the score given in Table 7.3 with the similar settings for the first flapwise bending mode, the improvement is clearly seen since employment of the second flapwise bending mode results in a score of 1+, i.e. unambiguously locate and accurately assessed. Generally, it is found that employment of the second flapwise bending mode facilitates acceptable damage identification for  $\text{SNR} = 30$  dB. Even further improvement can be expected for the high-frequency modes, but since these modes are typically not easily obtainable in in-service conditions, they will not be treated.

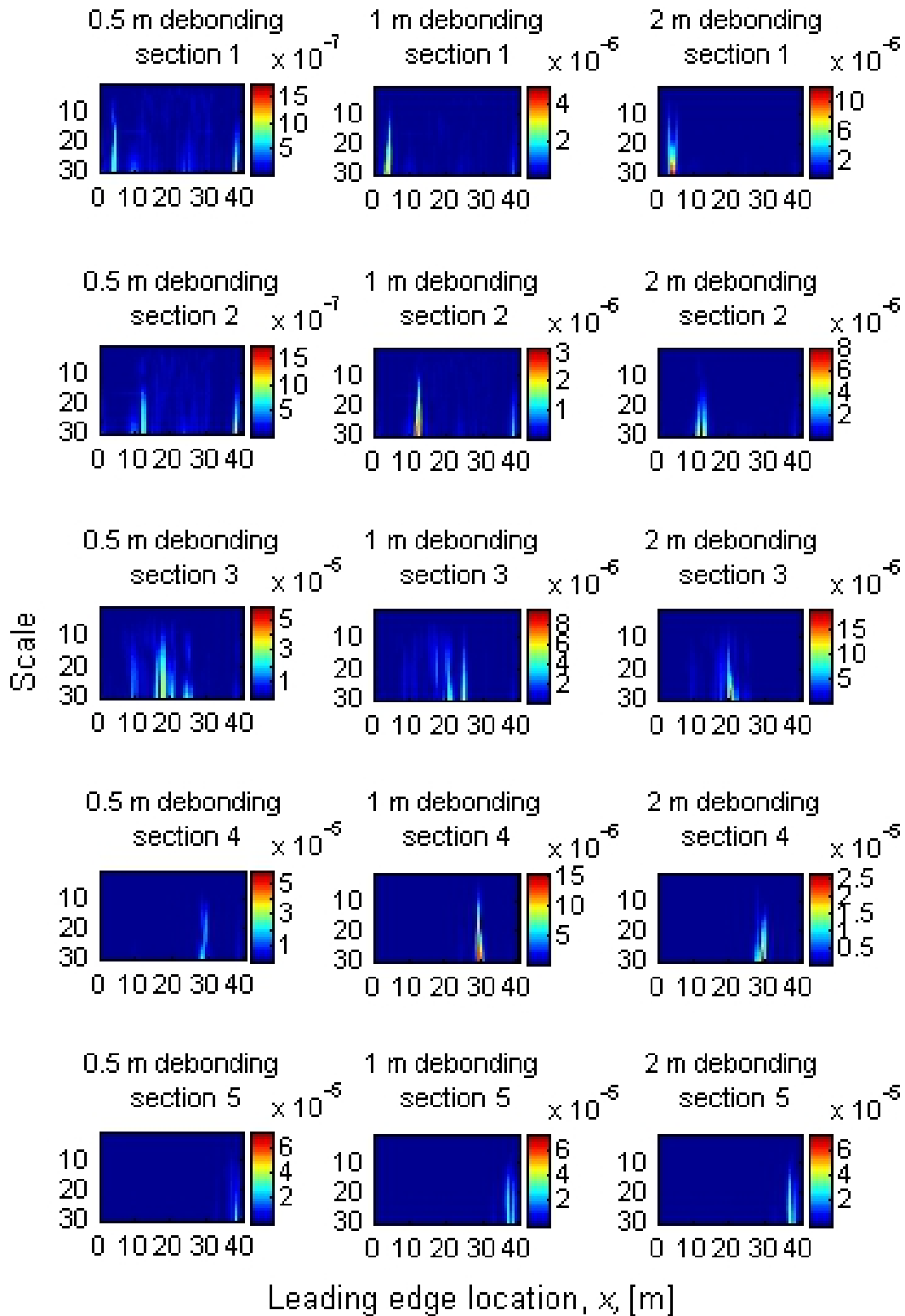


**Fig. 7.5:** Wavelet coefficients for first flapwise bending mode of GE 1.5 XLE blade with debondings in the leading edge centered at  $x_i[m] = \{4.1, 12.4, 20.6, 28.9, 37.1\}$ . No noise is added.

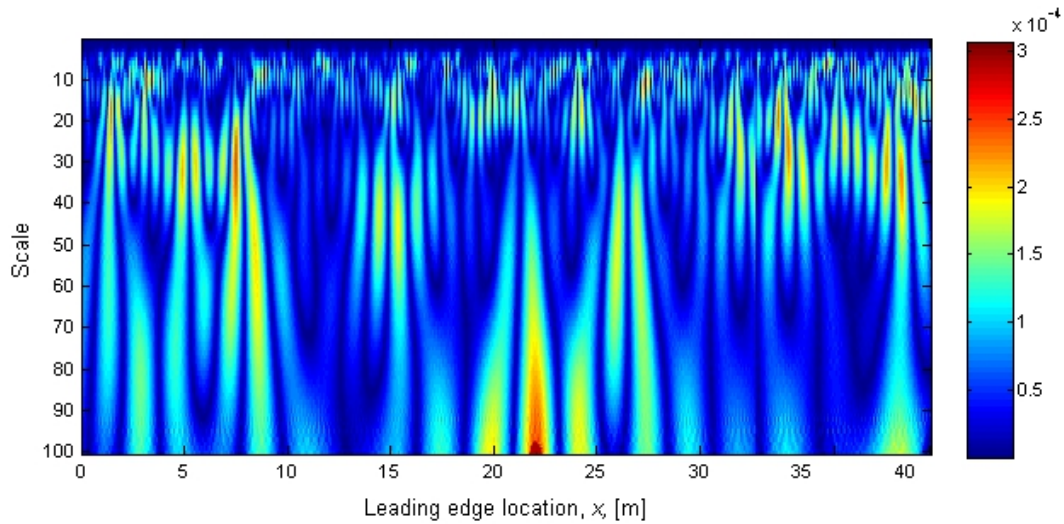


**Fig. 7.6:** Wavelet coefficients for the second flapwise bending mode of GE 1.5 XLE blade with 2 m leading edge debonding in section 3. Noise corresponding to SNR = 40 dB is added.

### 7.4.2 Debonding of trailing edge

In analogy to the analyses of debondings in the leading edge, 15 trailing edge debonding damage scenarios are investigated by use of one-dimensional Gaussian wavelet analysis of the mode

**Table 7.4:** Damage identification for first flapwise bending mode of GE 1.5 XLE blade with debonding damages in trailing edge. The number  $x \in [1; 3]$  and the signs  $\pm$  indicate the scores given in agreement with the classification established in Section 7.3.

Blade section	Debonding length [m]	Signal noise (SNR)			
		No noise	60 dB	50 dB	40 dB
1	0.5	3÷	3÷	3÷	3÷
	1.0	2+	2÷	3÷	3÷
	2.0	1+	1+	2÷	2÷
2	0.5	1+	2+	2+	3÷
	1.0	1+	2+	2+	3÷
	2.0	1+	1+	1+	2÷
3	0.5	1+	1+	2+	2÷
	1.0	1+	1+	1+	2÷
	2.0	1+	1+	1+	1÷
4	0.5	2+	2+	2÷	3÷
	1.0	1+	2+	2÷	3÷
	2.0	1+	1+	1+	2+
5	0.5	2+	2+	2÷	3÷
	1.0	1+	1+	2+	2÷
	2.0	1+	1+	2+	2÷



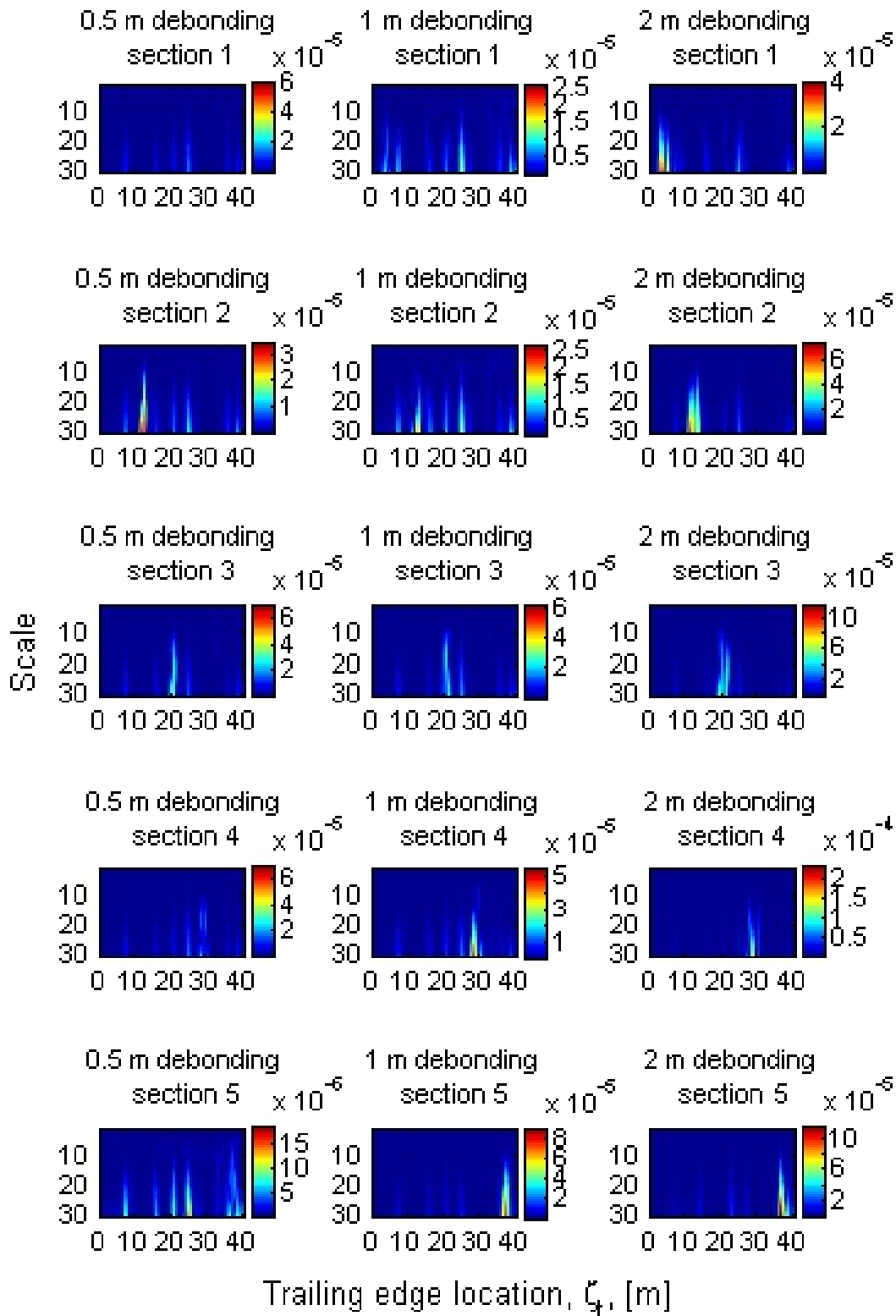


**Fig. 7.7:** Wavelet coefficients for first flapwise bending mode of GE 1.5 XLE blade with debondings in the trailing edge centered at  $\zeta_{i,i}[m] = \{4.3, 12.6, 20.9, 29.3, 37.5\}$ . No noise is added.

shape signal along the trailing edge. The obtained results for the first flapwise bending mode are presented in Table 7.4. Contrary to leading edge analysis findings, it is not possible to locate and assess all individual trailing edge debondings acceptably even when no noise occurs in the mode shape signal. This is seen in Fig. 7.7, where the wavelet coefficients obtained from mode shape 1 without noise contamination is presented.

Table 7.4 and Fig. 7.7 reveal that the 0.5 m trailing edge debonding in section 1 is not identified validly. However, as Fig. 7.7 implies, by conducting a section-divided analysis, the debonding will be accurately localized. Furthermore, employment of the second flapwise bending mode will also yield an improved localization compared to the original, see Fig. 7.8.

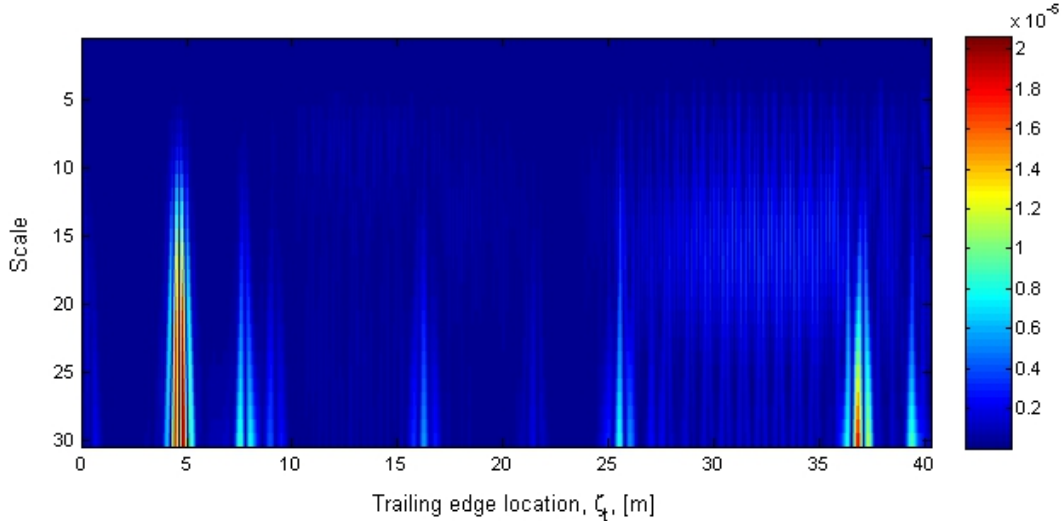


**Fig. 7.8:** Wavelet coefficients for the second flapwise bending mode of GE 1.5 XLE blade with 0.5 m trailing edge debonding in section 1. No noise is added.

When noise is introduced, the wavelet peaks governed by the debondings in sections 1 and 2 quickly become difficult to distinguish from the noise, just as it is the case for the leading edge debondings. On the other hand, the sensitivities towards debondings in sections 3, 4 and 5 are really high, and as seen in Table 7.3, especially trailing edge debondings in section 3 introduce significant discontinuities which can be localized acceptably in the noisy signal with  $\text{SNR} = 40$  dB. Generally, the damage identification can, like the leading edge debonding identification, be improved by either dividing the analyses into sections or by employing the higher modes.

### 7.4.3 Longitudinal crack

As described in Section 7.1, 15 longitudinal cracks are introduced alternately to the top surface of the GE 1.5 XLE blade. The damage identification analyses are conducted as two-dimensional wavelet analyses based on the measurement grid illustrated in Fig. 7.3. For information about two-dimensional wavelet analysis, the reader is referred to Appendix E which documents the wavelet, namely the two-dimensional Morlet wavelet, employed in the analyses in the present subsection. A wavelet parameter of  $k_0 = 6$  plus a scale of  $a = 7$  and  $a = 22$  for signals without and with noise, respectively, are utilized.

Table 7.5 presents the scores obtained in the damage identification analyses of the blade model introduced to the different longitudinal cracks. Evidently, the scores are generally worse

**Table 7.5:** Damage identification for first flapwise bending mode of GE 1.5 XLE blade with longitudinal cracks in the top surface. The number  $x \in [1; 3]$  and the signs  $\pm$  indicate the scores given in agreement with the classification established in Section 7.3.

Blade section	Crack length [m]	Signal noise (SNR)			
		No noise	60 dB	50 dB	40 dB
1	0.5	3÷	3÷	3÷	3÷
	1.0	2+	2÷	2÷	3÷
	2.0	1÷	1÷	2÷	2÷
2	0.5	2+	2÷	2÷	3÷
	1.0	2+	2+	2+	3÷
	2.0	1+	1+	1+	2÷
3	0.5	2+	2÷	2÷	3÷
	1.0	2÷	2÷	2÷	2÷
	2.0	1+	1+	1÷	2÷
4	0.5	1÷	1÷	2÷	2÷
	1.0	1+	1+	2÷	2÷
	2.0	1+	1+	2+	2÷
5	0.5	3÷	3÷	3÷	3÷
	1.0	1÷	1÷	3÷	3÷
	2.0	1÷	1÷	2÷	3÷

than those obtained for the debonding damage scenarios, and especially an accurate assessment is difficult to obtain. One major reason for this is the influence of the shear web. By close inspection of the plots in Fig. 7.9, it can be seen that a disturbing pattern of wavelet coefficient peaks in non-damaged areas is derived consistently for all analyses. As visualized in Fig. 7.10, these patterned peaks arise as a consequence of the contact between the top blade surface and the shear web, hence the presence of the shear web composes an issue in wavelet analysis for identification of damages located on the blade surfaces.

Since the adverse effects of the shear web will occur consistently, it is obvious to suggest that these effects are eliminated by, e.g., subtracting wavelet coefficients derived from an undamaged model from the wavelet coefficients derived from a damaged model. However, this approach is not applicable in general because it requires complete consistency between the undamaged areas of the pre- and post-damage analyses, which cannot be expected during in-service conditions. Consequently, the only way of reducing the impact of the adverse shear web effects is to ensure that the wavelet coefficients governed by the structural damage are significantly higher than those governed by the shear web. For all other sections than the second and third, in which the largest wavelet coefficient peaks governed by the shear web are located, the adverse shear web effects can to some extent be concealed by conducting section-divided analyses. It has also been examined how the employment of higher modes influences the shear web effects, and here it is generally found for the bending modes that the shear web effects are predominant, thus employment of higher bending modes does not facilitate clearer distinction between the wavelet coefficient peaks governed by the structural damage and those governed by the shear

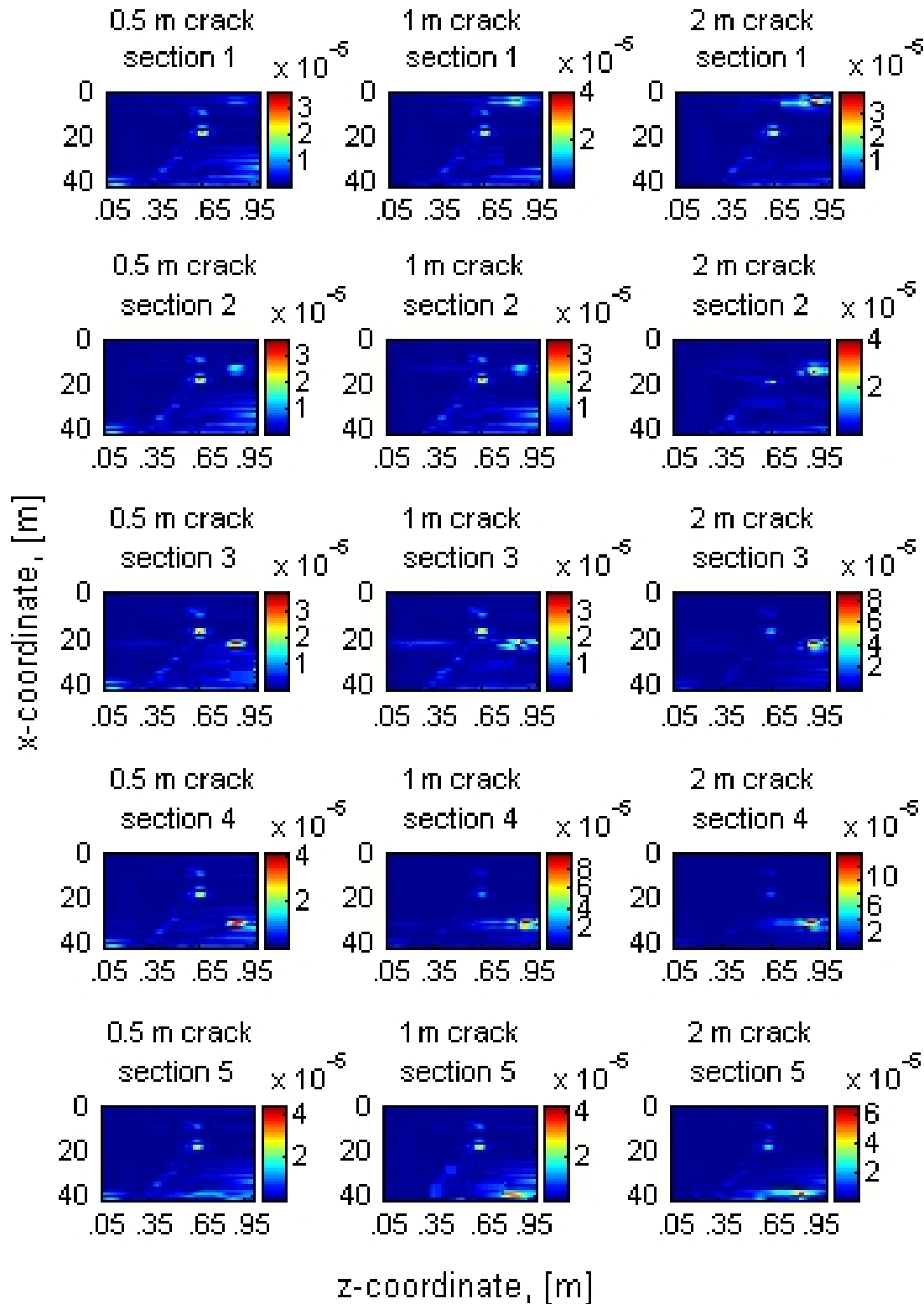


**Fig. 7.9:** Wavelet coefficients for first flapwise bending mode of GE 1.5 XLE blade with longitudinal cracks in the top surface centered at  $(z, x_i)[m] = (0.88, \{4.1, 12.4, 20.6, 28.9, 37.1\})$ . No noise is added.

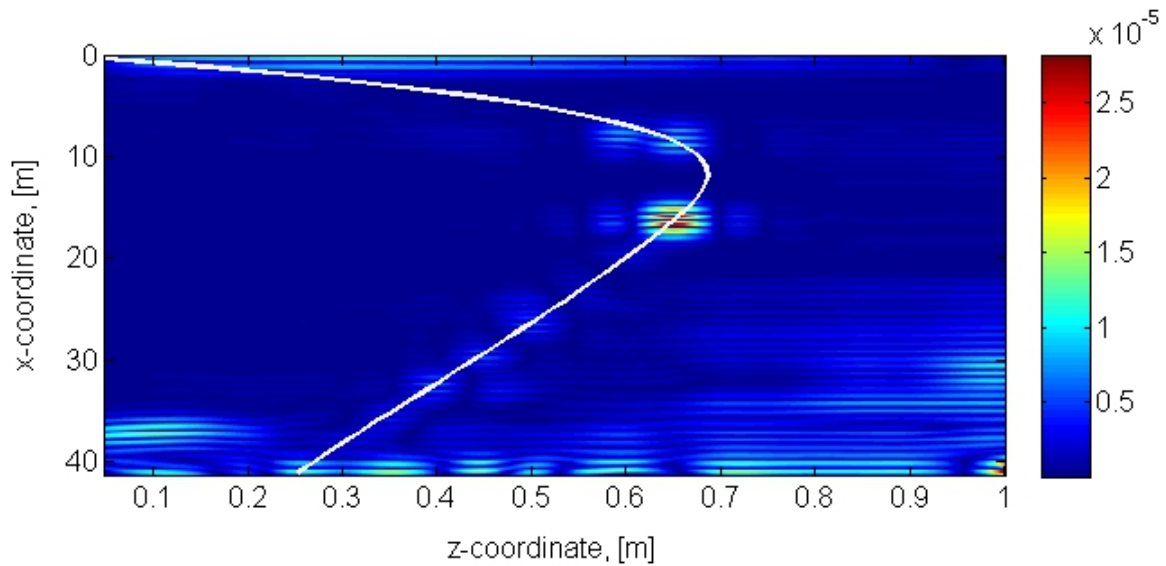


**Fig. 7.10:** Wavelet coefficients for undamaged GE 1.5 XLE blade model with specification of shear web location. No noise is added.

web. For the twisting modes, however, it is found that these yield improved identification results since the wavelet coefficients in the damaged area are significantly higher than those in the undamaged area. In Fig. 7.11, this is illustrated for the first twisting mode with a 1 m longitudinal crack in section 2. When comparing these findings with the corresponding results for the first flapwise bending mode, see Fig. 7.9, the improvement is evident, and employment of the twisting mode yields unambiguous localization and accurate assessment, i.e. a score of 1+.

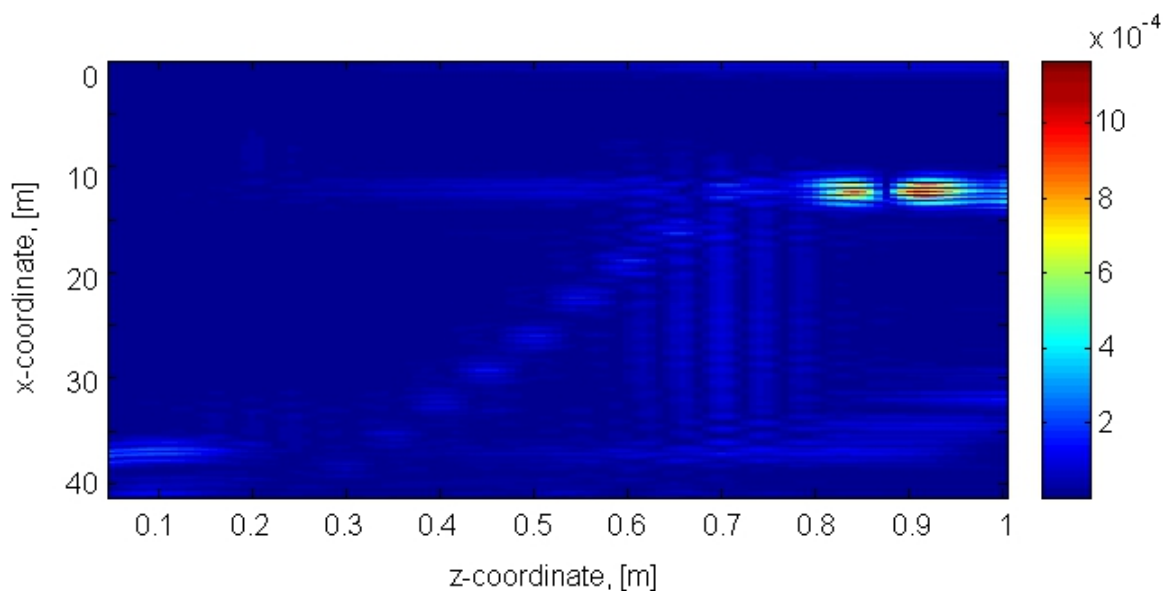


**Fig. 7.11:** Wavelet coefficients for the first twisting mode of GE 1.5 XLE blade with 1 m longitudinal crack in section 2. No noise is added.

#### 7.4.4 Transverse crack

Five longitudinal cracks are introduced alternately to the top surface of the GE 1.5 XLE blade in agreement with the descriptions in Section 7.1. The damage identification analyses are conducted as two-dimensional wavelet analyses based on the measurement grid illustrated in Fig. 7.3. In analogy to the analyses conducted in the previous section, the two-dimensional Morlet wavelet is employed with a wavelet parameter of  $k_0 = 6$  plus a scale of  $a = 7$  and  $a = 22$  for signals without and with noise, respectively. The analysis results are presented in Table 7.6, and here it is seen that the wavelet analysis method succeeds in localizing and assessing all five transverse cracks for both the noise-uncontaminated signal and the SNR = 60 dB-signal of the first flapwise bending mode. As it can be deduced from the plots in Fig. 7.12, the adverse effects of the shear web, see e.g. Fig. 7.10, are also present. However, since the transverse cracks yields very large wavelet coefficients in the damaged area, the adverse effects are not as dominating as it is the case for many of the longitudinal cracks, see e.g. Fig. 7.9.

**Table 7.6:** Damage identification for first flapwise bending mode of GE 1.5 XLE blade with transverse cracks in the top surface. The number  $x \in [1; 3]$  and the signs  $\pm$  indicate the scores given in agreement with the classification established in Section 7.3.

Blade section	Crack length [m]	Signal noise (SNR)			
		No noise	60 dB	50 dB	40 dB
1	0.05	2+	2+	3÷	3÷
2	0.05	1+	1+	2+	3÷
3	0.05	1+	1+	1+	2÷
4	0.05	1+	1+	1+	2÷
5	0.05	1+	2+	2+	3÷

The plots in Fig. 7.12 imply that the blade is very sensitive towards transverse cracks, as it is seen that all cracks are localized acceptably, hence the scores given in Table 7.6. The scores are additionally improved as the higher flapwise bending modes are employed, as exemplified in Fig. 7.13a which illustrates the wavelet coefficients for the second flapwise bending mode of the blade with a 0.5 m longitudinal crack in section 1. However, contrary to the findings for the longitudinal cracks, treated in previous subsection, the employment of twisting modes does not improve the damage identification of transverse cracks because the adverse effects of the shear web are dominant. In Fig. 7.13b, this is illustrated for the first twisting mode which represents the general tendency of the twisting modes.

#### 7.4.5 Summary of single-damage identification analyses

In the present section, damage identification analyses have been conducted for the first mode of the GE 1.5 XLE blade model introduced, alternately, to leading and trailing edge debondings plus longitudinal and transverse cracks on the top surface of the blade. In Tables 7.3 - 7.6, the analysis results, in the form of scores for damage localization and assessment, are presented in agreement with the classification system described in Section 7.3. The general tendency is that all the damages are localized and assessed acceptably for signals without noise and for signals

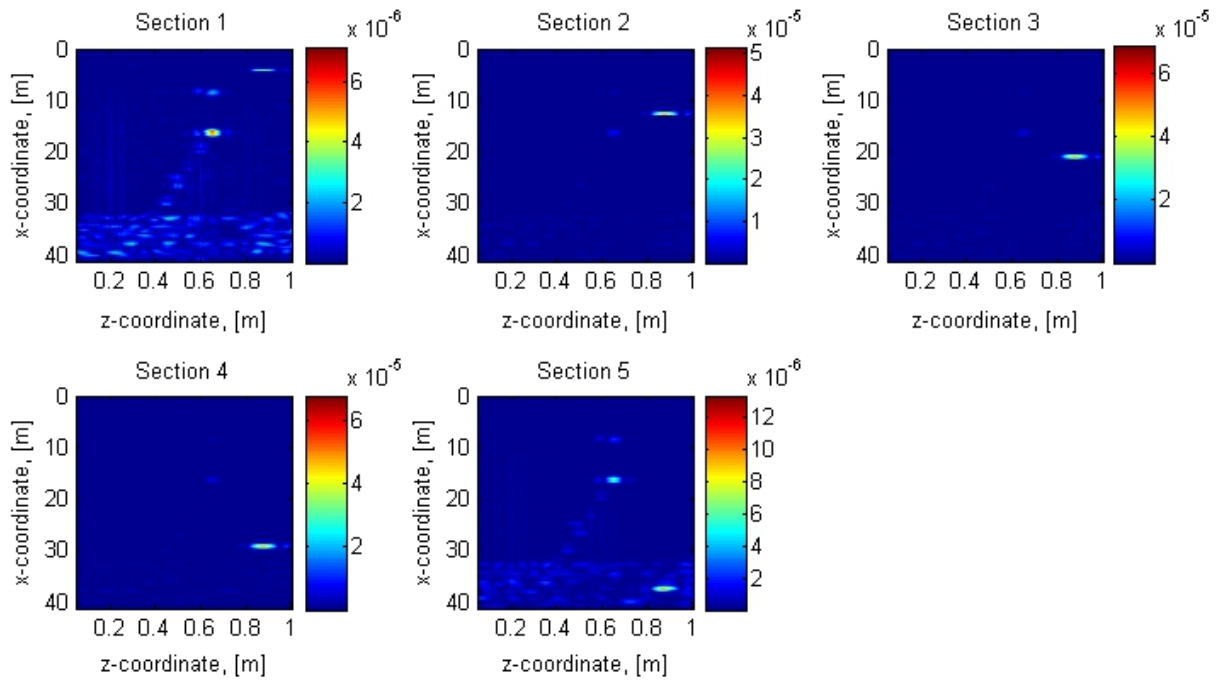


**Fig. 7.12:** Wavelet coefficients for first flapwise bending mode of GE 1.5 XLE blade with transverse cracks in the top surface centered at  $(z, x_i)[m] = (0.88, \{4.1, 12.4, 20.6, 28.9, 37.1\})$ . No noise is added.

with a small amount of noise, corresponding to  $\text{SNR} = 60$  dB. When more noise is introduced, i.e.  $\text{SNR} = 50$  dB, unambiguous localization and accurate assessment becomes challenging, and for a noisy signal,  $\text{SNR} = 40$  dB, the applicable identification is primarily obtained as ambiguous localization in blade sections 3 and 4. Generally, introduction of damages in these

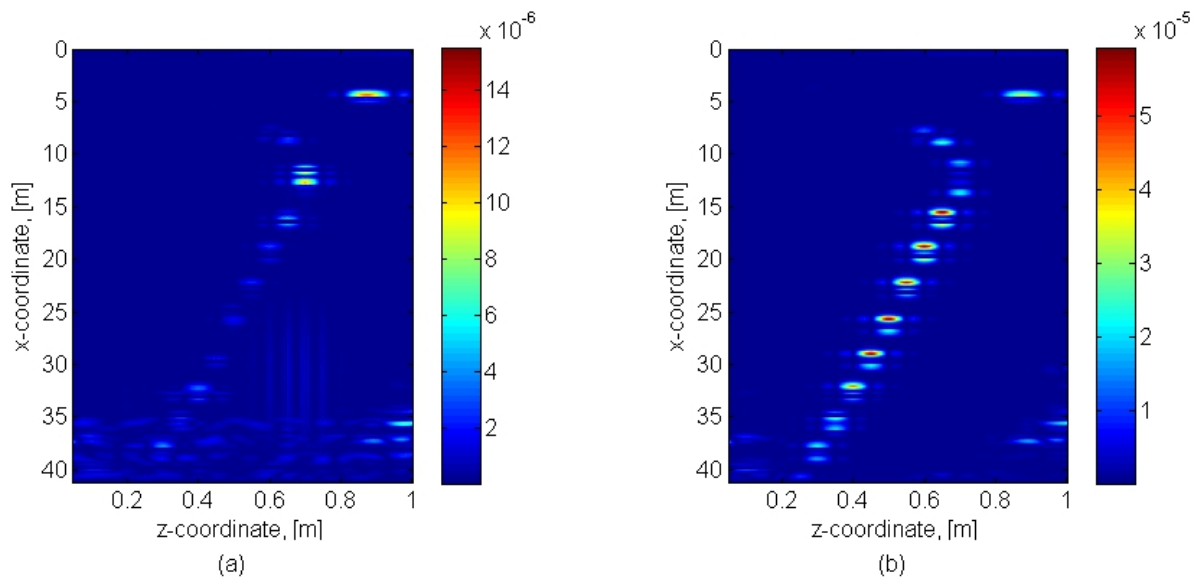


**Fig. 7.13:** Wavelet coefficients for different modes of GE 1.5 XLE blade with 1 m longitudinal crack in section 1. No noise is added. (a) Second flapwise bending mode. (b) First twisting mode.

specific sections result in the most pronounced wavelet coefficient peaks in the damaged area.

Regarding the influence of damage types, it is found that identification of the longitudinal cracks along the top blade surface is impeded by adverse effects of the shear web, see e.g. Fig. 7.10. These effects can, however, be concealed by employing the twisting modes of the blade, as shown in Fig. 7.11, which generally improve the damage identification for this particular damage type. For the other crack type, i.e. the transverse crack across the top blade surface, it is found that the shear web effects are of less significance when employing the first flapwise bending mode, thus acceptable identification of the transverse crack can be obtained on the basis of this mode shape. Indeed, employment of higher flapwise bending modes yield even better damage identification, see e.g. Fig. 7.13a, but it is found that the use of twisting modes deteriorates the identification as the wavelet coefficient peaks governed by the cracks are surpassed by the wavelet coefficient peaks governed by the shear web effects, see e.g. Fig. 7.13b. For the debonding damages, it is generally found that employment of the higher modes, both bending and twisting, yields significantly improved identification of the debondings. Consequently, it can be concluded that all the examined damage types can be identified acceptably for noise signals with SNR = 40 dB if higher modes, e.g. second flapwise bending and first twisting, are employed along with mode 1.

## 7.5 Multi-damage identification analyses

To further examine the robustness and general applicability of the modal and wavelet analysis-based damage identification method, the following three multi-damage scenarios are analyzed;

- 1 m longitudinal crack in section 4 and 0.05 m transverse crack in section 2.
- 2 m trailing edge debonding in section 3 and 0.05 m transverse crack in section 3.
- 1 m leading edge debonding in section 1, 2 m leading edge debonding in section 5 and 0.5 m trailing edge debonding in section 5.

The multi-damage scenarios presented in the listing above are chosen, partially, because they compose a realistic mixture of damages, and partially because the combination of damages in each scenario facilitates inspection of potential adverse, inherent effects from one damage to the wavelet analysis of another damage.

### 7.5.1 Longitudinal and transverse cracks

As described introductory in the present section, a 0.05 m transverse crack is introduced in section 2 along with a 1 m longitudinal crack in section 4. In particular, the transverse crack is centered at  $(z,x)[m] = (0.88,12.4)$ , while the longitudinal crack is centered at  $(z,x)[m] = (0.88,28.9)$ . With these damages, the wavelet analysis coefficients plotted in Fig. 7.14 are obtained. Evidently, an unambiguous localization is deduced, and through a more thorough inspection, it is also found that an accurate assessment is obtained for both damages.

A brief study of the influence of noise contamination has been performed, and here it is found that the influence for this multi-damage scenario generally resembles the tendency deduced for the single-damage analyses of the longitudinal and transverse cracks, see e.g. Tables 7.5 and 7.6.



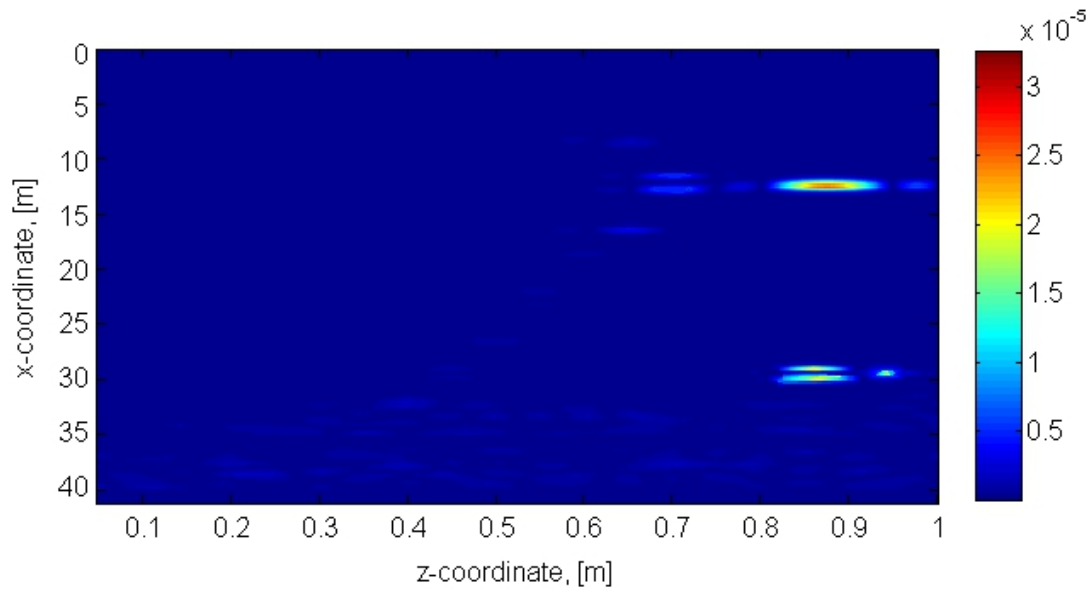


**Fig. 7.14:** Wavelet coefficients for first flapwise bending mode of GE 1.5 XLE blade with a 0.05 m transverse crack centered in section 2 at  $(z,x)[m] = (0.88,12.4)$  and a 1 m longitudinal crack centered in section 4 at  $(z,x)[m] = (0.88,28.9)$ .

### 7.5.2 Trailing edge debonding and transverse crack

A 2 m trailing edge debonding, centered at  $\zeta_t = 20.9$  m, and a 0.05 m transverse crack, centered at  $(z,x)[m] = (0.88,20.6)$ , are introduced in section 3. This damage scenario is examined by a one-dimensional wavelet analysis along the trailing edge combined with a two-dimensional wavelet analysis in the top blade surface grid, thus two independent plots are obtained as shown in Fig. 7.15.

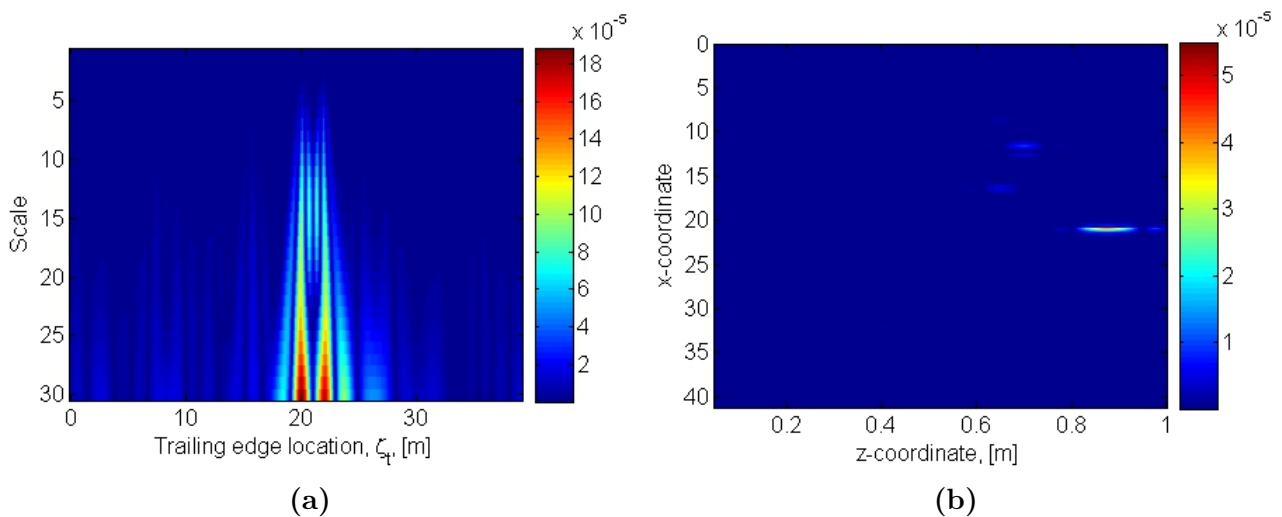


**Fig. 7.15:** Wavelet coefficients for first flapwise bending mode of GE 1.5 XLE blade with a 2 m trailing edge debonding centered in section 3 at  $\zeta_t = 20.9$  m plus a 0.05 m transverse crack centered in section 3 at  $(z,x)[m] = (0.88,20.6)$ . (a) One-dimensional wavelet plot for trailing edge. (b) Two-dimensional wavelet plot for top blade surface grid.

The plot in Fig. 7.15a clearly shows that an unambiguous localization and accurate assessment is obtained for the trailing edge debonding. Regarding the transverse crack, it is seen in Fig. 7.15b that the damage is localized unambiguously. Via a close-up inspection it is also found that the damage is assessed accurately.

In analogy to the procedure in Subsection 7.5.1, a brief study of the influence of noise contamination has been conducted. Hereby, it is found that the influence for the multi-damage scenario with a trailing edge debonding and a transverse crack resembles the tendency deduced for the single-damage analyses of the trailing edge debondings and transverse cracks, see e.g. Tables 7.4 and 7.6.

### 7.5.3 Leading and trailing edge debondings

In this third and last multi-damage analysis, three different debondings are introduced. In section 1, a 1 m leading edge debonding is introduced, centered at  $x = 4.1$  m, and additionally, a 2 m leading edge debonding plus a 0.5 m trailing edge debonding are introduced in section 5, centered at  $x = 37.1$  m and  $\zeta_t = 37.5$  m, respectively. This damage scenario is examined by one-dimensional wavelet analyses along the leading edge and the trailing edge, hence resulting in the two independent plots presented in Fig. 7.16.

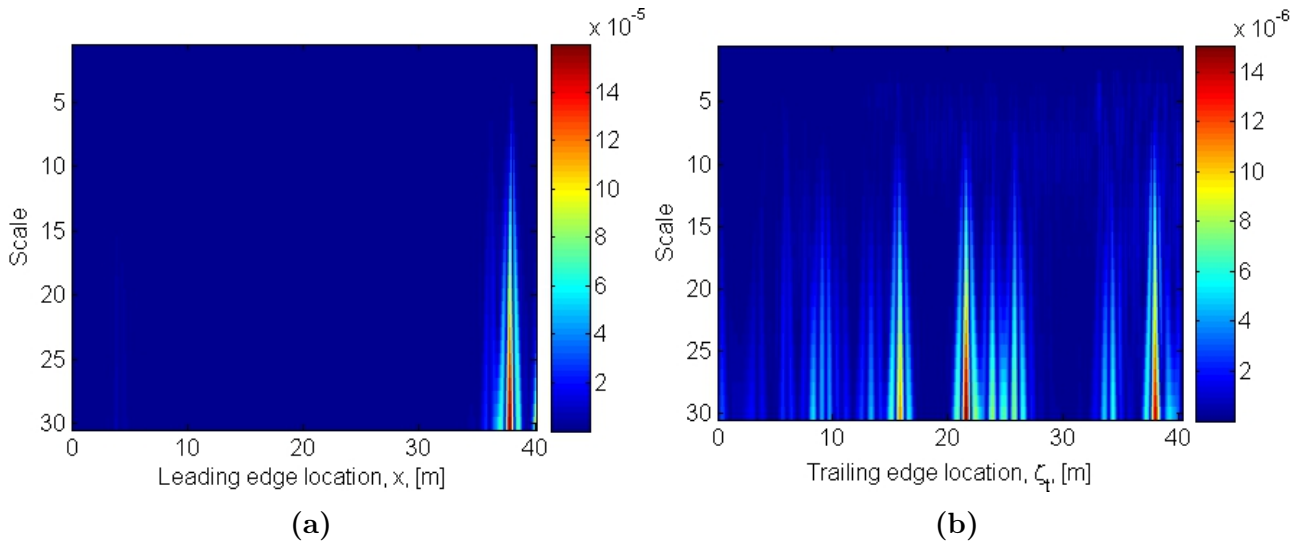


**Fig. 7.16:** Wavelet coefficients for first flapwise bending mode of GE 1.5 XLE blade with a 1 m leading edge debonding centered in section 1 at  $x = 4.1$  m, a 2 m leading edge debonding centered in section 5 at  $x = 37.1$  m plus a 0.5 m trailing edge debonding centered in section 5 at  $\zeta_t = 37.5$  m. (a) One-dimensional wavelet plot for leading edge. (b) One-dimensional wavelet plot for trailing edge.

Fig. 7.16a shows that the 2 m leading edge debonding in section 5 is identified, i.e. localized and assessed, acceptably. By close inspection of the plot, it can be seen that the 1 m leading edge debonding in section 1 excites local wavelet coefficient peaks, which are located and confined in the damaged area, thus acceptable identification is also obtained for this damage. Regarding the 0.5 m trailing edge debonding, Fig. 7.16b illustrates that the damage, in agreement with the results presented in Table 7.4 for the single-damage scenario, is ambiguously localized but

accurately assessed. This suggests that the leading edge debondings have not triggered adverse effects in the wavelet analysis of the trailing edge debonding.

As done for the two other multi-damage analyses, see e.g. Subsections 7.5.1 and 7.5.2, a brief study of the influence of noise contamination has been conducted. It is found that the influence for the multi-damage scenario with two leading edge debondings and one trailing edge debonding resembles the tendency deduced for the single-damage analyses of the debondings, see e.g. Tables 7.3 and 7.4.

## 7.6 Summary

The present chapter deals with modal and wavelet analysis-based damage identification for a blade from a full-scale wind turbine, namely the GE 1.5 XLE wind turbine. As described in Section 7.1, the identification analyses have been conducted for leading and trailing edge debondings plus longitudinal and transverse cracks in the top blade surface. These specific damages have been chosen because they generally compose the most severe and critical damages in wind turbine blades [9].

The wavelet analyses are based on post-damage mode shapes which are derived through free-vibration finite element analyses. In Section 7.2, it is described how the measurement points, which capture the modal displacements composing the mode shapes, are placed on the blade model. It has been chosen to place measurement points along the leading and trailing edge plus in a grid on the top blade surface, as shown in Fig. 7.3. This facilitates one-dimensional wavelet analyses for the debondings and two-dimensional wavelet analyses for the cracks.

In order to evaluate the quality of the damage identification in a consistent way, a classification system has been introduced in Section 7.3. The system divides the damage localization into three scores, namely 1, 2 and 3, where 1 represents an unambiguous localization, 2 represents an ambiguous, but still acceptable, localization, and 3 represents an invalid localization. For the damage assessment, the score + is given for assessments which lie in an interval of  $\pm 20\%$  of the actual damage length, while  $\div$  implies that this interval demand is not fulfilled.

Based on the classification system, the single-damage identification analyses have been carried out in Section 7.4. As summarized in Subsection 7.4.5, it is found through single-damage analyses that the general tendency is acceptable localization and assessment for all the damages when no noise or a little amount of noise, corresponding to a  $\text{SNR} = 60$  dB, is added to the signal of the first mode shape. When more noise is introduced, i.e.  $\text{SNR} = 50$  dB, unambiguous localization and accurate assessment becomes challenging, and for a noisy signal,  $\text{SNR} = 40$  dB, the applicable identification is primarily obtained as ambiguous localization in blade sections 3 and 4. The damage identification is generally improved significantly when higher modes are employed. This is due to the fact that the sensitivity towards structural abnormalities, such as debondings and cracks, is increased in the higher modes. However, for the transverse cracks it is found that only the flapwise bending modes are suitable for damage identification, since the employment of, e.g., twisting modes yields predominant wavelet coefficient peaks along the joint between the shear web and the top blade surface. Consequently, it can be concluded that all the examined damage types can be identified acceptably for noisy signals with  $\text{SNR} = 40$  dB if higher modes, e.g. second flapwise bending and first twisting, are employed.

The analyses conducted in Section 7.5 imply that the modal and wavelet analysis-based damage identification method is applicable also for multi-damage scenarios, since acceptable identification is obtained for the three analyzed multi-damage scenarios. Furthermore, a brief

study of the influence of noise contamination has been performed, and here it is found that the tendency for multi-damage scenarios generally resembles the tendency for the single-damage scenarios. Therefore, it can be concluded that both single- and multi-damage scenarios can be identified acceptably for noisy signals with  $\text{SNR} = 40$  dB if higher modes are employed.

---

# CONCLUSION

---

The main scope of the present report is to conduct level 1, 2 and 3 damage identification analyses, i.e. detection, localization and assessment, of wind turbine blades. In order to ensure that the analyses are carried out validly and that they resemble realistic conditions, an extensive literature review of general methods available for damage identification is presented along with a description of typical structural damages in wind turbine blades. The review findings and the damage descriptions are, as an addition to the use in this report, also summed up in a paper submitted to the 10th International Conference on Damage Assessment of Structures (DAMAS) 2013.

In the literature review of general methods available for damage identification, three methods, namely temperature-, noise- and vibration-based, are described and subsequently compared. On the basis of these comparisons, it is chosen to employ a vibration-based method, in the form of modal analysis, because it is found that the two other methods have more critical shortcomings than the vibration-based, now referred to as modal analysis-based. Furthermore, the modal analysis-based method is appealing because studies imply that only the high-frequency modes are applicable when conducting damage identification based on modal parameters. Hence, this facilitates a possible challenging of this common assumption.

Regarding damage types, the presented descriptions conclude that edge debondings, longitudinal cracks and transverse cracks are the most critical and severe, because these damage types typically necessitate structural repairs. Consequently, only these three damage types are treated in the analyses presented in this report.

With modal analysis as the general approach, the damage identification must be conducted by use of a specific method which utilizes some of the modal parameters, i.e. eigenfrequencies, mode shapes and modal damping ratios, as damage indicators. Both the eigenfrequencies and the damping ratios have proven to be inconvenient, because they, respectively, are too insensitive towards structural damages and show ambiguous changes when damage is introduced. Therefore, three methods utilizing mode shapes or their derivatives have been tested on the basis of numerically derived pre- and post-damage mode shapes of a cantilevered rectangular shell tube. The first method is based on the coordinate modal assurance criteria (COMAC), which seeks to locate the differences between pre- and post-damage mode shapes. The second method applies the mode shape curvatures (MSCs) of the undamaged and damaged model, respectively, and compare these directly. The motivation behind applying the MSCs instead of the original mode shapes becomes clear when recalling the Euler-Bernoulli beam theory, which states that the curvature is inversely proportional to the flexural stiffness, implying that a reduction of stiffness associated with damage will lead to an increase in curvature. The third and last examined method is wavelet analysis in which damage-governed discontinuities in the post-damage mode shape signals are searched for via wavelet transformations. Through analyses of the aforementioned shell tube, the three methods have been tested, and hereby it is found that the wavelet analysis-based approach yields the best results for damage detection, localization and assessment and is more robust towards noise than the other methods. Consequently, the wavelet analysis-based method is chosen.

To examine the general applicability of the modal and wavelet analysis-based damage iden-

tification method, blades from a residential-sized wind turbine, namely the Whisper 500, and a full-scale wind turbine, namely the GE 1.5 XLE, are treated. First, level 1, 2 and 3 damage identification is conducted for the Whisper 500 blade introduced to longitudinal cracks of realistic sizes and depths. The mode shapes are derived both experimentally and numerically, and since the different results show strong correlation, the experimental and numerical findings show the same tendencies for changes in mode shapes and eigenfrequencies; introduction of longitudinal cracks mostly influences the modal parameters of the higher modes, especially the twisting modes, but through wavelet analysis even the first bending mode shape yields valid and useful damage detection, localization and assessment. This strongly emphasizes the applicability of wavelet analysis for damage identification of real-life structures, for which it is desirable if the low-frequency modes can be employed because these are easy to access. However, the analyses of the Whisper 500 blade imply that the wavelet analysis-based method, like all other mode shape-based methods, has an inherent shortcoming regarding the amount and placement of measurement points; the distance between the measurement points must be smaller than the damage sizes if these are to be localized unambiguously and assessed accurately. It is noticed that a paper containing the initial level 1 damage identification for the Whisper 500 blade is submitted to the 10th International Conference on Damage Assessment of Structures (DAMAS) 2013.

Damage identification analyses of the GE 1.5 XLE wind turbine blade are conducted for derived mode shapes of a numerical blade model, to which different damage types, in the form of longitudinal and transverse cracks plus edge debondings, are introduced both alternately and simultaneously. To further challenge the robustness and general applicability of the method, Gaussian noise is added in order to simulate typical experimental findings. For the single-damage scenarios, it is found that employment of the first mode shape facilitates acceptable damage identification for signals without noise and for signals with a small amount of noise, corresponding to  $\text{SNR} = 60$  dB. When more noise is introduced, i.e.  $\text{SNR} = 50$  dB, unambiguous localization and accurate assessment becomes challenging, and for a noisy signal,  $\text{SNR} = 40$  dB, the damages are only identified acceptably when introduced in some of the blade sections. This identification is, however, ambiguous, thus clear damage identification for noisy signals is generally not obtained by employment of the first mode shape, i.e. the first flapwise bending mode shape. Studies in this report suggest that employment of higher mode shapes, e.g. the second flapwise and the first twisting, significantly improves the damage identification and robustness towards noise. By conducting multi-damage analyses, it is found that the wavelet analysis-based method is applicable also for multi-damage scenarios, since acceptable identification is obtained for three analyzed multi-damage scenarios. Furthermore, a brief study of the influence of noise contamination has been performed, and here it is found that the tendency for multi-damage scenarios generally resembles the tendency for the single-damage scenarios. Thus, it can be concluded that both single- and multi-damage scenarios can be identified acceptably for noisy signals if higher modes are employed.

To summarize, the present report focuses on establishing a general method for damage identification for wind turbine blades. The results and findings in the report strongly suggest that modal and wavelet analysis-based damage identification has the potential to be applied for operating wind turbines. However, in order to reach this state of applicability, it is necessary to comprehensively examine specific aspects, such as instrumentation and the influence of actual dynamic response during operational condition.

---

# Bibliography

---

- [1] Wind Energy, The Facts, Operation and Maintenance Costs of Wind Generated Power.  
*<http://www.wind-energy-the-facts.org/en/part-3-economics-of-wind-power/chapter-1-cost-of-on-land-wind-power/operation-and-maintenance-costs-of-wind-generated-power.html>*. Accessed 12.11.2012.
- [2] Anders Rytter.  
*Vibration Based Inspection of Civil Engineering Structures*. Ph.D. Thesis, Aalborg University, Denmark, 1993.
- [3] Saferenvironment, Wind Energy - Renewable energy harnesses natural wind power - Effective answer for emission problem towards cleaner, safer and greener environment.  
*<http://saferenvironment.wordpress.com/2008/11/03/wind-energy-renewable-energy-harnesses-natural-wind-power-%E2%80%93-effective-answer-for-emission-problem-towards-cleaner-safer-and-greener-environment/>*. Accessed 18.01.2013.
- [4] NewEn Austria, Wind Turbines.  
*<http://www.newen.com.au/Wind-Facts/Wind-Facts/>* Accessed 05.01.2013.
- [5] A.G. Dutton.  
*Thermoelastic Stress Measurement and Acoustic Emission Monitoring in Wind Turbine Blade Testing*. Proceedings, European Wind Energy Conference, 2004.
- [6] P.A. Joosse, M.J. Blanch, A.G. Dutton, D.A. Kouroussis, T.P. Philippidis & P.S. Vionis.  
*Acoustic Emission Monitoring of Small Wind Turbine Blades*. Journal of Solar Energy Engineering, 124, 2002.
- [7] S.N. Ganeriwala, Jun Yang & Mark Richardson.  
*Using Modal Analysis for Detecting Cracks in Wind Turbine Blades*. Sound and Vibration Magazine, 10, 2011.
- [8] M.M. Khan, M.T. Iqbal & F. Khan.  
*Reliability and condition monitoring of a wind turbine*. Proceedings, 18th Annual Canadian Conference on Electrical and Computer Engineering, 2005.
- [9] Sabbah Ataya & M.M.Z. Ahmed.  
*Forms of discontinuities in 100 KW and 300 KW Wind Turbine Blades*. Proceedings, 10th World Wind Energy Conference & Renewable Energy Exhibition, 2011.
- [10] Basin Electric Power Cooperative, Wilton wind blade damage.  
*<http://basinelectric.wordpress.com/2009/06/04/cause-still-unknown-for-broken-blade-on-wind-turbine/wilton-wind-blade-damage1/>*. Accessed 05.01.2013.

- [11] Bladena, Blade Enabler.  
*Bladena Presentation, Technical, November, 2012, Find Mølholt Jensen.* (See enclosed DVD).
- [12] F.M. Larsen & Troels Sorensen.  
*New Lightning Qualification Test Procedure for Large Wind Turbine Blades.* Proceedings, International Conference on Lightning and Static Electricity, 2003.
- [13] N.P. Avdelidis, D.P. Almond, C. Ibarra-Castanedo, A. Bendada, S. Kenny & X. Maldague.  
*Structural integrity assessment of materials by thermography.* Proceedings, Conference on Damage in Composite Materials CDCM, 2006.
- [14] R.D. Cook, D.S. Malkus, M.E. Plesha & R.J. Witt.  
*Concepts and Applications of Finite Element Analysis.* 4th ed., John Wiley & Sons, 2002.
- [15] C.C. Ciang, J.R. Lee & H.J. Bang.  
*Structural health monitoring for a wind turbine system: a review of damage detection methods.* Journal of Measurement Science and Technology, 19, 2008.
- [16] A.G. Dutton, L.J.J. Speet, D.R.V. van Delft, A.H. Yaghi, G.M. Smith, W.J. Morris & L. Boswell.  
*Damage detection and stress measurement in composite wind turbine blades.* Proceedings, European Wind Energy Association Conference, 1994.
- [17] F. Hahn, C.W. Kensche, R.J.H. Paynter, A.G. Dutton, C. Kildegaard & J. Kosgaard.  
*Design, Fatigue Test and NDE of a Sectional Wind Turbine Rotor Blade.* Journal of Thermoplastic Composite Materials, 15, 2002.
- [18] IEC 61400-1.  
*Wind turbines - Part 1: Design requirements,* 3rd ed., 2005.
- [19] IEC/TS 61400-23.  
*Wind turbine generator systems - Part 23: Full-scale structural testing of rotor blades,* 1st ed., 2001.
- [20] A.A. Anastassopoulos, D.A. Kouroussis, V.N. Nikolaidis, A. Proust, A.G. Dutton, M.J. Blanch, L.E. Jones, P. Vionis, D.J. Lekou, D.R.V. van Delft, P.A. Joosse, T.P. Philippidis, T. Kossivas & G. Fernando.  
*Structural Integrity Evaluation of Wind Turbine Blades Using Pattern Recognition Analysis on Acoustic Emission Data.* Proceedings, 25th European Conference on Acoustic Emission Testing, 2002.
- [21] A.G. Dutton, M. Blanch, P. Vionis, V. Kolovos, D.R.V. van Delft, P. Joosse, A. Anastassopoulos, D. Kouroussis, T. Kossivas, J. ter Laak, T.P. Philippidis, Y.G. Kolaxis, G. Fernando, G. Zheng, T. Liu & A. Proust.



- Acoustic Emission Monitoring from Wind Turbine Blades Undergoing Static and Fatigue Testing*. Proceedings, 15th World Conference on Non-Destructive Testing, 2000.
- [22] M.A. Rumsey & J.A. Paquette.  
*Structural Health Monitoring of Wind Turbine Blades*. Proceedings of the SPIE, 6933, 2008.
- [23] A.G. Dutton, M.J. Blanch, P. Vionis, D. Lekou, D.R.V. van Delft, P.A. Joosse, A. Anastasopoulos, D. Kouroussis, T. Kossivas, T.P. Philippidis, T.T. Assimakopoulou, G. Fernando, C. Doyle & A. Proust.  
*Acoustic Emission Condition Monitoring Of Wind Turbine Rotor Blades: Laboratory Certification Testing To Large Scale In-Service Deployment*. Proceedings, European Wind Energy Conference, 2003.
- [24] M.J. Blanch & A.G. Dutton.  
*Acoustic Emission Monitoring of Field Tests of an operating Wind Turbine*. Key Engineering Materials, 245-246, 2003.
- [25] Erik Gross, Todd Simmermacher, Mark Rumsey & R.I. Zadoks.  
*Application of Damage Detection Techniques using Wind Turbine Modal Data*. Journal for American Institute of Aeronautics and Astronautics, 1999.
- [26] Agilent Technologies.  
*The Fundamentals of Model Testing*. Application Note 243-3.
- [27] Hansang Kim & Hani Melhem  
*Damage detection of structures by wavelet analysis*. Journal of Engineering Structures, 26, 2004.
- [28] R.J.H. Paynter & A.G. Dutton  
*The Use of a Second Harmonic Correlation to Detect Damage in Composite Structures Using Thermoelastic Stress Measurements*. Journal in Strain, 39, 2003.
- [29] The Energy Center, Wind Energy Products & Info.  
<http://www.thesolarenergycenter.com/page/390544203>. Accessed 19.01.2013.
- [30] The Windpower, Wind turbines and farms database, GE Energy 1.5xle.  
[http://www.thewindpower.net/turbine\\_en\\_58\\_ge-energy\\_1.5xle.php](http://www.thewindpower.net/turbine_en_58_ge-energy_1.5xle.php). Accessed 17.05.2013.
- [31] ANSYS WB - Wind Turbine Blade - Problem Specification, Added by Benjamin J. Mullen.  
<https://confluence.cornell.edu/display/SIMULATION/ANSYS+WB+-+Wind+Turbine+Blade+-+Problem+Specification>. Accessed 10.05.2013.
- [32] JARP Equipment, GE Wind Turbine.  
<http://jarpequipment.com/id/3171>. Accessed 17.05.2013.

- [33] C. Yanbin, S. Lei & Z. Feng.  
*Modal Analysis of Wind Turbine Blade Made of Composite Laminated Parts*. Pow. and En. Eng. Conf., 2010 Asia-Pacific, 2010.
- [34] J.S. Bendat & A.G. Piersol.  
*Random Data Analysis and Measurement Procedures*. John Wiley & Sons, Edition 4, 2010.
- [35] R.J. Allemang & D.L. Brown.  
*A Correlation Coefficient for Modal Vector Analysis*. Proceedings, International Modal Analysis Conference, 1982.
- [36] O.S. Salawu.  
*Detection of structural damage through changes in frequency: a review*. Journal of Engineering Structures, 19, 718-723, 1997.
- [37] Norris Stubbs, Jeong-Tae Kim & C.R. Farrar.  
*Field Verification of a Nondestructive Damage Localization and Severity Estimation Algorithm*. Proceedings 13th Int. Modal Analysis Conf., 1, 1995.
- [38] E. Douka, S. Loutridis & A. Trochidis.  
*Crack identification in beams using wavelet analysis*. International Journal of Solids and Structures, 40, 2003.
- [39] S. Loutridis, E. Douka, L.J. Hadjileontiadis & A. Trochidis.  
*A two-dimensional wavelet transform for detection of cracks in plates*. Journal of Engineering Structures, 27, 2005.
- [40] Stephane Mallat.  
*Characterization of signals from multiscale edges*. Academic Press, 2nd edition, 1998.
- [41] YAWTb: Yet Another Wavelet Toolbox.  
<http://sites.uclouvain.be/ispgroup/yawtb/>. Accessed 07.03.2013.
- [42] Brüel & Kjær, PULSE Analyzer Platform.  
<http://www.bksv.dk/Products/pulse-analyzer.aspx>. Accessed 08.01.2013.
- [43] C.Y. Shih, Y.G. Tsuei, R.J. Allemang & D. L. Brown.  
*Complex Mode Indication Function and its Applications to Spatial Domain Parameter Estimation*. Journal of Mechanical Systems and Signal Processing, 2, 1988.
- [44] Brian Wallace.  
*Development and validation of a wind generator field testing methodology*. Master Thesis in Aerospace Engineering, The Pennsylvania State University, The Graduate School, Department of Aerospace Engineering.

- [45] M.J. Sundaresan, M.J. Schulz & A. Ghoshal.  
*Structural Health Monitoring Static Test of a Wind Turbine Blade*. Subcontract Report, NREL/SR-500-28719, March 2002.
- [46] Dmitri Kopeliovich, SubsTech, Polyester matrix composite reinforced by glass fibers (Fiberglass).  
[http://www.substech.com/dokuwiki/doku.php?id=polyester\\_matrix\\_composite\\_reinforced\\_by\\_glass\\_fibers\\_fiberglass](http://www.substech.com/dokuwiki/doku.php?id=polyester_matrix_composite_reinforced_by_glass_fibers_fiberglass). Accessed 01.12.2012.
- [47] MatWeb, MatWeb, Overview of materials for PVC, Foam Grade.  
<http://www.matweb.com/search/DataSheet.aspx?MatGUID=e19bc7065d1c4836a89d41ff23d47413&ckck=1>. Accessed 01.12.2012.
- [48] ANSYS Workbench 14.0 Help Menu (part of the ANSYS software).
- [49] C. Lindenburg.  
*BLADMODE, Program for Rotor Blade Mode Analysis*. Energy research Centre of the Netherlands, ECN-C-02-050, 2003.
- [50] Kourepinis Vasileios.  
*Strengthening of Steel Bridges by GFRP Plates*. Master's thesis, Faculty of Civil Engineering & Geosciences, Delft University of Technology.
- [51] T. Dallard & G.R. Spedding.  
*2-D wavelet transforms: generalisation of the Hardy space and application to experimental studies*. European Journal of Mechanics-B/Fluids, 12, 1993.